Using Low-Frequency Earthquakes to Investigate Slow Slip Processes and Plate Interface Structure Beneath the Olympic Peninsula, WA

Shelley Chestler

A dissertation submitted in partial fulfillment of the requirements

for the degree of

Doctor of Philosophy

University of Washington

2017

Reading Committee:

Ken Creager, Chair

Heidi Houston

David Schmidt

Program Authorized to Offer Degree:

Earth and Space Sciences

University of Washington

Abstract

Using Low-Frequency Earthquakes to Investigate Slow Slip Processes and Plate Interface Structure Beneath the Olympic Peninsula, WA

Shelley Chestler

Chair of the Supervisory Committee:

Professor Ken Creager

Department of Earth and Space Sciences

This dissertation seeks to further understand the LFE source process, the role LFEs play in generating slow slip, and the utility of using LFEs to examine plate interface structure. The work involves the creation and investigation of a 2-year-long catalog of low-frequency earthquakes beneath the Olympic Peninsula, Washington.

In the first chapter, we calculate the seismic moments for 34,264 low-frequency earthquakes (LFEs) beneath the Olympic Peninsula, WA. LFE moments range from 1.4×10^{10}–1.9×10^{12} N-m (M_W=0.7-2.1). While regular earthquakes follow a power-law moment-frequency distribution with a b-value near 1 (the number of events increases by a factor of 10 for each unit increase in M_W), we find that while for large LFEs the b-value is ~6, for small LFEs it is <1. The

magnitude-frequency distribution for all LFEs is best fit by an exponential distribution with a mean seismic moment (characteristic moment) of 2.0×10^{11} N-m. The moment-frequency distributions for each of the 43 LFE families, or spots on the plate interface where LFEs repeat, can also be fit by exponential distributions. An exponential moment-frequency distribution implies a scale-limited source process. We consider two end-member models where LFE moment is limited by (1) the amount of slip or (2) slip area. We favor the area-limited model. Based on the observed exponential distribution of LFE moment and geodetically observed total slip we estimate that the total area that slips within an LFE family has a diameter of 300 m. Assuming an area-limited model, we estimate the slips, sub-patch diameters, stress drops, and slip rates for LFEs during ETS events. We allow for LFEs to rupture smaller sub-patches within the LFE family patch. Models with 1-10 sub-patches produce slips of 0.1-1 mm, sub-patch diameters of 80-275 m, and stress drops of 30-1000 kPa. While one sub-patch is often assumed, we believe 3-10 sub-patches are more likely.

In the second chapter, using high-resolution relative low-frequency earthquake (LFE) locations, we calculate the patch areas (A_p) of LFE families. During Episodic Tremor and Slip (ETS) events, we define A_T as the area that slips during LFEs and S_T as the total amount of summed LFE slip. Using observed and calculated values for A_P, A_T and S_T we evaluate two end-member models for LFE slip within an LFE family patch (models 2 and 3 from chapter 1). In the ductile matrix model (model 3), LFEs produce 100% of the observed ETS slip (S_{ETS}) in distinct sub-patches (i.e., $A_T<<A_P$). In the connected patch model (model 2), $A_T=A_P$, but $S_T<<S_{ETS}$. LFEs cluster into 45 LFE families. Spatial gaps (~10-20 km) between LFE family clusters and smaller gaps within LFE family clusters serve as evidence that LFE slip is heterogeneous on multiple spatial scales. We find that LFE slip only accounts for ~0.2% of the slip within the slow slip

zone. There are downdip trends in the characteristic (mean) moment and in the number of LFEs during both ETS events (only) and the entire ETS cycle ($M_{c,ETS}$ and $N_{T,ETS}$ and $M_{c,all}$ and $N_{T,all}$ respectively). During ETS, M_c decreases with downdip distance but N_T does not change. Over the entire ETS cycle, M_c decreases with downdip distance, but N_T increases. These observations indicate that downdip LFE slip occurs through a larger number (800-1200) of small LFEs, while updip LFE slip occurs primarily during ETS events through a smaller number (200-600) of larger LFEs. This could indicate that the plate interface is stronger and has a higher stress threshold updip.

In the third chapter, we use high-precision, relative low-frequency earthquake (LFE) locations for LFEs beneath the Olympic Peninsula, WA to constrain the depth, geometry, and thickness of the plate interface. LFE depths correspond most closely with the McCrory et al. (2012) plate model, but vary from that smooth model along strike. The latter observation indicates that the actual plate interface is notably rougher and more complex than smooth plate models. Our LFEs lie directly above low-velocity zone (LVZ) and approximately 5 km above intraslab earthquakes. This supports the proposal of Bostock (2013), that the LVZ comprises the upper oceanic crust and that fluids are responsible for the velocity contrast across the LVZ and likely play a large role in generating slow slip and LFEs. Within each of our LFE families, LFEs group into tight clusters around the family centroid. The width of these clusters in the depth direction, which is an indicator of the thickness of slow slip deformation on the plate interface, is 130 to 340 meters.

Table of Contents

Introduction

The Cascadia Subduction Zone (CSZ) is the plate boundary, stretching approximately 1,000 km from Cape Mendocino, CA to Vancouver Island, Canada, where the oceanic Juan de Fuca plate subducts beneath the continental North American plate at a rate of approximately 4 cm/yr. In the shallow (<25 km), locked portion of the subduction zone, plate convergence is accommodated by large (~M8.0-9.0) megathrust earthquakes with recurrence intervals of 300-500 years (Atwater, 1987, 1992). These earthquakes pose a threat for both coastal infrastructure and large population centers in the Pacific Northwest. In the deep portion of the subduction zone (>45 km depth), the plates slide past each other at a steady rate without producing observable seismic energy.

In the early 2000s another type of phenomenon, called slow slip, was discovered in the transition zone between the locked and steadily-sliding zones (~25-45 km depth) (Dragert et al., 2001) (Figure 1.1). During slow slip events (SSEs) the plates slide past each other orders of magnitude slower than during "regular" earthquakes. The slip produces a seismic signal, called tremor, that is non-impulsive and depleted in high-frequency content when compared to "regular" earthquakes (Rogers & Dragert, 2003). SSEs and accompanying tremor have been observed in many other subduction zones worldwide, including Nankai (Obara, 2002; Obara et al., 2004), the Hikurangi Trench (Douglas et al., 2005; Kim et al., 2011), Guerrero, Mexico (Kostoglodov et al., 2003; Payero et al., 2008; Yoshioka et al., 2004), Alaska (Ohta et al., 2006; Peterson & Christensen, 2009), and Costa Rica (K. M. Brown et al., 2005; Jiang et al., 2012).

In Cascadia, SSEs propagate along strike at rupture speeds of 7-12 km/day, approximately four orders of magnitude slower than "regular" earthquakes. Large SSEs, with accompanying tremor, called episodic tremor and slip (ETS) events, occur in northern Cascadia

at regular intervals of 12-15 months. Each ETS event releases the same amount of energy as a M6.0-6.8 earthquake (Schmidt & Gao, 2010), but over several weeks instead of timescales of seconds to minutes. Smaller SSEs, lasting several hours to several days, occur throughout the year. These smaller SSEs are often too small to be observed geodetically but can be observed in tremor data (Ghosh et al., 2012; Wech & Creager, 2008, 2011).

While slow slip events do not pose a threat for humans or infrastructure, understanding how slow slip occurs is important for understanding how plate convergence is accommodated within subduction zones. In addition, knowledge of how slow slip interacts with strain build-up and relief in the locked zone will enhance our understanding of both the recurrence and downdip limit of megathrust earthquakes.

Low-frequency earthquakes (LFEs), tiny, repeating earthquakes that make up tectonic tremor (Shelly et al., 2007), are a common tool used to study when and where slow slip is happening. LFEs occur via shear slip on the plate interface (Ide et al., 2007; Shelly et al., 2007) and, like tremor, are depleted in high-frequency content compared to "regular" earthquakes. One difference between tremor and LFEs is that LFEs have identifiable P- and S-wave arrivals while tremor does not. As a result of this difference, LFEs can be located more accurately and with higher temporal resolution than tremor. Hence, they serve as more precise slip indicators.

While we know that LFEs are generated during slow slip, the specifics of how LFEs and slow slip are related are not well understood. How much SSE slip releases seismic energy via LFEs? Do LFEs occur everywhere in the slow slip zone, or just in areas with favorable frictional/compositional properties for generating LFEs? The answers to these questions are important for building a core understanding of the role LFEs play in generating slow slip.

Another gap in our understanding of LFEs is the details of the LFE source process (e.g. the amount of slip, slip area, and stress drop). LFEs are clustered into LFE families, or groups of LFEs that repeat over and over again within a small patch (~1 km^2) (Sweet, 2014). However, the details of how slip occurs within an LFE family patch are not well understood. A study by Bostock et al. (2015) on southern Vancouver Island found that though LFE moments vary by more than an order of magnitude, LFE durations are relatively constant (~0.3-0.5 seconds). The interpretation is that LFEs are not self-similar; LFEs have larger moments due to greater amounts of slip and not a larger slip area. Additionally, Thomas et al. (2016) used empirical Green's function analysis to show that LFEs on the San Andreas Fault have lower rupture speeds, slip speeds, and stress drops than "regular" earthquakes of similar magnitude, but faster slip speeds than SSEs. The faster slip speeds of LFEs relative to the surrounding slowly slipping regions, results in the radiation of detectable seismic energy (Thomas et al., 2016). These two studies laid the groundwork for understanding the LFE source process and expanding on their findings will lead to further insight on how LFE slip occurs.

This dissertation seeks to further understand the LFE source process and the role LFEs play in generating slow slip. To do this I create a 2-year catalog of low-frequency earthquakes beneath the Olympic Peninsula, Washington. The catalog includes 39,966 LFEs sorted into 45 LFE families, the locations and detection histories for each family, and the magnitudes for individual LFEs. Using the catalog, I (1) further expand our knowledge of the LFE source process, (2) propose a model for how slip occurs within an LFE family patch, (3) examine the role of LFEs in generating slow slip across the entire slow slip zone, and (4) show how LFEs can be used to investigate plate interface structure.

There are three chapters. The first chapter is a paper published in the *Journal of Geophysical Research* entitled "Evidence for a scale-limited LFE source process" (Chestler and Creager, 2017). In the paper, I calculate the moments for 34,264 LFEs. I show that the moment-frequency relationship for LFEs is exponential, which indicates a scale-limited LFE source process. I propose three different models for slip within an LFE family patch: (1) where each LFE slips over the entire LFE family patch, (2) where LFEs slip on multiple connected sub-patches within the LFE family patch, and (3) where the LFE sub-patches are separate and surrounded by a ductilely deforming matrix. I conclude that LFEs likely slip on multiple (3-10) sub-patches (i.e., models 2 and 3).

The second chapter is a paper, entitled "A model for low-frequency earthquake slip," that has been submitted to *Geochemistry, Geophysics, Geosystems*. In the paper, I further evaluate models 2 and 3 from the first chapter of my dissertation, which I call the connected patch and ductile matrix models respectively. To do this, I estimate values for LFE family patch area (A_P), calculated from high-precision relative LFE locations, the area that slips during LFEs (A_T), and summed LFE slip (S_T). In the ductile matrix model, I assume that LFEs produce 100% of the observed ETS slip (S_{ETS}) in distinct sub-patches and find that $A_T << A_P$. In the connected patch model, $A_T = A_P$, but $S_T << S_{ETS}$. Additionally, I investigate LFE slip across the entire slow slip zone. While LFEs cluster into 45 LFE families, there are spatial gaps (~10-20 km) between clusters of LFE families and smaller gaps within LFE family clusters. The gaps in the catalog serve as evidence that LFE slip is heterogeneous on multiple spatial scales. LFEs and LFE families are surrounded by areas that do not produce slip in the form of observable, repeating LFEs. Finally, I calculate LFE slip from the moments of LFEs and estimate that LFE slip only accounts for ~0.2% of the total slip that occurs within the slow slip zone.

In the third and final chapter, which also will be submitted to *Geochemistry, Geophysics, Geosystems*, I use the same high-precision, relative LFE locations from chapter 2 to investigate the structure of the plate interface. My main finding is that the spread of LFEs within LFE families in the depth direction, an analog for the thickness of deformation in the slow slip zone, is 130-340 meters. I also find that LFEs lie on top of the widely-observed low-velocity layer and that, beneath the Olympic Peninsula, LFE depths align most closely with the McCrory et al. (2012) plate interface model. LFEs at similar downdip distances dip down ~10-15° to the north, which indicates that the plate interface may not be smooth.

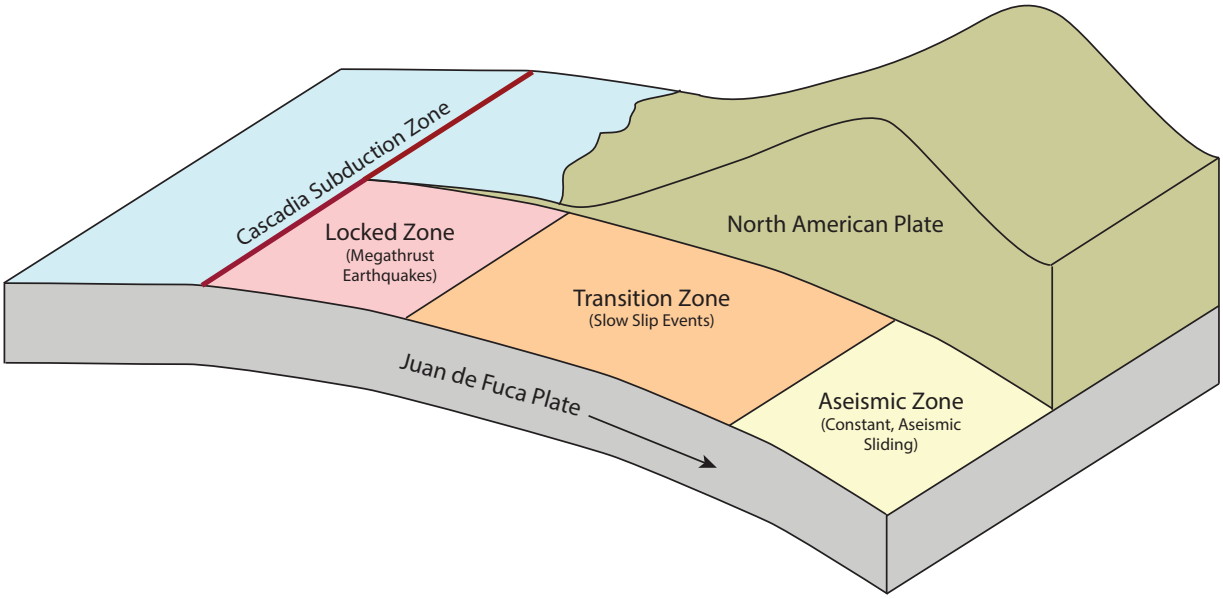

Figure 1.1: Cartoon cross section of the Cascadia Subduction Zone illustrating the relative geometry of the locked, transition and aseismic zones.

Evidence for a scale-limited low-frequency earthquake source process

The content of this chapter was published in:

Chestler, S. R., & Creager, K. C. (2017). Evidence for a scale-limited Low-Frequency Earthquake source process. *Journal of Geophysical Research: Solid Earth*, 2016JB013717. https://doi.org/10.1002/2016JB013717.

1 Introduction

Low-frequency earthquakes (LFEs) are tiny, repeating earthquakes that are thought to make up tectonic tremor (Shelly et al., 2007). Both LFEs and tremor are depleted in high-frequency content when compared to "regular" earthquakes. One difference between LFEs and tremor is that LFEs have identifiable P- and S-wave arrivals, while tremor does not. Like "regular" earthquakes, LFEs occur due to shear slip (Ide et al., 2007; Shelly et al., 2007). Both LFEs and tremor occur during slow slip events (SSEs) in subduction zones worldwide (e.g., Japan (Shelly et al., 2006), Cascadia (Bostock et al., 2012; Y. Peng & Rubin, 2016; Plourde et al., 2015; Royer & Bostock, 2014; Rubin & Armbruster, 2013; J. Sweet, 2014; Thomas & Bostock, 2015), the Aleutians Brown et al., 2013;Wech, 2016), and Mexico (Frank et al., 2013)) and some strike-slip settings (e.g. Parkfield (Shelly, 2010)) and are thought to be localized asperities that rupture more seismically than the surrounding regions (Beeler et al., 2013; Shelly et al., 2007). Both LFEs and tremor are used as indicators of when and where slow slip is happening. Because LFEs have identifiable P- and S-wave arrivals, they can be located more accurately and with higher temporal resolution than tremor. Hence, they serve as more precise slip indicators.

Though LFEs are used frequently to study slow slip, insight on the details of the LFE source process (e.g. the amount of slip, slip area, and stress drop) is limited. A recent study by Bostock et al. (2015) on southern Vancouver Island found that though LFE moments vary by more than an order of magnitude, LFE durations are relatively constant (~0.3-0.5 seconds). The interpretation is that LFEs are not self-similar; LFEs have larger moments due to greater amounts of slip and not a larger slip area. Slip dimension should scale with duration assuming constant rupture velocity. Thomas et al. (2016) used empirical Green's function analysis to show that LFEs on the San Andreas Fault have lower rupture speeds, slip speeds, and stress drops than "regular" earthquakes of similar magnitude, but higher slip speeds than SSEs. Because LFEs slip faster than the surrounding slowly slipping regions, they radiate detectable seismic energy (Thomas et al., 2016). The implication is that slip speed may govern the distribution of LFE asperities. Local regions of accelerated slip speed can be produced using rate and state friction by imposing spatial variations in the cutoff velocity, effective stress, or frictional parameters (Hawthorne & Rubin, 2013). Physical explanations for these variations include variations in bulk rheology (Fagereng et al., 2014) or local variations in fluid pressure (Thomas et al., 2016).

The moment-frequency relation for LFEs is another topic of debate. While Bostock et al. (2015) favors a power-law distribution with a b-value ($b \approx 6.3$) much higher than "regular" earthquakes ($b \sim 1$), (Sweet, 2014) suggests that the moment-frequency relationship of LFEs is best fit by an exponential distribution. Watanabe et al. (2007) also observes an exponential distribution of tremor amplitudes in Japan. In an exponential distribution, the natural log of the number of events exceeding a given moment verses moment is a straight line whose slope is the inverse of the characteristic moment. The characteristic moment is also the mean of the exponential distribution. An exponential moment-frequency distribution implies that the LFE

rupture process is scale limited. Bostock et al. (2015) support this conclusion, though they prefer a power-law moment frequency distribution over a limited range of moments.

Here, we produce a new catalog of 43 LFE families beneath the Olympic Peninsula, WA using the data from the Array of Arrays (AofA) and Cascadia Arrays for Earthscope (CAFE) experiments. We find that LFEs follow an exponential moment-frequency distribution and show that the characteristic moment of individual LFE families is larger during ETS events than during inter-ETS time periods. Finally, assuming that the LFE source process is limited by slip area we estimate the slips, sub-patch diameters, stress drops, and slip rates for LFEs during ETS events.

2 Methods

2.1 Finding and Locating LFEs

We use high signal-to-noise (SNR) level waveforms, calculated by Ghosh et al. (2012) using multibeam-backprojection (MBBP), to create a catalog of low-frequency earthquakes. The data were collected during the Array of Arrays (AofA) experiment, which consisted of eight 1-km aperture arrays, each with 10-20 3-component stations that were deployed from June 2009 to September 2010 and August 2011. For each array and every 1-minute time window Ghosh et al. (2012) filtered vertical-component seismograms between 5-9 Hz. Then they apply a delay-and-sum beamforming approach to stack data and find the vector slowness corresponding to the direction of a plane wave that produces the stack with the most power. Stacking seismograms from each window at the optimal slowness produces a continuous time series with excellent SNR. This is repeated for each array and every 50-percent overlapping one-minute time window.

We use these high SNR waveforms to search for new LFE families. For each array, j, we select all the peaks, ℓ, that are larger than 18 times the median absolute deviation (MAD) and store their times, t_ℓ^j, and amplitudes, A_ℓ^j. To find peaks recorded at multiple arrays and account

for the difference in arrival times between arrays, we create a boxcar-like time series for each array:

$$s_j(t) = \sum_{\ell=1}^{N_j} A_\ell^j \, \mathrm{B}(t - t_\ell^j) \qquad [1]$$

where A_ℓ^j is either the amplitude of the ℓth peak or 1, and N_j is the number of peaks at array, j. We have processed the data both ways. $\mathrm{B}(t - t_\ell^j)$ is the boxcar function:

$$\mathrm{B}\left(t - t_\ell^j\right) = \begin{cases} 1 & \text{if } \left|t - t_\ell^j\right| < 1 \\ 0, & \text{elsewhere} \end{cases}. \qquad [2]$$

Finally, we stack the time series', s_j, for all arrays and use the peaks in the resulting function as potential LFEs.

To verify that potential LFEs repeat in time, using a set of 3-stations from each array, we autocorrelate 15-second windows of 3-component data, band-passed between 2 and 8 Hz, centered on each peak through time. We stack the autocorrelation functions for all channels and stations using an n^{th}-root stack where n=2 and look for times when the stacked autocorrelation function exceeds 45 times the median absolute deviation (MAD). For each potential LFE, up to 150 of the time windows that correlate best with the initial detection are stacked to create a template waveform. We found that stacking more than 150 windows does not result in templates with better SNRs. If the template has clear P- and S-wave arrivals, we strengthen it by autocorrelating the template waveform through time to look for additional correlating time windows and re-stack to create template waveforms with higher SNRs. After three iterations, we group the original LFE and all the correlating time windows into an LFE family, imposing a stricter correlation threshold that varies from 0.05 to 0.20 depending on the number of stations that are active at the time of the LFE (0.05, 0.1, 0.14, 0.15, 0.2 for less than 6 stations, 7-9

stations, 10-12 stations, 13-15 stations, and more than 15 stations respectively). Templates also include stations from the CAFE experiment located near the AofA.

To locate LFE families we first produce P- and S-wave differential times by cross correlating stacked templates across different stations and S minus P times by cross correlating S- (on horizontal channels) verses P- (on vertical channels) waves at the same stations. We then perform a grid search using the 3D velocity model from Preston et al. (2003) to locate each LFE family. We convert this P-wave model to an S-wave model assuming the earth is a Poisson solid. Finally we improve relative locations between nearby families using the double difference method of Waldhauser and Ellsworth (2000) applied to differential P- and S-times determined by the autocorrelation of template waveforms.

2.2 Processing the LFE Catalog

We processed our LFE catalog so that: (1) there are no duplicate LFE families, and (2) the detections within each family are unique. We assess the similarity of two LFE families by the ratio, R_{com}, of the number of common detections between the two families to the number of LFE detections in the family with the least number of detections. When two LFE families have $R_{com} > 0.5$, the family with the lower median correlation coefficient is removed. This is nearly always the family with fewer detections. This reduced the number of LFE families from 57 to 43. After this step, if there are still LFEs that are included in multiple families, we keep the LFE in the family that it correlates best with and remove it from the others.

2.3 Calculating LFE Moments

Using AofA data, we invert for the seismic moments of each LFE following the method from Sweet (2014). We deconvolve our data to obtain displacement and filter it between 2 and 8 Hz. For each array (~10 stations per array) we find the times corresponding to the maximum S-

wave amplitude within ±1 second of the predicated arrival time on each of the horizontal channels. We keep only the channels where the maximum amplitude occurs within ±0.2 seconds of each other. We predict the S-wave polarity in two ways: (1) we test each of 4 possible channel orientations (E-up/N-up, E-up/N-down, E-down/N-up, E-down/N-down) to find which produces the highest number of consistent arrivals, and (2) we calculate the polarity for a thrust source on the plate interface at the location of the LFE family. In most cases these two methods agree, but if they do not we favor the polarizations calculated by the shallow thrust source. Next, for each station, k, we estimate the time integral of the displacement pulse, ${d^N}_k$ and ${d^E}_k$ for the north and east channels, by finding the local minima on either side of the S-wave maximum and calculating the area of the triangle formed by these three points. Finally, we calculate and later use the median value of this integral across all the time-consistent channels (i.e. channels with peaks within 0.2 sec of each other) for each array and LFE pair. While this calculation may seem crude, it is designed to obtain a robust estimate of moment by using signals that are coherent within each array even though the SNR is low. We believe it is a good enough approximation given other sources of error during the inversion process (e.g. uncertainty of attenuation, the exact density/velocity structure of the subsurface beneath the Olympic Peninsula, the focal mechanism, and the signal-to-noise ratio for these tiny events).

To solve for moment, we use the following equation (adapted from Shearer, 2009) for far-field S-wave displacement, $\mathbf{u}^s$, in an elastic whole space observed at position $\mathbf{x}$ from a source at $\mathbf{x}$=0:

$$\mathbf{u}^s(\mathbf{x},t) = \frac{1}{4\pi\rho\beta^3}\left(\cos 2\theta \cos\phi\, \widehat{\boldsymbol{\theta}} - \cos\theta \sin\phi \widehat{\boldsymbol{\phi}}\right)\frac{1}{r}\dot{M}_0\left(t-\frac{r}{\beta}\right) \qquad [3]$$

where β is the shear-wave velocity, ρ is density, r is source-receiver distance, and $\dot{M}_0$ is moment rate. We rearrange terms and integrate moment rate over time to solve for seismic moment (M_0).

We also modify the equation for the transmission coefficient between the velocity and density at source, β_2=4010 m/s and ρ_2=3300 kg/m^3, and the velocity and density at the receiver, β_1=3110 m/s and ρ_1=2700 kg/m^3. Both this modification, and the surface correction, R, assume a model with only a source and receiver velocity and near-vertical ray paths. The resulting equation is:

$$M_0 \approx \frac{4\pi {\beta_2}^2(\rho_1\beta_1 + \rho_2\beta_2)r}{2Rc} e^{\frac{rf\pi}{\beta Q_s}} * \text{median}({d^N}_k, {d^E}_k) \quad [4]$$

where $\text{median}({d^N}_k, {d^E}_k)$ is the time integral of the S-wave displacement observed at each array as described above, R=2 is a free-surface correction for near-vertical incident rays, c=0.35 is the average amplitude of the directional terms in equation 3 over the unit sphere, f=2 Hz is the dominant frequency, β is the average of β_1 and β_2, and Q_s is the S-wave quality factor. We use a quality factor of 200, an estimate of the regional average Q_s from a previous study in northern Washington by (Gomberg et al., 2012). The corresponding anelastic attenuation parameter is $c_2 = \pi f/\beta Q_s$ = 0.0087 km^{-1}, which is twice the size of the value c_2=0.0044-0.0048 km^{-1} estimated using tremor amplitudes in the same area by Baltay and Beroza (2013).

For a given LFE family we simultaneously invert for moment of each LFE ($\ln M_i$, i=1:N$_{LFE}$) and for dimensionless array correction terms ($\ln S_j$, j=1:N$_{array}$), where $\ln S_j$ sum to zero. The forward problem is:

$$\ln M_i - \ln S_j = \ln C_{ij} + \ln D_{ij} \quad [5]$$

where $C_{ij} = \frac{4\pi {\beta_2}^2(\rho_1\beta_1 + \rho_2\beta_2)r}{2Rc} e^{\frac{rf\pi}{\beta Q}}$ is known and D_{ij} is the median of the time integral of the observed S-wave displacement for the ith source at the jth array. Because the amplitudes of LFE waveforms are often similar to the background noise (see section 4.1), for each LFE we eliminate low SNR stations by only using arrays with 10 or more time-consistent observations. We perform this inversion for each LFE family separately.

3 Results

3.1 LFE Catalog and Sorting

Initially, we found 57 LFE families beneath the Olympic Peninsula, WA, (Figure 2.1) each with 250-1700 detections during the time when the AofA experiment was active. There are 34,479 LFEs in total. The values of R_{com} for this catalog range from zero (no duplicate detections) to ~0.8, and decreases with distance between LFE families (Figure 2.1). There are two reasons why the same detection could be in two or more LFE families: (1) the LFEs families could be the same, or (2) the detection could belong in one family, but still correlate well with another family because the two families are located close to each other. The latter is probable for our catalog because we allow for correlation coefficients as low as 0.05. To account for our low correlation coefficient but also remove as many duplicate families as possible, for our final catalog we use 0.5 as our R_{com} threshold. After sorting the remaining duplicate detections into their proper families, our final catalog includes to 32,387 unique LFEs sorted into 43 families (Figure 2.2). The locations of LFE families in our catalog are similar to LFEs in others catalogs beneath the Olympic Peninsula from Royer and Bostock (2014) and Peng and Rubin (2016). Royer and Bostock (2014) created a catalog using a method similar to this work, but did not use data from the AofA. Peng and Rubin (2016) created their catalog using the AofA data, but used the cross-station method piloted by Rubin and Armbruster (2013). The similarities across these LFE catalogs, despite the differences in techniques used to create catalogs, gives us confidence in our LFE detections and locations.

3.2 LFE Moments

We calculate LFE moments for 34,264 LFEs. Because for each LFE we only use arrays with 10 or more time-consistent observations, there are some LFEs that do not have any robust

amplitude measurements. Hence these LFEs are not included in our moment catalog. LFE moments range from $M_o \approx 1.4\times10^{10} - 1.9\times10^{12}$ N-m (M_W = 0.7-2.1). We also calculate displacements by numerically integrating between the two S-wave minima. The mean percent difference between moments calculated with numerically integrated displacements and the moments calculated with displacements estimated by triangles is -0.5% and the standard deviation is 11.9%.

Our calculated LFE moments are about a factor of five smaller than those measured by Bostock et al. (2015) (M_W=1.0-2.61 or $M_o \approx 4\times10^{10} - 1\times10^{13}$ N-m) beneath Vancouver Island. One difference in our calculations is that Bostock et al. (2015) uses c_2=0.005 km^{-1}, more similar to the value of c_2 observed by Baltay and Beroza (2013). But, using this smaller value for c_2 would result in a decrease in our calculated seismic moments by 20%, further broadening the gap between our moments and those from Bostock et al. (2015). The difference between our moments and Bostock's can be rectified by using a much higher value of c2≈0.055, which corresponds to an unrealistically low value of $Q_s = 60$. The relative moments of LFEs are nearly the same independent of the choice of c_2.

Two components of our methods that differ from Bostock et al. (2015) and could lead to underestimated moments; (1) filtering our data between 2 and 8 Hz, which results in band-limited moments, and (2) using triangles to calculate displacement. Bostock et al. (2015) filter their data between 1 and 8 Hz. Additionally, Bostock et al. (2015) estimates displacement using signal in 2-second-long detection windows, a timescale longer than their typical S-wave duration (0.5 seconds). Hence, noise within the detection window could be incorporated into their calculations. By only using triangles made of the S-wave maxima and adjacent minima, we are

being more conservative than Bostock et al. (2015), but our displacement estimates are less susceptible to bias.

To test whether the differences in moment between our two catalogs are a result of method differences, using our method and filter, we calculated the displacement for an LFE beneath Vancouver Island on one channel. Our calculated integrated displacement is 1.4×10^{-8} m-s compared to 2.1×10^{-8} m-s from Bostock et al. (2015). We calculated the moment of the LFE using c_2=0.005 km^{-1}. The resulting value for moment (~2.0×10^{12} N-m) is only 25% larger than the value calculated by Bostock et al. (2015) for the same LFE (~1.6×10^{12} N-m). Given the similarity in moments for the same LFE calculated using both methods, we believe that while our methods are different, this discrepancy alone cannot account for the differences in LFE moment.

We suggest two possible options for why moments for Olympic Peninsula LFEs are smaller than Vancouver Island LFEs: (1) our LFEs could be smaller or, (2) attenuation could be much larger beneath the Olympic Peninsula than Vancouver Island.

We also examine the duration of our LFEs, measured from the data band-pass filtered between 2-8 Hz. Measured durations are ~0.25-0.4 seconds, but we do not think these durations are significant given our filter.

3.3 Moment-Frequency Distribution

We model the distribution of LFE moments using both power-law and exponential functions. The power-law relationship is given by the equation:

$$\log_{10}N = \alpha_1 - \beta\log_{10}\mathrm{M_o} = \alpha_2 - b\mathrm{M}_w, \qquad [6]$$

where N is the number events with moment greater than $\mathrm{M_o}$(N-m), $\beta = \frac{2}{3}b$ is the best fitting exponent where $N = 10^{\alpha_1}{M_o}^{-\beta}$ and b is the b-value of a Gutenberg-Richter distribution (eq. 6). Conversely, the exponential relationship is given by the equation:

$$\log_{10} N = \alpha_3 - \gamma \mathrm{M}_o, \quad [7]$$

where α_3 is the y-intercept and γ is the slope. $\mathrm{M}_c = \frac{1}{\gamma \ln 10}$ is the characteristic moment. It is both the negative inverse of the slope of $\ln N$ verses M_o and the mean moment of the exponential distribution. 37%, 1% and 0.01% of LFEs have moment exceeding M_c, $4.6\mathrm{M}_c$, and $9.2\mathrm{M}_c$ respectively.

The upper range of moments for all our LFEs ($\mathrm{M_o} > 4.3\times10^{11}$ N-m) can be fit by a power-law function with $b = 6.5$ ($\beta = 4.3$) (Figure 2.3b). This result is similar to Bostock et al. (2015) who found that LFEs with $\mathrm{M_o} > 2.5\times10^{12}$ N-m are fit by a power-law function with a b-value of 6.3. The high b-value suggests that, compared to the moment-frequency distribution of "regular" earthquakes (b~1), there are many more small LFEs relative to the number of large LFEs. For example, if b=6 for every $\mathrm{M_w}$=2 LFE there are a million $\mathrm{M_w}$=1 LFEs and a trillion $\mathrm{M_w}$=0 LFEs.

We find that the distribution of our entire catalog is best fit by an exponential distribution with $\mathrm{M}_c = 2.05\times10^{11}$ N-m (Figure 2.3a). This distribution matches previous observations of LFEs beneath the Olympic Peninsula (Sweet, 2014), LFEs on the San Andreas Fault (Shelly & Hardebeck, 2010) and observations of tremor in Japan (Watanabe et al., 2007). In contrast to a power-law distribution, which implies a scale-invariant source process, an exponential distribution implies that the source process is scale-limited. Possibilities for what could limit the LFE source-process (i.e. slip or slip area) are discussed below.

We find that the moment-frequency distribution of LFEs within individual LFE families can also be fit by exponential distributions, each with their own value for $\mathrm{M_c}$ (e.g. Figure 2.2 and Figure 2.4). Characteristic moments for individual families range from $0.5–2.7\times10^{11}$ N-m ($\mathrm{M_w}$=1.1-1.5) (Table A1.1). Furthermore, we examine the moment-frequency distribution of LFEs during ETS events and inter-ETS time periods separately. The distribution of LFEs in both

groups can be fit by an exponential distribution and the characteristic moments for LFE families are on average 40% smaller during inter-ETS time periods than during ETS events (Figure 2.4). The updip LFEs have a much bigger ETS verses inter-ETS difference than downdip families (Figure A1.1).

4 Discussion

4.1 Signal to Noise

One potential issue with our catalog is that the SNR for LFE waveforms is low. If we define the SNR for each event as the LFE peak amplitude divided by the MAD of the 1-minute window prior to the event, the 25, 50, and 75 percentile SNRs are 5.3, 7.4, and 10.6 respectively. The correlation between the log of peak-to-trough LFE amplitudes and the log of root-mean-square (RMS) noise during a 1-minute-long window prior to each event, measured on individual stations, is very high and has a slope close to 1 for each array (Figure 2.5). This implies that the ability to detect LFEs depends on the amplitude of background tremor. LFEs with amplitudes much smaller than the amplitude of background tremor are likely not detected.

To examine this issue more closely we divide observations of LFE amplitudes into three groups: those observed on 10 or less consistent channels in a given array, those with 11-15, and those will more than 15. We find that detections with observations on more stations per array have higher amplitudes relative to the RMS noise. To verify this, we visually inspect waveforms for the LFE family whose amplitudes are shown in Figure 2.5. On arrays with 10 or more observations, there are almost always clear LFE pulses (e.g. Figure 2.6). Conversely, on arrays with fewer observations it is hard to distinguish the LFE pulse from the background noise.

As mentioned in section 2.3 we remove observations where the LFE pulse is indistinguishable from the background tremor by calculating LFE moments using only arrays

with time-consistent observations on 10 or more horizontal channels. To verify that this method actually removes unclear signals, for one LFE family (the same family used in Figure 2.5), we manually inspect the waveforms on all arrays for each LFE and pick the arrays with clear waveforms. For individual LFEs, the arrays chosen often have clear pulses on 10 or more channels, but sometimes pulses are visible when there are fewer than 10 channels.

Both the catalog limited to arrays with 10 or more stations and the catalog calculated from our manual picks are missing observed moments for some LFEs. We compare both these catalogs to a catalog where no arrays were removed and find that all three catalogs are fit well by exponential moment-frequency distributions (Figure 2.7). As expected the characteristic moment for the unfiltered catalog is slightly (20%) smaller than the two filtered catalogs, which are virtually indistinguishable. We believe that this consistency means that the exponential fit is robust and not an artifact of low SNR waveforms, though the actual estimate of characteristic moment could be biased by 20% or so (Figure A1.2). This will be discussed in greater detail at the end of this section.

We also test whether an exponential distribution of background tremor (noise) could mask a power law distribution of LFEs. To do this we create a synthetic LFE moment catalog with power-law moment frequency distributions ($b = 4$, $\beta = 2.67$) and maximum LFE moment of 1.8×10^{12} N-m. In addition, we consider background noise with an exponential moment-frequency distribution to represent the background tremor (Watanabe et al., 2007). For each LFE in the synthetic power-law catalog we randomly select a noise value from the exponential noise distribution and only keep the LFE if it exceeds the noise. Figure 2.8 illustrates the effects of varying noise levels. The thick, solid line in the right plot is the synthetic power-law distribution. The symbols represent the LFE distribution after considering noise with characteristic moments

of 10^{10}, 10^{11}, 10^{12} N-m. In each case the filtered catalog retains its near power-law distribution, but the apparent b value decreases with increasing noise from 4 to 3.9, 3.1, and 2.6 respectively and the number of missing events increases from 50% to 99%. Hence, we conclude than an exponential distribution of background tremor would not mask a power-law distribution of LFE moments and that the moment-frequency distribution of our true LFE catalog is exponential.

We do find, however, that if you assume that the underlying LFE distribution is exponential, increasing the M_c of the background noise by 10-100 can increase the apparent M_c of the filtered distribution by a factor of 10-30% (Figure A1.2). Therefore, it is possible that the higher characteristic moments during ETS events (~40% larger than during inter-ETS time periods) could be explained, in part, by a higher level of background tremor.

4.2 Implications of an Exponential Moment-Frequency Distribution

While Bostock et al. (2015) prefer a power-law distribution for the largest events, they acknowledge that this law must break down for smaller events. In particular, our full LFE catalog is best fit by $N = (M_o/2.8e12)^{-4.3}$ for the largest LFEs (Figure 2.3c) corresponding to a b-value of 6.5=3/2*4.3. Extrapolating to smaller LFEs results in 10 million missing events with M_W>1.0, and would predict an average of 10 LFEs of Mw>1 every second continuously for the 5 days the LFEs are active during each ETS. If these small events exist, they would release too much energy. The cumulative moment released by LFEs with $M_o > 2\times10^{10}$ N-m, one order of magnitude smaller than the characteristic moment ($M_c = 2.05\times10^{11}$), would release ~3×10^{19} N-m of energy (Figure 2.9). This is more than the moment released by an entire Cascadia ETS event ($M_w \approx 6.5$, $M_o \approx 7\times10^{18}$) (Hall & Houston, 2014; Schmidt & Gao, 2010). Because the power law distribution must break down for events with smaller moments, we prefer the exponential

moment-frequency relationship. It both fits the data well and naturally provides a scale size and limit on the number of smaller LFEs.

What possibly could impose a scale on LFE seismic moment? Seismic moment is defined as $M_o = \mu SA$, where μ is the shear modulus, S is slip, and A is slip area. Assuming constant rigidity, two end-member models are (1) that the amount of slip is constant and that the size of the patch follows an exponential distribution, or (2) that the slip area is constant and slip follows an exponential distribution. Both models must account for the observations that the characteristic moments for LFE families are larger during ETS events than inter-ETS time periods, especially for up-dip LFEs.

If the size of LFEs were limited by the amount of slip, this would imply that LFE slip area is greater during ETS events than inter-ETS time periods. If LFE families are physical asperities on the plate interface (e.g. mafic blocks (Fagereng et al., 2014) or subducted seamounts (Sweet et al., 2014)) it is possible that the entire asperity does not slip during every LFE. In particular, if the smaller M_c's during inter-ETS time periods are not an artifact of less background tremor, smaller sections of the overall LFE asperities could slip during inter-ETS time periods. Alternatively, the physical size of the asperity could change. But, this seems improbable on short time scales on the order of one year, the recurrence interval of ETS events in northern Cascadia. If LFEs were asperities created by differences in fluid distribution or frictional properties (Hawthorne & Rubin, 2013; Thomas et al., 2016), it seems more likely that asperity size could change over the course of a year.

It is also possible that the asperity area could appear larger during ETS episodes because more LFEs are active at the same time. If this were true, it would imply that when we observe an LFE with large moment, we are actually observing multiple LFEs. For the waveforms of

multiple LFEs to stack coherently, the LFEs would have to occur within 0.5 seconds of each other. We think that it is unlikely that LFEs occur so close together in time if LFEs occur randomly. If LFEs are triggered by other LFEs within ~0.1 second, it could appear as though LFEs are occurring simultaneously.

In contrast, if the size of LFEs were limited by slip area, there would have to be more slip per LFE during ETS events. Because LFE durations are the same regardless of moment (Bostock et al., 2015; Thomas et al., 2016), more slip requires higher slip rates. Rate and state models show that during ETS events there are higher stresses and slip rates at the rupture front (Hawthorne & Rubin, 2013). In addition, because stress is relieved more often down-dip between ETS events (Sweet, 2014; Wech & Creager, 2011), more stress is relieved up-dip during ETS events, possibly resulting in higher up-dip slip rates and more slip per LFE.

It is difficult to distinguish between these two models from the patterns in characteristic moment alone. But, Bostock et al. (2015) argues that the weak scaling between LFE moment and duration indicates that LFE moment is limited by slip area. Given this evidence, we too favor the area-limited model. Additionally, it is simpler to imagine some sort of barrier or difference in the frictional properties on the plate interface that prohibit rupture propagation than some physical process that limits slip.

4.3 Estimating the slip, patch width, and stress drop for an up-dip LFE family

For the discussion below we consider an up-dip LFE family (latitude=47.98, longitude=-123.21) during a single ETS event. We consider a single ETS event because there are good geodetic measurements of slip during ETS events. About 30 mm of slip occurred at this LFE family during the 2010 and 2012 ETS events beneath the Olympic Peninsula (Hall & Houston,

2014). Similar amounts of slip (20-40 mm) were observed in the region during ETS events that occurred from 1998-2008 (Schmidt & Gao, 2010; Wech et al., 2009a).

The LFE family has N_T LFEs. Each LFE has an unknown area (A_i) and slip (S_i) where i=1:N_T. The seismic moment for each LFE is:

$$M_i = \mu S_i A_i, \quad [8]$$

We measure the characteristic (mean) moment, $M_c = \frac{1}{N_T}\sum_{i=1}^{N_T} M_i$, for this LFE family. The total area of the LFE family patch, A_T, is unknown. We assume that the total slip, S_T, is the geodetically determined value of about 30 mm. The total moment release for this family is:

$$N_T M_c = \mu S_T A_T. \quad [9]$$

By rearranging this equation, we can solve for the total area of the LFE family patch using only measured parameters:

$$A_T = \frac{N_T M_c}{\mu S_T}. \quad [10]$$

For the LFE family mentioned above, N_T=300 and M_c= 1.8×10^{11}. Therefore, A_T=60 km^2 and the diameter of the LFE family patch is approximately 300 m. We admit that there are problems with estimating patch size using geodetic slip. First, our catalog is likely missing events, so N_T is likely greater than we observe. Second, it has been shown that only ~0.1% or less of the estimated geodetic moment is released seismically through tremor (Kao et al., 2010). Therefore it is possible that aseismic slip does occur within an LFE patch (e.g., Nakata et al., 2011).

To estimate the patch diameter, slip, and stress drops for individual LFEs, we consider two end-member models (Figure 2.10). In the first model (Figure 2.10a) each LFE ruptures the entire patch, so A_i=A_T for every LFE. In this case, the slip for each event follows an exponential distribution with a characteristic (mean) slip of $S_c = M_c/\mu A_T = S_T/N_T$.

In the second end-member model (Figure 2.10b), we assume each LFE ruptures a small subsection of the entire LFE family patch and that each sub-patch only slips once. Here, S_i=S_T for every LFE. Now, the rupture areas, A_i, follow an exponential distribution with characteristic (mean) area of $A_c = M_c/\mu S_T$.

The true behavior of LFEs most likely lies somewhere in between these two end-member models (i.e. Figure 2.10a and 2.10b). To describe this behavior, we define N as a proxy for the number of sub-patches where N=A_T/mean(A_i). While the end-members described above have N=1 and N_T sub-patches respectively, N can take on any value between 1 and N_T. While the maximum slip area for each LFE is limited by the overall size of the LFE-family patch (A_T), each LFE can rupture a smaller portion of the patch. The rupture areas for LFEs can overlap.

For a given value of N, we estimate the mean patch area (A_N), and corresponding patch radius (L_N), directly using the definition on N above. Our main assumptions are that (1) the LFE sub-patches are circular, and (2) the entire LFE family patch slips S_T during the ETS event. The latter assumption may be incorrect such that only a small portion of the LFE family asperity slips during LFEs, and that the rest of the asperity could be ductile. An example model (Figure 2.10c) is that the LFE family is characterized by a cluster of small unstable sub-patches (LFEs) embedded in a ductile background (e.g., Nakata et al., 2011). The ductile background slips silently while the LFE sub-patches each slip a total of S_T during LFEs. In this case, we interpret A_T as the sum of the areas of the unstable sub-patches and the area of the LFE family could be much larger if the percent of ductile area is large.

Because we know the values for S_T, N_T, and M_c (S_T=30 mm, N_T=300, and M_c= 1.8×10^{11} N-m), we can estimate A_N without making any additional assumptions. We also make crude estimates of mean slip per event (S_N), and stress drop ($\Delta\sigma_N$) assuming that all sub-patches are the

same size. This assumption is consistent with the observation by Bostock et al. (2015) that LFE duration is nearly independent of seismic moment. The assumption has a modest effect on S_N, but $\Delta\sigma_N$ depends strongly on this assumption. The equations for A_N, L_N, S_N, and $\Delta\sigma_N$ are:

$$\begin{aligned} A_N &= M_c/(\mu S_T)\ \ (N/N_T)^{-1} \\ L_N &= \mathrm{sqrt}(Mc/(\pi\mu S_T))\ (N/N_T)^{-1/2} \\ S_N &= S_T\ (N/N_T) \\ \Delta\sigma_N &= (\ 7/16)\ (Mc)\text{-}1/2\ \ (\pi\mu S_T N/N_T)^{1.5} \end{aligned} \qquad [11]$$

where the shear modulus, μ, is 30 GPa (Bostock et al., 2015).

To calculate the slip rate we use the equation $\dot{S}_N = S_N/\tau$ where the LFE duration, τ, is 0.5 s (Bostock et al., 2015). It is important to note that for "regular" earthquakes there are two timescales, the rise time, or the duration of slip at a single point on the fault, and the rupture duration, or the total amount of time it takes to rupture the entire fault surface. When estimating slip rate, we assume that measured duration, τ, is the rise time. Thomas et al. (2016) also makes this assumption when calculating slip rate for LFEs.

As N varies from 1 to N_T, we find that slip/LFE ranges from 0.1 to 30 mm, patch diameter ranges from 275 to 16 m, stress drop ranges from $3\text{x}10^4$ – $2\text{x}10^8$ Pa and slip rate ranges from 0.2 to 60 mm/s. If LFEs are allowed to slip on many (non-overlapping) sub-patches, LFE stress drops are much higher than suggested by both Bostock et al. (2015) and Thomas et al. (2016) (Table 1.1). Stress drops calculated when N>10 exceed 1 MPa, within the range of stress drops for "regular" earthquakes (Allmann & Shearer, 2009; Kanamori & Anderson, 1975a). Stress drops with N<3 are between 10 and 100 kPa, which is equivalent to estimated stress drops for Cascadia SSEs (10-100 kPa (Schmidt & Gao, 2010)). This observation indicates that either LFEs can have a large range of stress drops or that large numbers on non-overlapping sub-

patches within an LFE family patch is an unrealistic model. Slip rates calculated for the entire range of N are slower than slip rates during "regular" earthquakes, but faster than estimates of slip speed during slow slip events from geodetic inversions and used in slow slip models (~10^{-3}-10^{-4} mm/s (Bartlow et al., 2011; Colella et al., 2011, 2012; Rubin, 2011)).

Table 2.1 shows our estimates when N=1 compared to estimates from Bostock et al. (2015) and Thomas et al. (2016), who also assume N=1. Bostock et al. (2015) later relaxes the assumption that each LFE ruptures the entire LFE family patch, but we include their calculations for N=1 here because they are directly comparable to Thomas et al. (2016). The most notable difference between our results and Bostock et al. (2015) is that our patch width is smaller by a factor of 3. This makes sense because our LFE moments are smaller than those from Bostock et al. (2015) but our estimates of slip/LFE are similar. Our calculated slip, patch width, stress drop, and slip rate are similar to those estimates for LFE on the San Andreas Fault by Thomas et al. (2016).

Models with small values of N, say between 3 and 10, seem most plausible. It is often assumed, for simplicity, to be 1, but we think that it is unlikely that each LFE ruptures the entire patch for a given family. Additionally, previous work by Bostock et al. (2015) and Thomas et al. (2016) favor the idea that LFEs are low stress drop events. Following that conclusion, we think that it is unlikely that the stress drops for LFEs are as large as the stress drops for "regular" earthquakes. Hence values for N approaching 10 are increasingly less likely.

5 Conclusions

We calculate the seismic moments for 34,264 LFEs beneath the Olympic Peninsula, WA and find that the moment-frequency distribution for LFEs is best fit by an exponential distribution with a characteristic moment, M_c=2.05x10^{11}. We also find that the characteristic

moments for individual LFE families are larger during ETS events than during inter-ETS time periods, especially for updip LFE families. An exponential moment-frequency distribution implies that the source process for LFEs is scale-limited. We propose two end-member models: (1) where LFE size is limited by the amount of slip, and (2) where LFE size is limited by slip area. It is difficult to distinguish between these two models because the physical explanation for LFE asperities is still a topic of debate. Hypotheses include subducted seamounts (Sweet et al., 2014), rheological differences in the fault zone (e.g. mafic blocks) (Fagereng et al., 2014), or small areas governed by different frictional behavior than the surrounding region (Hawthorne & Rubin, 2013; Thomas et al., 2016). Given that the exponential moment-frequency distribution naturally provides a scale size for LFE moment and that LFE duration does not scale with moment (Bostock et al., 2015), we argue that LFE moment is limited by slip area, in agreement with Bostock et al. (2015).

Based on the observed exponential distribution of LFE moment and geodetically observed total slip we estimate that the total area that slips within an LFE family has a diameter of ~300 m. We also estimate the slip per LFE, patch width, stress drop, and slip rate for an updip LFE family during an ETS event. We allow for LFEs to rupture an overall LFE family patch with anywhere from 1 to 300 sub-patches and calculate the corresponding range of slips per LFE, patch diameters, stress drops, and slip rates. While estimated slip rates span orders of magnitude (0.2 – 60 mm/s), for all numbers of sub-patches, LFE slip rates are slower than those of "regular" earthquakes but faster than slow slip events. This supports the interpretation from Thomas et al. (2016) that LFEs are asperities within a slow slip region with frictional properties and variations in fluid pressure that allow for faster slip speeds. The range of stress drops is also large (3.0×10^4 – 1.6×10^8 Pa). When there are fewer sub-patches (<20) stress drops are smaller than "regular"

earthquakes, but in the range of stress drops estimated for slow slip events (10-100 kPa (Schmidt & Gao, 2010)). When there are many sub-patches, stress drops for LFEs are similar to those of "regular" earthquakes (~1 MPa or greater). The large variations in slip rate and stress drop imply that the number of sub-patches, N, is an important parameter to consider when quantifying LFE source properties. We believe that values for N between 3 and 10 sub-patches are reasonable since these values result in stress drops less than "regular" earthquakes. Though N=1 is often assumed for simplicity, we think it is unlikely that each LFE in a family ruptures the same patch. When we assume N=1 (each LFE ruptures the entire LFE family patch) our estimates of LFE source properties (slip/LFE≈0.1 mm, patch width=200 m, stress drop≈10 kPa, and slip rate=0.2 mm/s) are similar to values estimated for Vancouver Island (Bostock et al., 2015) and in the San Andreas Fault (Thomas et al., 2016).

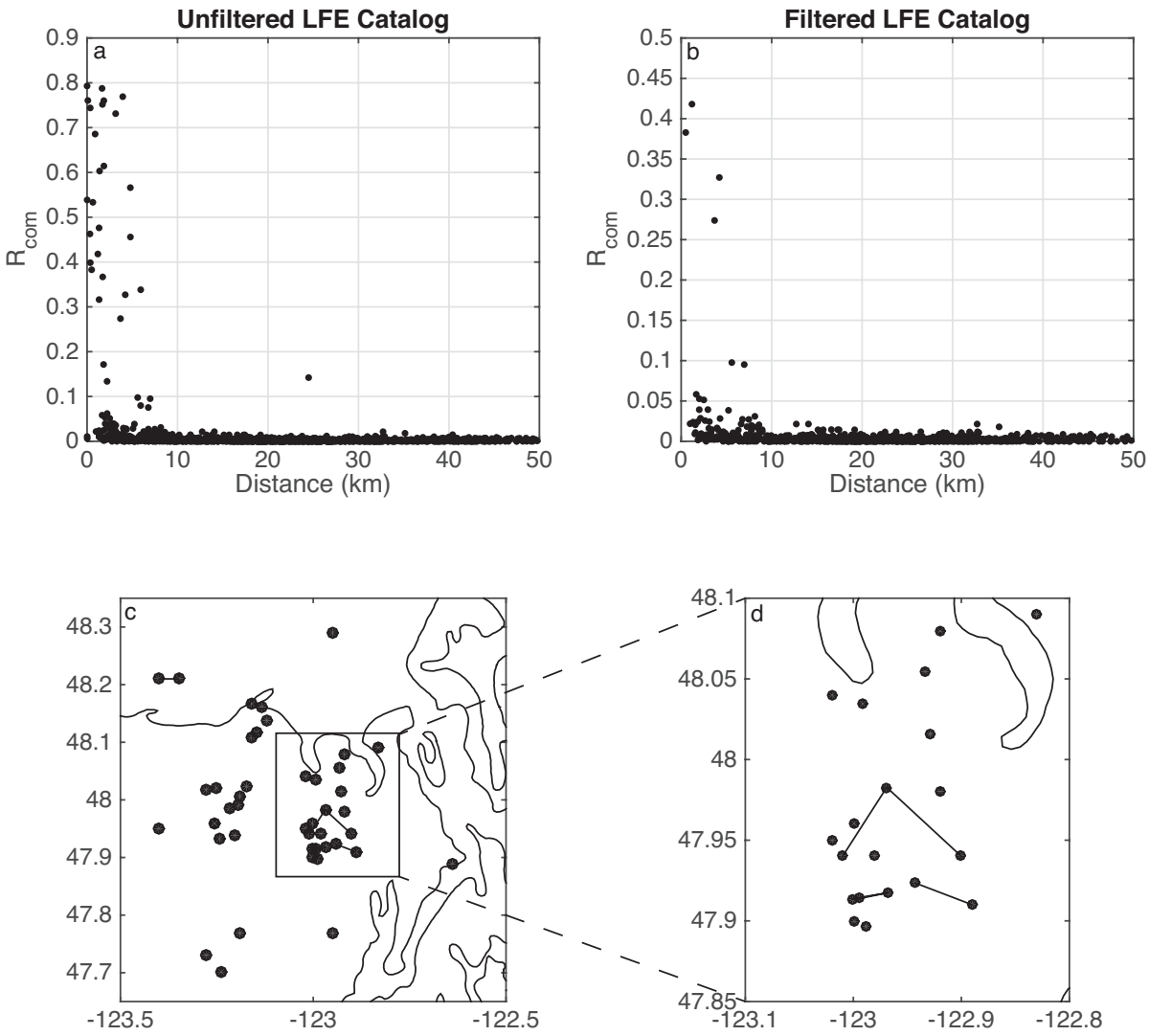

Figure 2.1: (a) R_{com} values of the unfiltered LFE catalog plotted against the distance between families. Only families located within 10 km of each other have high R_{com} values (R_{com}>0.2), or many overlapping detections. (b) Same as subplot (a), but for the filtered LFE catalog. (c) Map of LFE families beneath the Olympic Peninsula, WA. Families shown are from the filtered LFE catalog. Lines connect LFE families with R_{com} values greater than 0.05. (d) Zoomed in version of subplot (c).

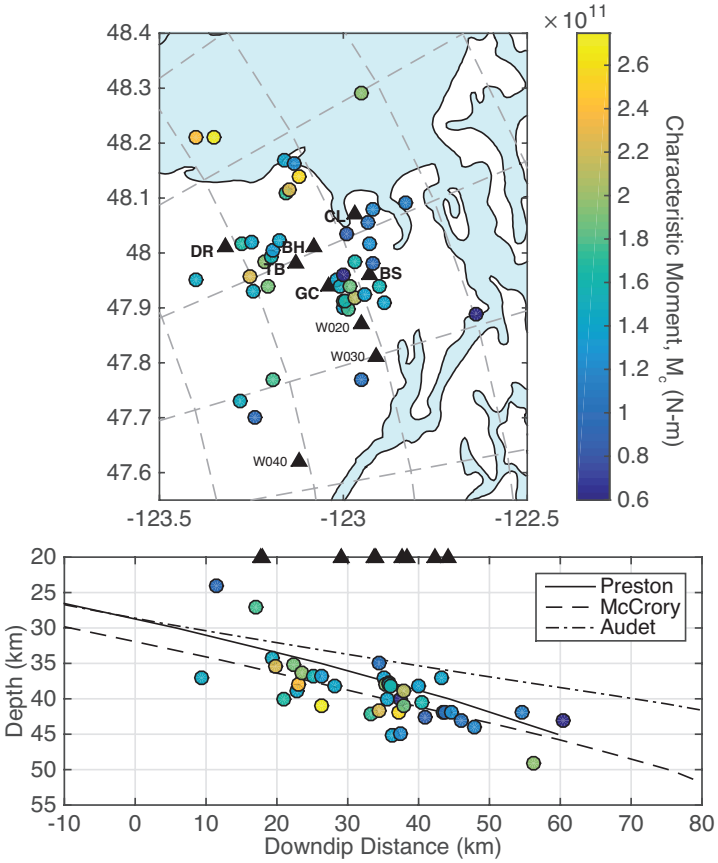

Figure 2.2: Map (top) and cross section (bottom) of LFE families (after sorting) beneath the Olympic Peninsula, WA. LFE families are dots, color-coded by characteristic moment ($\mathbf{M_c}$). The triangles are arrays from the AofA (bold labels) and CAFÉ (regular labels) experiments used to find LFEs, make LFE templates, locate LFEs, and calculate LFE moments.

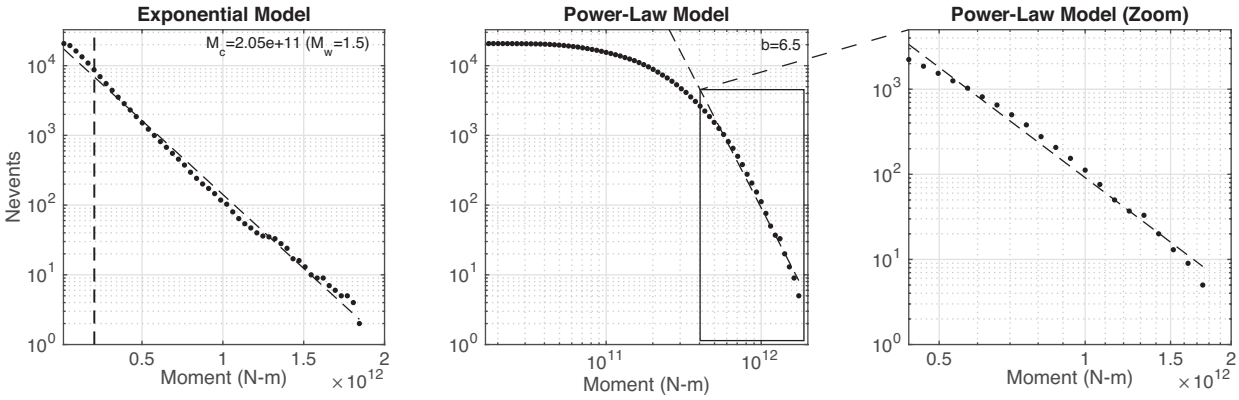

Figure 2.3: (a) Moment-frequency distribution for all LFEs in all families (dots) showing exponential fit (dashed line) with a slope corresponding to a characteristic moment M_c= 2.05×1011 N-m. Vertical dashed line shows the value of the characteristic moment. (b) Power-law fit for the LFE moment-frequency distribution. The distribution, restricted to the largest events, is best fit by a power-law curve with exponent, β=4.3 (dashed line), which corresponds to a b-value of 6.5. (c) Zoom of the power-law fit showing only Mo > 4.3×1011 N-m.

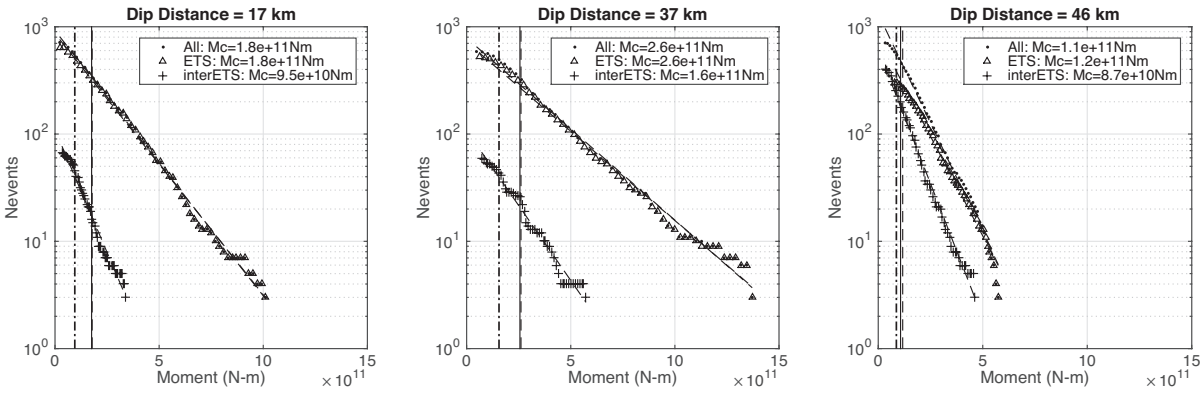

Figure 2.4: Exponential moment-frequency distributions for three LFE families ordered from updip (left) to downdip (right) showing LFEs during all time periods (dots), during ETS events (triangles) and during inter-ETS times (crosses). The vertical solid lines, dashed lines, and dot-dashed lines respectively are the characteristic moments for all time periods, ETS events, and inter-ETS time periods respectively. Figure A1.1 shows the same type of plots for more LFEs families.

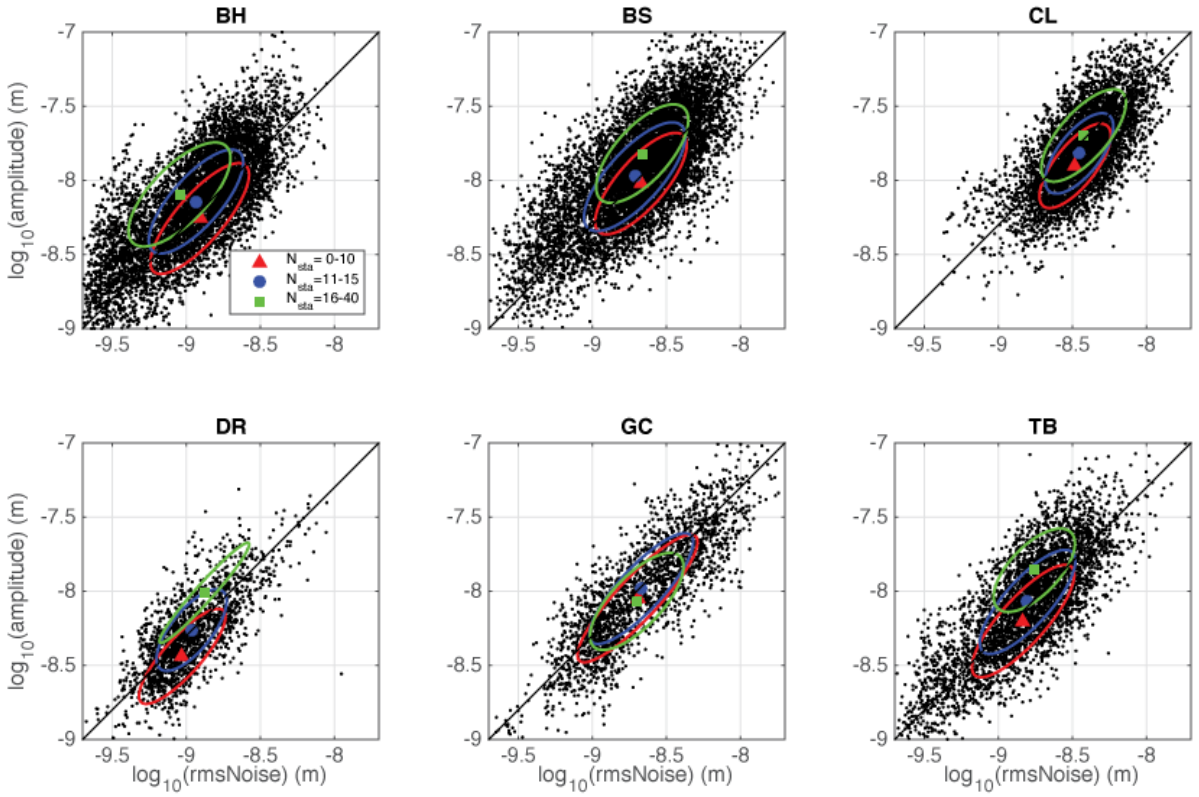

Figure 2.5: Displacement amplitude of LFEs in a single LFE family plotted against the RMS noise of a 1-minute window prior to the detection for each station/horizontal channel pair in each array. The symbols and surrounding ellipses represent the centroid and covariance ellipses of these data corresponding to aligned observations with 10 or fewer channels (red triangles), 11-15 channels (blue circles) and more than 15 channels (green squares). With the exception of the Gold Creek (GC) array, the SNR is better when there are more stations.

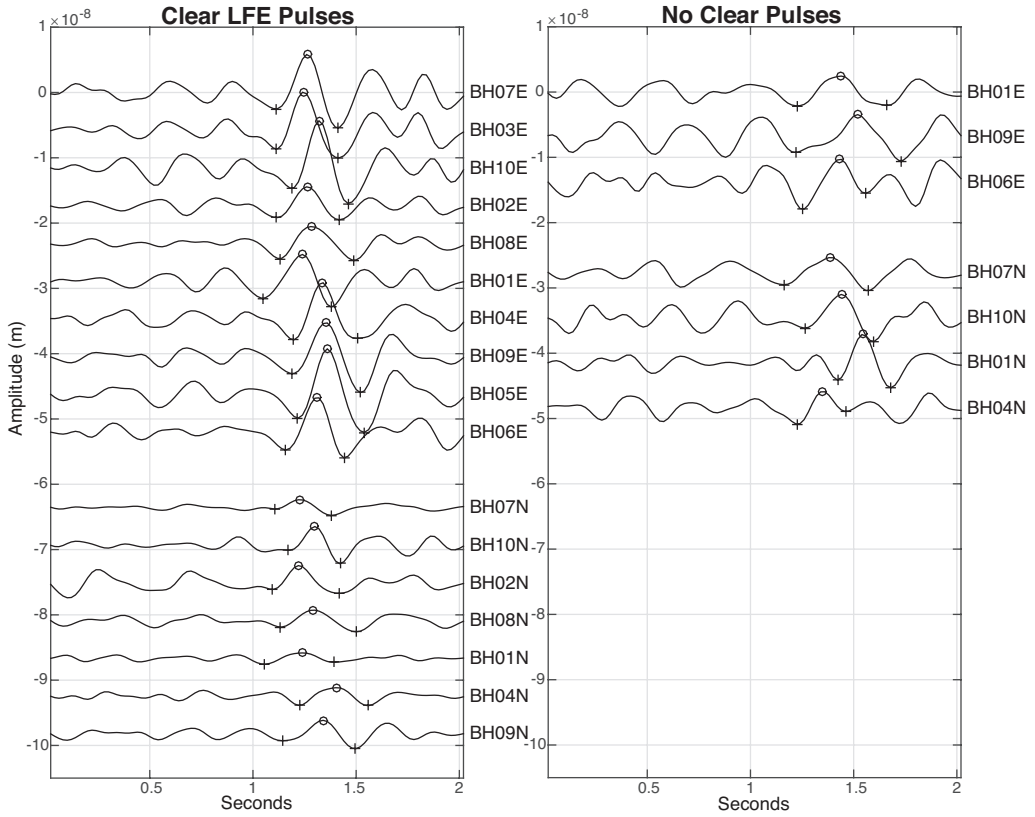

Figure 2.6: (left) Example of unstacked, LFE shear wave displacements from a single LFE (2009/10/31 22:39:22.4) on 17 channels from the Burnt Hill (BH) array. Displacement waveforms are deconvolved and bandpass-filtered between 2 and 8 Hz. Waveforms show clear, impulsive arrivals. East channels are on the top, north on the bottom. Circles show the maximum shear wave amplitude within the 2-second window and the crosses show the minima on either side of the maximum. (right) Example of displacement waveforms for a different LFE (2009/11/12 13:17:39.7) at Burnt Hill without clear, impulsive shear wave arrivals. There are only 7 channels with time-consistent peak amplitudes.

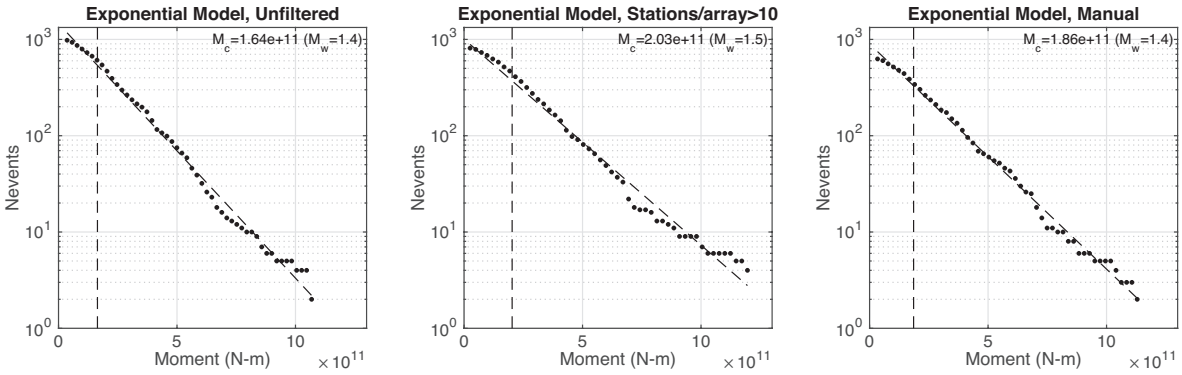

Figure 2.7: Exponential fits for the unfiltered LFE moments (left), LFE moments calculated only using arrays with 10 or more observations (middle), and LFE moments calculated with manually picked high SNR arrays (right). The sloped and vertical dashed lines indicate the best exponential fit and the value of the characteristic moment respectively.

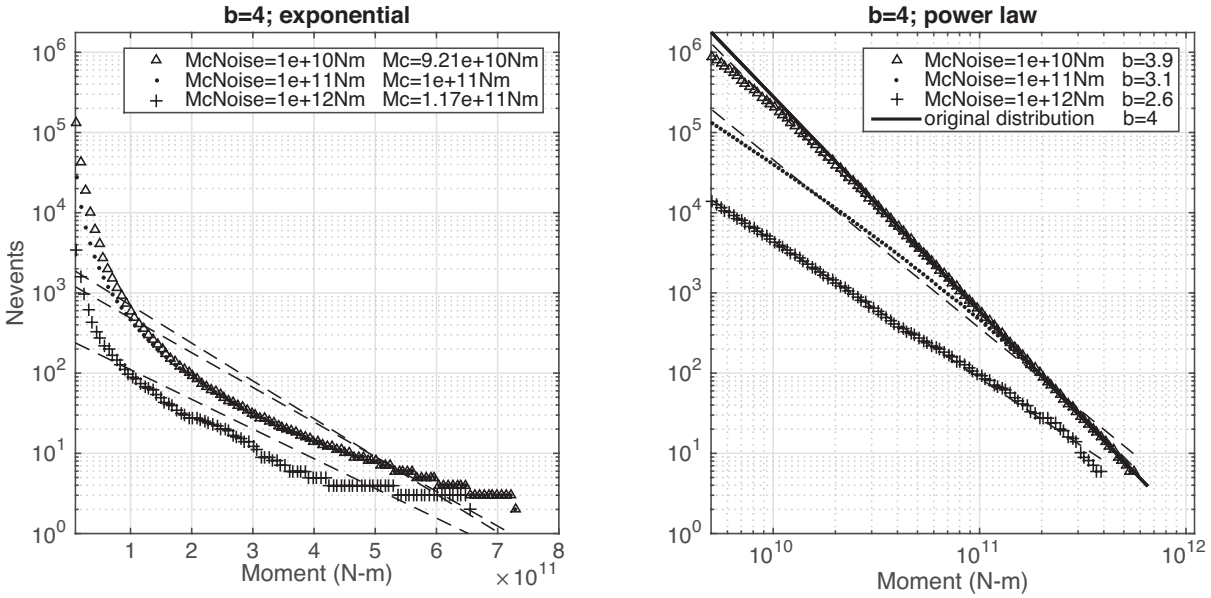

Figure 2.8: Consider a synthetic LFE catalog with a power-law distribution and b-value of 4 (β=2.67) and maximum LFE size of 1.8x1012 N-m (solid line, right plot). The probability of detecting any of the LFEs in this catalog is given by an exponential noise distribution with characteristic noise levels of Mc = 1010, 1011, 1012 N-m. The resulting three filtered catalogs are indicated by the symbols in the legends. The three filtered catalogs are fit to exponential distributions (left), which do not explain the noisy catalogs well and to power-law distributions (right), that do fit the noisy catalogs. As the noise level increases, the apparent b-value decreases, but the filtered catalog continues to exhibit a power-law distribution.

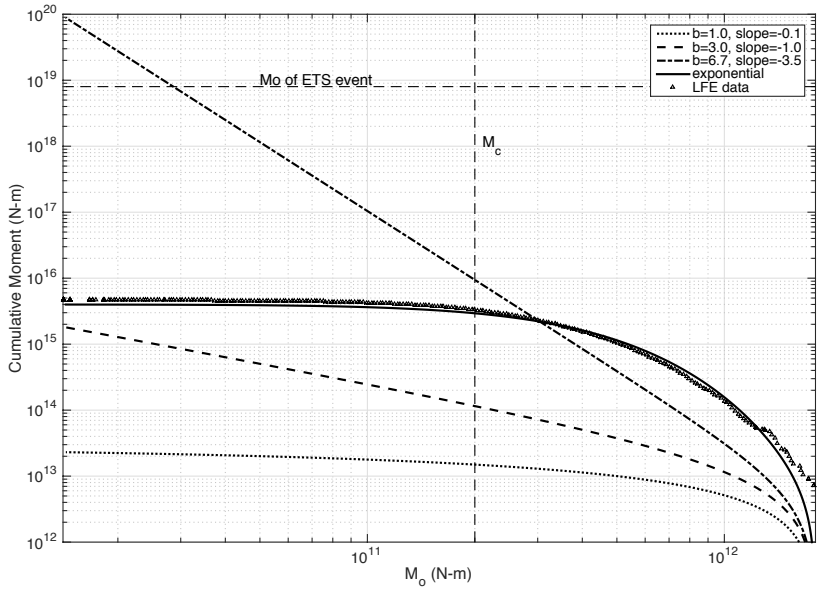

Figure 2.9: Cumulative moment release by all LFEs above a given moment, Mo, assuming a complete catalog of LFEs for power law moment frequency relationships with b values of 1, 3, and 6 and for the exponential moment-frequency relationship that best fits our LFE catalog (M_c= 2.05×1011).

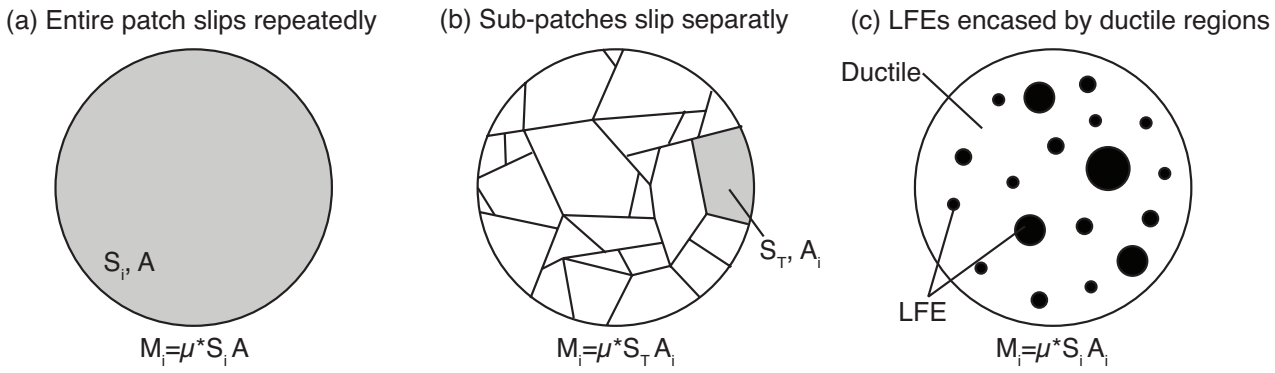

Figure 2.10: Cartoon of end member LFE rupture models: (a) where each LFE ruptures the entire LFE family patch, (b) where each LFE ruptures a separate sub-patch, and (c) where LFEs are encased in a ductile matrix. The large circles in (a) and (b) represent the total LFE family patch area, AT. In (c), AT is the summed area of the small, black circles.

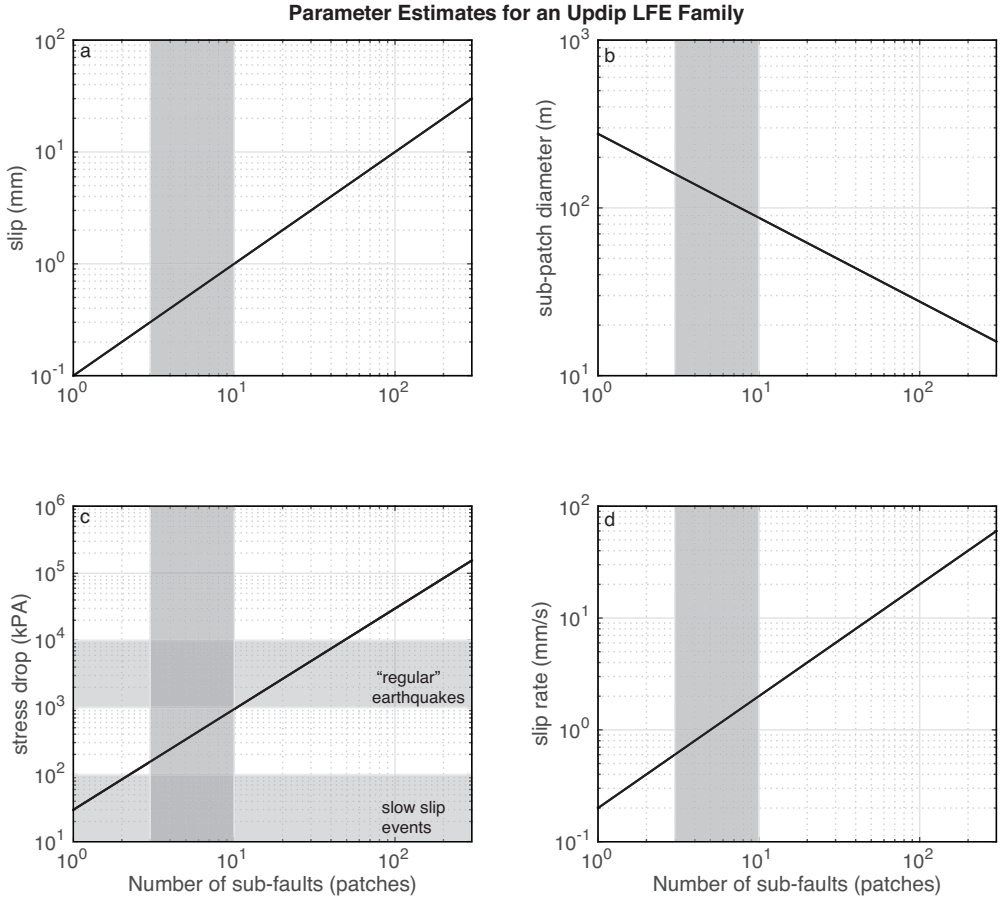

Figure 2.11: Estimates of (a) slip per LFE, (b) sub-patch diameter, (c) stress drop, and (d) slip rate for an updip LFE during an ETS event for N=1-300. Vertical gray bars show values when 3≤N≤10. The horizontal gray bars in subplot (c) show the ranges of stress drops for "regular" earthquakes and slow slip events. For our calculations, we assume that 3 cm of slip happens on the LFE family patch in total during the ETS event, the mean moment of each LFE is 1.8×1011 N-m, the duration of each LFE is 0.5 s, and the shear modulus is 30 GPa.

Table 2.1: LFE Source Parameters

	This work (N=1)	Thomas et al. [2016]	Bostock et al. [2015]
Slip/LFE (mm)	0.1	0.05	0.12
Patch Diameter (m)	275	200	600
Stress Drop (Pa)	3×10^4	$\sim10^4$	1.53×10^4
Slip Rate (mm/s)	0.2	0.24	0.25

A model for low-frequency earthquake slip

The content of this chapter is in review for publication in *Geochemistry, Geophysics, Geosystems*.

1 Introduction

Low-frequency earthquakes (LFEs) are distinct, repeating earthquakes that are embedded within tectonic tremor (Shelly et al., 2007). LFEs group into LFE families, or clusters of LFEs that repeat on small ~1 km^2 patches on the plate interface (Sweet et al., 2014). LFE family patches are thought to be localized asperities that release observable seismic energy during slip (Beeler et al., 2013; Shelly et al., 2007). Both LFEs and tremor occur during slow slip events (SSEs) in subduction zones worldwide (e.g. Nankai (Shelly et al., 2006), Cascadia (Bostock et al., 2012; Peng & Rubin, 2016; Plourde et al., 2015; Royer & Bostock, 2014; Rubin & Armbruster, 2013; Sweet, 2014; Thomas & Bostock, 2015), the Aleutians/Alaska (Brown et al., 2013;Wech, 2016), and Mexico (Frank et al., 2013)) and some strike-slip settings (e.g. Parkfield (Shelly, 2010) and the Alpine Fault, New Zealand (Chamberlain et al., 2014; Wech et al., 2012)) and are used as indicators for when and where slow slip is occurring. Both LFEs and tremor are active during northern Cascadia episodic tremor and slip (ETS) events (M6.0-6.5, 4-week-duration SSEs that occur every 14 months) and during inter-ETS time periods. Because, LFEs have identifiable P- and S-wave arrivals and therefore can be located more accurately and with higher temporal resolution than tremor. As a result of these qualities, LFEs are more precise slip indicators than tremor.

LFEs are commonly used to identify when and where slow slip occurred, especially for slow slip events that are too small to be observed geodetically (Frank et al., 2015). Most recently,

using LFEs to constrain the timing of slow slip loading, Frank (2016) showed that slip must occur between geodetically observed SSEs. Despite the utility of LFEs, an understanding of how slip occurs on LFE family patches is limited. How much slip occurs per LFE and over what area? Do all LFEs within an LFE family rupture the exact same spot within an LFE family patch? These types of questions have only been partially addressed by existing research.

While multiple studies found that slip per LFE is 0.05-0.1 mm and the rupture diameters of LFEs range from 200-600 meters (Bostock et al., 2015; Chestler & Creager, 2017; Thomas et al., 2016), a robust model for how slip occurs within an LFE family patch has yet to be determined. Additionally, calculations made in these papers are based on the assumption that all LFEs rupture the same patch, which we do not favor (see next paragraph). Chestler and Creager (2017) show that the moment-frequency distribution of LFEs, including LFEs in individual LFE families, is exponential. This differs from the power-law moment-frequency distribution for "regular" earthquakes. While Bostock et al. (2015) favors a power-law distribution for LFEs beneath Vancouver Island, they acknowledge that the power-law distribution breaks down for smaller LFEs. We prefer an exponential distribution because it fits the data nicely (Chestler and Creager, 2017). An exponential moment-frequency distribution for LFEs indicates that there is characteristic (mean) moment (M_c) for each family. The number of LFEs that exceed moment M_o is $N_T e^{-M_o/M_c}$ where N_T is the total number of LFEs.

Based on the observation that LFE families have characteristic moments, Chestler and Creager (2017) proposed three end-member models for LFE slip (Figure 3.1). Before discussing the three conceptual models we define a few terms. A_P is the area of the LFE family patch and is measured by the spread of relative LFE locations. It is the same for all 3 models. Similarly, the total summed seismic moment, which is estimated using the statistics of the exponential

distribution, is the same for each model. A_T is the total area that slips during LFEs, S_T is the total amount of summed slip on an LFE family patch or sub-patch during an ETS event, and S_{ETS} is the geodetically observed amount of ETS slip.

For model 1, each LFE slips over the entire patch so the total slipping area A_T equals A_P. The summed slip S_T is much less than S_{ETS} and is assumed to be uniform over A_P.

For model 2, the connected patch model, the total summed slip (S_T) is also assumed to be uniform over the entire patch (A_P), but it occurs over multiple sub-patches. Like model 1, A_T=A_P and S_T, which is much less than S_{ETS}, is the same for models 1 and 2. Model 1 is a special case of model 2 assuming only one sub-patch. At any point within the family patch only a small fraction of the slip produces LFEs, the vast majority of slip is ductile.

For model 3, the ductile matrix model, the sum of slip in the black regions (Figure 3.1c) is assumed to be the total geodetically determined slip (S_{ETS}), while the white regions contain no LFE slip; slip is entirely ductile there. In this case, we assume that S_T equals S_{ETS} but A_T (area in black) is much less than A_P.

Chestler and Creager (2017) conclude that LFEs likely rupture multiple sub-patches (approximately 3-10), and hence favor models 2 and 3. But, they did not attempt to differentiate between these two models.

In this paper, we evaluate models 2 and 3, which we will refer to as the connected patch model and the ductile matrix model respectively, and determine which model best represents slip within an LFE family. To do this we compare the LFE slip area (A_T), or the area that slips during LFEs, to the LFE family patch area (A_P) for multiple LFE families. For the ductile matrix model, assuming S_T=S_{ETS} , we estimate A_T by the summed seismic moment release of LFEs and S_{ETS} and find that for every LFE family A_T<<A_P. For the connected patch model, we estimate S_T by

the summed seismic moment and the known slip area A_T=A_P and find that for every family S_T<<S_{ETS}. The remainder of the geodetically observed slip occurs ductiley.

Furthermore, we investigate the patchiness of LFE families. Are there places within the slow slip zone that slip without radiating energy in the form of observable, repeating LFEs? Both LFEs (Bostock et al., 2012; Chestler & Creager, 2017; Y. Peng & Rubin, 2016; Royer & Bostock, 2014; Rubin & Armbruster, 2013) and tremor (Ghosh et al., 2012) catalogs from northern Cascadia are patchy. Regions with no observed LFE families surround spots where many LFE families are clustered close together. Similarly, there are patches with higher tremor densities and moment rates compared to the surrounding areas (Ghosh et al., 2012). In this work, we systematically search for new LFE families beneath the Olympic Peninsula, Washington where, so far, no LFE families have been observed. Our goal is to deduce whether the spatial gaps between LFE families are real or if they are a result of the methods used to search for LFEs. (i.e cross-time autocorrelation (e.g., Bostock et al., 2012; Brown et al., 2008), cross-station correlation (Peng & Rubin, 2016; Rubin & Armbruster, 2013), and searching for repeating peaks in seismic energy (e.g., Chestler & Creager, 2017; Frank et al., 2014). Existing methods used to find LFEs may preferentially find events with higher signal to noise ratios (SNRs). LFEs with amplitudes closer to the amplitude of the background noise could go undetected. To search for new families, we focus on time periods when tremor occurs in patches without LFE families or during inter-ETS time periods when there is more downdip LFE activity (Sweet, 2014).

Finally, we show that the characteristic (mean) moment of LFE families decreases with downdip distance. Additionally, while the number of LFEs during ETS events is constant with downdip distance, the total number of LFEs (including those that occur during inter-ETS time periods) increases.

2 Methods

2.1 LFE catalog and searching for new families

We employ the LFE catalog from the Olympic Peninsula, Washington assembled by Chestler and Creager (2017). The catalog was created using high signal-to-noise waveforms calculated by Ghosh et al., (2012) using multibeam-backprojection and consists of 32,387 unique LFEs sorted into 43 LFE families. Chestler and Creager (2017) created their catalog by searching for repeating peaks in tremor during the 2010 and 2011 ETS events. They use the peaks found during ETS events to create the initial templates that are then scanned during the entire AofA time period to find additional LFEs. For this work, following a similar methodology to Chestler and Creager (2017), we found an additional 6 LFE families by targeting the search for new LFEs (1) during times when tremor, identified by Ghosh et al. (2012), is located in spatial gaps in the Chestler and Creager (2017) catalog and (2) during inter-ETS time periods when there is more downdip LFE activity (Sweet, 2014). We located the new LFE families and calculated the band-limited moments of LFEs following methods from Chestler and Creager (2017). After removing duplicate families and sorting LFEs uniquely into families the updated LFE catalog includes 39,966 LFEs sorted into 45 families (Figure 3.2). Figure A2.1 shows the time history of the catalog.

2.2 Calculating Slip Area

We calculate the ETS slip area (A_T), or the total area over which LFEs slip, for LFE families following the methodology outlined by Chestler and Creager (2017). Consider one LFE family during an ETS event. The LFE family has N_T LFEs and each LFE has unknown area (A_i) and slip (S_i) where i=1:N_T. The seismic moment for each LFE is:

$$M_{o_i} = \mu S_i A_i, \quad [1]$$

where μ=30 GPa is the shear modulus. Assuming that LFEs in the family follow an exponential moment-frequency distribution (Chestler & Creager, 2017),we measure the characteristic (mean) moment, $M_c = \frac{1}{N_T}\sum_{i=1}^{N_T} M_{o_i}$, for this family. We define the total area that slips producing LFEs as A_T, and assume that within that area the summed slip, S_T, is uniform. The assumption for the connected patch model is that A_T=A_P, which is known. For the ductile matrix model, A_T is the unknown area of the black regions in Figure 3.1c and S_T=S_{ETS} is total amount of slip that occurs during the 2010 and 2011 ETS events. Here, we consider a 2-D model, for which these assumptions are valid.

GPS slip inversions (Hall & Houston, 2014; Schmidt & Gao, 2010; Wech et al., 2009) show that approximately 3 cm of slip occurs during ETS events in the updip portion of the slow slip zone beneath the Olympic Peninsula and that slip decreases with downdip distance. Figure A2.6, which shows the summed slip during the 2010 and 2011 ETS events (Hall & Houston, 2014) at the location of each LFE family, confirms that S_{ETS}≈6 cm for the updip families. At the most downdip LFE family the summed slip is <1 mm. We believe that the GPS slip at the locations of downdip LFE families is poorly constrained for multiple reasons: (1) small slips are difficult to resolve, (2) model resolution is poorer downdip due to the greater distance between the GPS stations and the plate interface (Hall, personal communication), and (3) the slip gradient is sensitive to the smoothing used in the slip inversion. Therefore, while we believe it is safe to use S_{ETS}≈6 cm for updip LFE families, we do not think it is appropriate to use the GPS-estimated slip for downdip families. Smoothing does affect GPS-estimated slip at the location of all LFE families, but because slip estimates are at least 60 times smaller for downdip families than updip families, errors due to smoothing are proportionally larger for downdip families. To account for

the decrease in ETS slip with downdip distance we scale S_{ETS} for each LFE family by the proportion of tremor that occurs during ETS events verses all time periods at the LFE family's location (Wech & Creager, 2008). We use tremor rather that LFEs because the tremor catalog is not spatially sensitive to the locations of the AofA stations. The proportion of tremor that occurs during ETS is roughly proportional to N_T/ N_T^{all} (Figure A2.6), where N_T is the number of LFEs that occur during ETS events and N_T^{all} is the total number of LFEs in the family. For example, if 50% of the tremor at the LFE family location occurs during ETS events, then S_{ETS} for that family would be 6×0.5=3 cm. The assumption of this scaling method is that the total amount of slip that occurs at each family is uniform in space (i.e., that over all time periods (ETS and inter-ETS) the same amount of slip occurs everywhere within the slow slip zone).

In both the connected patch and ductile matrix models we assume that the total summed slip, S_T, is uniform within A_T and the total summed seismic moment is given by:

$$N_T M_c = \mu S_T A_T. \quad [2]$$

For the ductile matrix model, characterized by regions with no LFEs (white regions of Figure 3.1c) and with 100% of slip from LFEs (black regions), we can calculate the total slip area A_T from measured parameters (N_T, M_c, and S_T=S_{ETS}):

$$A_T = \frac{N_T M_c}{\mu S_{ETS}}. \quad [3]$$

Using this method, we estimate the slip area for all 45 LFE families during ETS events. Table A2.1 includes the N_T, M_c, and calculated A_T for all LFE families.

Similarly, for the connected patch model we can equate A_T to the observed value for A_P to determine S_T from known parameters (N_T, M_c, and A_T=A_P):

$$S_T = \frac{N_T M_c}{\mu A_P}. \quad [4]$$

The fact that LFEs follow an exponential moment-frequency distribution is critical for these calculations. An exponential distribution implies that LFE moments are scale-limited, and hence have a characteristic size. On the other hand, a power-law moment-frequency distribution, observed for "regular" earthquakes, implies that moment is scale invariant. For a power-law distribution there is no characteristic moment.

2.3 Calculating Patch Size

We calculate the patch size for 25 LFE families, located in the boxes in Figure 3.2, by inverting for relative LFE locations using the double difference method (hypoDD, Waldhauser, 2001). The double difference technique minimizes the residuals between observed and predicted travel time differences (or double differences) for pairs of nearby events observed at a common station. The hypoDD algorithm minimizes the residuals for event pairs at each station by weighted least squares using either singular value decomposition (SVD) (for small systems) or the conjugate gradients method (LSQR, Paige & Saunders, 1982) (for large systems). We invert high-precision differential P- and S-wave travel times between event pairs for relative LFE locations using the LSQR method. Differential travel times are calculated by cross-correlating LFE waveforms on 6 arrays (10-20 stations per array) and 3 individual stations. Cross-correlating P- and S-waveforms on vertical and horizontal channels respectively give precise lag times between phase arrivals for event pairs.

We relocated 1586 events that correlate with their family templates with mean correlation coefficients greater than 0.18. LFEs with higher correlation coefficients generally have cleaner waveforms, which result in better travel-time picks. The parameters used to perform the hypoDD inversion are summarized in Table A2.2. Parameters were chosen to optimize the least squares inversion and include a maximum separation distance for event interaction (4 km) that ensures

that LFEs only interact with other LFEs with similar waveforms. As a result, events without neighboring LFEs within 4 km are automatically removed.

Before relocation, we initially assumed that all LFEs in a particular LFE family occur at the location of the LFE family. To reassure ourselves that this assumption did not bias the double difference results, we performed two different relocations (1) where each LFE starts at its LFE family location, and (2) where LFEs are randomly assigned to starting locations within a 6.5 by 6.5 km grid centered around the original LFE family location (Figure A2.2). For both relocations (using both types of initial LFE locations) we iterate the hypoDD inversion five times. Each time we use updated locations and origin times from the previous iteration to recalculate differential travel-time picks. To avoid errors due to cycle skipping, we limit the allowed lag times, calculated by cross correlation, to +/- 0.3 s or 0.4 s during the first 4 iterations. This allows poorly located LFEs to stabilize. For the last iteration, we decrease the cutoff value to to 0.2 s to better eliminate cycle skipping errors. Because both relocation methods yield similar results, we will only discuss results from the latter relocation method (i.e., where LFEs start at randomly assigned locations).

To calculate the patch area, for each LFE family we convert the LFE longitude, latitude, and depth to Cartesian coordinates, remove the mean locations (centroids) and calculate the 3-D covariance matrix **C** (second moment about the centroid). If the LFE locations have a Normal distribution, then we would expect 95% of the locations to lie within the 95% confidence ellipsoid defined by:

$$\boldsymbol{X}^T \boldsymbol{C}^{-1} \boldsymbol{X} < \Delta^2 \qquad [5]$$

where $\Delta^2 = 7.81$ is the 95th percentile of the chi-squared distribution with three degrees of freedom and **X** is a location vector relative to the centroid. We remove the LFEs that lie outside

this ellipsoid and recalculate the centroid and error ellipse of the reduced data set and repeat three times until the centroid is stable. Using the stabilized centroids as the mean locations, we recalculate the 3-D covariance matrix. For each family, we determine the value of Δ^2 corresponding to the confidence ellipsoid that includes 60-80% of all the events. We believe that tossing 20-40% of events is reasonable due to the low signal-to-noise levels of LFE waveforms in Cascadia (see section 3.2 for further justification). We define the patch area, A_P, as the area of the 2-D horizontal confidence ellipse for that surrounds 95% of the remaining LFEs (Δ^2 = 5.99):

$$A_P = \pi(\Delta * \sigma_1)(\Delta * \sigma_2). \quad [6]$$

σ_1 and σ_2 are the standard deviations in the horizontal principal directions.

3 Results

3.1 LFE slip area

Assuming the ductile matrix mode, the slip areas (A_T) for LFE families during ETS events range from 0.1-1×10^5 m^2. Both the characteristic moments (M_c) of LFE families for LFEs during all time periods and just ETS events decrease with downdip distance (Figure 3.3b). The M_c's of LFE families for all time periods range from 2.7×10^{11} N-m (updip) to 0.6×10^{11} N-m (downdip) and ETS M_c's range from 2.8×10^{11} N-m (updip) to 0.4×10^{11} N-m (downdip). During ETS events there are 200-600 LFEs per family, but there is no obvious downdip trend. In the overall catalog (i.e. including inter-ETS time periods) there are many more LFEs in downdip families (800-1200) than in updip families (200-600) (Figure 3.3c).

3.2 Patch Size

We relocated 1263 LFEs within 18 LFE families from the east (downdip) cluster and 323 LFEs within 9 LFE families from the west (updip) cluster. After relocation 1222 (97%) and 284 (87%) LFEs remained in the east and west clusters respectively. More LFEs (~30% of LFEs

from each family) were removed when calculating patch area. Relocated LFEs for the east and west clusters are shown in Figures 3.4 and 3.5 respectively, as well as the 95% confidence intervals (solid lines) that define the patch size for each family. For most families, LFEs formed distinct clusters around the family centroids. Families without a distinct cluster around the centroid (6 out of 25 families) were not analyzed, but are still shown in Figures 3.4a and 3.5a. Within these families all LFEs are widely scattered. The values for A_P range from 0.3-2.0×10^6 m^2, corresponding to patch diameters (D_P) of 600-1600 meters. The ellipses that define A_P contain ~60-80% of the initial LFEs, producing tight clusters. The remaining LFEs (small dots) are scattered broadly and their locations are likely poorly constrained. When LFEs are binned by distance from their centroid (Figure A2.3), the distribution is Gaussian near the centroid and nearly uniform farther from the centroid. This indicates that the LFEs far from the centroid are evenly and randomly distributed. In addition, we calculate the mean horizontal uncertainties for LFEs grouped into 0.5 km bins of distance from centroid. Mean horizontal uncertainties increase with distance from centroid. This is evidence that the locations of LFEs outside their family clusters are poorly constrained.

Unfortunately, one of the downsides of using the LSQR method to perform the hypoDD inversion is that the LSQR method grossly underestimates errors. To estimate errors, we relocated a small subset of events (LFEs in the cyan family in Figure 3.4) using the SVD method. For the LFEs in the cyan family, the median horizontal errors are 60 and 50 meters in the x- and y-directions respectively and 30 meters in depth. This indicates that values for D_P could be 100 m smaller than we observe (patch radii, or horizontal standard deviations, could be 50 m smaller).

Because patch diameters are 7-20 times larger than the horizontal uncertainties estimated via the SVD method, we believe that the spread in LFE locations is real. This implies that LFEs do rupture separate sub-patches (e.g., ductile matrix and connected patch models; Figures 3.1b and 3.1c). This supports the conclusion from Chestler and Creager [2017], that it is unlikely that LFEs within an LFE family rupture the exact same spot. There are examples of "regular" earthquake clusters (e.g. clusters of earthquakes in the San Andreas Fault (Nadeau et al., 1995)) that occur over much smaller patch areas with diameters of less than 100 meters. These earthquakes are almost always the same size and repeat at regular time intervals. Conversely, LFEs within an LFE family have a range of sizes (Chestler and Creager, 2017) and occur in clusters that are irregularly spaced in time. We therefore believe that our LFE families behave differently than these repeating, "regular" earthquakes.

3.3 Spatial Gaps: comparison between LFE catalogs

As mentioned in section 2.1, we found 6 new LFE families located on the downdip edge of the families from the Chestler and Creager (2017) catalog. The new families are all located within ~5 km of previously identified LFE families and hence do not fill the spatial gaps in our catalog. We found no additional families within the gap beneath the TB and BH arrays, where we searched specifically, despite the fact that this is where resolution should be the greatest. While approximately 10 out of the 45 families in our catalog are located away from other LFE families, the majority of LFE families are grouped in clusters 4-15 km in diameter. After relocation, LFEs remain clustered into families, even when family centroids are only 2-3 km apart (Figures 3.4 and 3.5). There is one instance in the east cluster where LFEs from two families (dark purple and dark green in Figure 3.5) completely overlap. These two families are likely one LFE family rather than two separate families.

We compare the LFE family locations in our catalog to the locations of LFE families from Royer et al., (2015) and short-window detections from Peng and Rubin (2016), which are akin to LFEs (Figure 3.6). Royer and Bostock (2014) created a catalog of LFEs beneath Vancouver Island, Canada and northern Washington, using data in northern Washington from the Plate Boundary Observatory (PBO) borehole stations, the CAFE and FACEs experiments, and the Pacific Northwest Seismic Network permanent stations. Because they use stations located over a larger area than the AofA stations, their catalog spans a much greater area than our catalog. Royer et al. (2015) used an updated version of the Royer and Bostock (2014) catalog. Despite that we use different stations than Royer et al. (2015), patterns in LFE family locations beneath the Olympic Peninsula are similar. Beneath the AofA, families are more or less uniformly distributed within the slow slip zone. The exception is a prominent gap beneath the TB and BH arrays. There are very few downdip LFE families.

The locations of LFE families in this work are less similar to the locations of short-window detections from Peng and Rubin (2016) (grey dots in Figure 3.6). For example, in the vicinity of our dense, west cluster of LFE families (near the BS array) there are fewer short-window detections than in other regions. There are also short-window detections in many areas where there are no LFE families. Differences in absolute location are likely a result of the different location methods and number of stations used. The locations of short-window detections (Rubin & Armbruster, 2013) and LFE families (Bostock et al., 2012) beneath Vancouver Island also differ.

One feature that is common between all three catalogs is the gap in activity east of the TB and BH arrays. There, short-window locations from Peng and Rubin (2016) are significantly less dense and there are no LFE families. Additionally, there is very little activity downdip of the BS

array in all three catalogs. The exception is the unique LFE family that is situated significantly downdip of the other families. This very active family has been studied thoroughly by Sweet et al. (2014)

In the supplementary materials, we compare LFEs to tremor from both the Ghosh et al. (2012) (Figure A2.5) and Wech et al. (2008) (Figure A2.8) catalogs. The Ghosh et al. (2012) catalog also has a gap beneath the TB and BH arrays. Interestingly, LFE family locations, especially those within the east cluster, correlate with the high-density tremor areas from the Wech et al. (2008). Conversely, the regions from the Wech et al. (2008) catalog with low tremor densities are also areas where there are no LFE families. This suggests that in the areas without LFEs there is also very little tremor.

4 Discussion

4.1 A model for slip within a LFE family

For the 19 LFE families for which we calculated A_P, A_T calculated for the ductile matrix model is only 2-10% of A_P. The area of the black regions relative to white in Figure 3.1c is 0.02 to 0.1. LFE relative location errors of order 100 m indicate A_P could be overestimated, but the error in estimates of area (A_P) are typically less than 10%, which is relatively insignificant given that $A_p >> A_T$. We favor the ductile matrix model (Figure 3.1c) proposed by Chestler and Creager (2017), where, within an LFE family patch, a ductilely deforming matrix surrounds LFEs. Admittedly, this is an end-member model and the truth is likely a mix of our two models.

The ductile matrix model aligns with models of LFE slip proposed in studies of exhumed shear zones (Collettini et al., 2011; Compton et al., 2017; Fagereng, 2011; Fagereng et al., 2014; Fagereng & Sibson, 2010; Hayman & Lavier, 2014). The shear zones are areas that may have deformed via slow slip. All these studies present evidence for both brittle and ductile

deformation. For example, Fagereng et al. [2014] examined the Southern Marginal Zone (SMZ) of the Damara Belt, which formed by northward subduction at the time of Gondwana amalgamation (Barnes & Sawyer, 1980; Kasch, 1983). Highly sheared rocks within the formation formed under metamorphic conditions of 600°C and 10 kbar (Kasch, 1983). Lithologies within the formation include metabasalt interlayered with less rigid metapelites and metapsammites. The basalt lenses are tens to hundreds of meters long, on par with LFE slip diameters for the ductile matrix model, estimated below, of ~10 meters. Fagereng et al. [2014] believe that the sequence deformed via both shearing flow in metapelite and metapsammite rock and brittle deformation with and along the boundaries of the rigid, mafic lenses. This shear failure related to slip within and along the basaltic lenses could be the source of LFEs.

In the ductile matrix model, we make the assumption that within LFE sub-patches slip only occurs via LFEs. Within the matrix surrounding LFEs, slip only occurs ductilely. As we mentioned above, 2-10% of the patch slips via LFEs. In the connected patch model, the entire patch area slips via LFEs, but LFE slip only accounts for 2-10% of the total slip on the patch. The slip that does not produce LFEs likely occurs aseismically. Thomas et al. (2016) find that LFE slip speeds are 10^3-10^4 times faster than slow slip speeds and suggest that the background slip rate could control whether slip generates LFEs. Variations in slip speed could be a result of local variations in frictional properties, perhaps related to fluid pressure.

For both the ductile matrix and connected patch models we calculate the slip per LFE (S_N), slip area per LFE (A_N), and stress drop ($\Delta\sigma_N$) using our calculated values for A_P and A_T. The values for these parameters also depend on the number of sub-patches (N) within the LFE family patch, which we assume is 3-10 following Chestler and Creager (2017). For the ductile matrix model A_N and S_N are calculated with the following equations:

$$A_N = A_T/N$$
$$S_N = S_T\,(N/N_T). \quad [7]$$

For the connected patch model, A_N and S_N are:

$$A_N = A_P/N$$
$$S_N = S_T\,(N/N_T)\,(A_T/A_P). \quad [8]$$

Stress drop is calculated the same way for both models and is defined by the equation:

$$\Delta\sigma_N = \frac{7\pi\mu S_N}{16}\left(\frac{A_N}{\pi}\right)^{-1/2} \propto N^{1.5}. \quad [9]$$

Equations 7-9 assume that all LFEs slip the same amount over the same area. This is not a perfect assumption since we know that LFE moments have an exponential distribution and hence LFE slip or slip area likely also follow an exponential distribution (Chestler & Creager, 2017). Hence, estimates of area, slip, and stress drops calculated using equations 7-9 are only approximate characteristic values. Figure 3.7 shows the mean values for A_N, S_N, and $\Delta\sigma_N$ calculated using equations 7-9 for both models. The values for individual LFEs families are included in Table A2.3.

Because the values for A_N are larger and the values for S_N are smaller for the connected patch model, stress drops are lower for that model. A potential problem with the ductile matrix model is that the stress drops are high, in the range of "regular earthquakes" (e.g., Allmann & Shearer, 2009; Kanamori & Anderson, 1975). Multiple studies have asserted that LFEs have low stress drops on the order of 1 kPa (Bostock et al., 2015; Chestler & Creager, 2017; Thomas et al., 2016). Estimates from Bostock et al. (2015) and Thomas et al. (2016) assume that all LFEs within a family rupture the entire patch area (e.g. Figure 3.1a), which we do not prefer. Additionally, Fagereng et al. (2011) found evidence for events with low slip-to-length ratios

(implying low stress drops) in the Chrystalls Beach Complex in New Zealand, which they believe could be LFEs.

So far, we have considered 2D models for LFE slip. However, deformation does not have to be confined to a plane. Geologic studies are converging on a 3D model of subduction thrusts where the plate interface has a finite thickness (Rowe et al., 2013). Allowing for deformation to occur in a finite 3D volume, presumably via mixed mode shearing and ductile failure (Collettini et al., 2011; Compton et al., 2017; Fagereng, 2011; Fagereng et al., 2014; Fagereng & Sibson, 2010; Hayman & Lavier, 2014), allows for lower LFE stress drops for the ductile matrix model. For the 2D ductile matrix model, S_T has to be equal to S_{ETS} since we assume that slip only occurs via LFEs on the LFE sub-patches. In a finite 3D volume, S_T can be less than S_{ETS} on the LFE sub-patches since some of the observed geodetic slip could be accommodated via ductile deformation above or below the LFE sub-patch. Allowing S_T to be less than S_{ETS} in the ductile matrix allows for lower LFE stress drops than those shown for the ductile matrix model in Figure 3.7.

Alternatively, it is possible that LFEs can have static stress drops equivalent to the stress drops of "regular" earthquakes. Stress drop can be estimated from corner frequency, f_c, the rupture velocity, V_R, and seismic moment using the following equation (adapted from Shearer, 2009):

$$\Delta\sigma = \frac{7}{16}\left(\frac{f_c}{kV_R}\right)^3 \mathrm{M_o} \qquad [10]$$

where V_R is rupture velocity and k is a constant between 0.21-0.32. For regular earthquakes $V_R \approx 0.9\beta$ (Madariaga, 1976), where β is the shear wave speed. This relationship between rupture velocity and shear wave speed does not hold up for SSEs and LFEs where rupture speeds are much slower. Dividing the slip radius (~50 meters, Figure 3.7a) by the duration of LFEs, which

is ~0.5 seconds and is nearly independent of M_o (Bostock et al., 2015), yields rupture speeds of ~100 m/s. Equation 10 indicates that high LFE stress drops are possible, despite the low corner frequency of LFEs, because the LFE rupture velocity is slow.

4.2 Patchy distribution of LFE families

Figures 3.2 and 3.6 illustrate that there are spots on the place interface where slip does not occur in the form of observable LFEs. There are gaps between clusters of LFE families that are up to 10 km wide. Additionally, even within clusters of LFE families, there are identifiable gaps between families. The double difference results indicate that LFE families are distinct clusters of LFEs with gaps, up to 2-3 km, between families. A patchy distribution of LFE families is not only a feature of LFE catalogs beneath the Olympic Peninsula (Chestler & Creager, 2017;Peng & Rubin, 2016; Royer et al., 2015; Royer & Bostock, 2014), as discussed in section 3.3, it is a feature of LFE catalogs from Japan (Shelly et al., 2006), the San Andreas Fault (Shelly, 2010), and across the entire slow slip zone in Northern Cascadia (Royer & Bostock, 2014; Rubin & Armbruster, 2013).

One model to explain the patchy distribution of LFEs families is that LFE family clusters represent areas with higher strength than the surrounding regions. Stress builds on these patches, or asperities, while the surrounding areas experience aseismic slip. This model is similar to the model proposed by Ghosh et al. (2012) based on the observation that there are patches with higher and lower tremor location densities.

A heterogeneous slow slip zone is used in many slow slip models (Ando et al., 2010; Nakata et al., 2011; Daub et al., 2011; Skarbek et al., 2012). Modeled slow slip zones include a number of small, frictionally unstable patches within a stable background region. Patches are either prescribed high initial traction (Ando et al., 2010; Nakata et al., 2011) or are represented

by regions with velocity-weakening behavior based on rate-and-state frictional parameters (Skarbek et al., 2012). The background regions have either lower traction (Ando et al., 2010; Nakata et al., 2011) or display velocity-strengthening behavior (Skarbek et al., 2012). The patches in these models are clustered together rather than being uniformly distributed, similar to the geometry of our observed LFE family clusters. Results from these modeling studies indicate that a heterogeneous fault zone, with mixed brittle and ductile regions, can reproduce the slow rupture speeds of SSEs.

While inversions for ETS slip in Cascadia (e.g., Bartlow et al., 2011; Schmidt & Gao, 2010) show that there are spatial variations in the amount of slip, these inversions do not have the resolution to reveal slip variations on spatial scales less than 10-20 km, or the size of LFE family clusters. Therefore, we cannot directly compare the locations of high slip zones with the locations of LFE family clusters. Potentially smaller-scale variations in slip could be revealed by strainmeter data (Hawthorne et al., 2016).

While it is difficult to quantify spatial variations in slip during ETS events, there is evidence that slip/deformation does occur between LFE family clusters during ETS. LFE activity propagates updip through the gap beneath the TB and BH arrays (Figure 3.8) during both the 2010 and 2011 ETS events. Because LFE activity propagates through the spatial gaps, it is likely that slip occurs between LFE family clusters.

Another option to consider is that seismic slip occurs between LFE family clusters by some other mechanism than observable, repeating LFEs. Seismic energy could be released in the form of (1) LFEs that have such low SNRs that they cannot be detected, (2) non-repeating LFEs, or (3) events in a different frequency band than 2-8 Hz (e.g. very low-frequency earthquakes (VLFEs) (Ghosh et al., 2015; Ide, 2016)). If we invoke (1) to explain missing LFE families, the

LFE families within the spatial gaps of our catalog would have to be comprised of only tiny (M<~0.8) LFEs. Given that M_c decreases with downdip distance, it is possible that on the downdip edge of the slow slip zone there are families with only tiny LFEs. If M_c decreases consistently with depth, it is harder to imagine that there are families of small LFEs in the gap beneath the BH and TB array.

One piece of evidence that points towards option (2) is that there is tremor within the spatial gaps between LFE family clusters (e.g. Figure 3.8c). This tremor could either be poorly located or represent seismic energy release by non-repeating events. We will discuss option (3) in more detail in section 4.5.

4.3 Downdip variations in M_c and N_T

In this section, we will both consider downdip variations in M_c and N_T during ETS events and throughout the entire ETS cycle. To distinguish between time periods, we will refer to the characteristic moment, number of LFEs, and slip area during ETS events as M_c^{ets}, N_T^{ets}. We use M_c^{all} and N_T^{all} to refer to the characteristic moments and number of LFEs during all time periods (i.e., June 2009-September 2010 and August 2011).

We will first consider ETS events only. During ETS events, updip LFE families have larger characteristic (average) moments (M_c^{ets}) than downdip families. Larger average moments can be a result of more slip, larger slip areas, or a combination of both. While values for N_T^{ets} range from 200-600 LFEs, N_T^{ets} does not vary with downdip distance. Because N_T^{ets} is similar for updip and downdip LFE families and M_c^{ets} is larger for updip LFE families, more energy is released per updip LFE family than per downdip LFE family. Hence, during ETS events, it is likely that more moment is released within updip family patches than downdip family patches.

While N_T^{ets} remains relatively constant with downdip distance, N_T^{all} is much larger for downdip LFEs. As mentioned above, small LFEs with very low SNRs, could be missed. Hence the value givens here for N_T^{all} and N_T^{ets} are lower estimates. Despite that there are likely events missing from our catalog, missed events are more likely farther from the AofA. This means that underestimates in N_T^{all} and N_T^{ets} could be greater for the most updip (downdip distance <20 km) and downdip LFEs (downdip distance >45 km). On the downdip edge of the transition zone N_T^{all} is already higher, hence we believe that trend in N_T^{all} (N_T^{all} increases with downdip distance) is real.

Sweet (2014) made a similar observation, that the downdip LFE families contained many more LFEs than the updip families, using only four LFE families. Additionally, Sweet [2014] noted that while updip LFE families are predominantly active during ETS events, downdip LFEs are active throughout the entire ETS cycle. Wech and Creager (2011) observed that the largest tremor durations and recurrence intervals occur in the updip portion of the transition zone. Like M_c^{ets}, M_c^{all} decreases within downdip distance.

Considering the trends in M_c^{ets}, M_c^{all}, N_T^{ets}, and N_T^{all}, we conclude that in the updip region of the slow slip zone, LFE slip occurs through a smaller number of large LFEs and predominantly during ETS events. In the downdip region of the transition zone, LFE slip occurs through larger numbers of small LFEs, which occur throughout the ETS cycle. One interpretation of this observation is that the plate interface is stronger updip, and hence has a higher stress threshold (e.g., Sweet, 2014; Wech and Creager, 2011). Alternatively, perhaps if LFE sub-patches are mafic blocks, blocks could break up and become smaller with increasing depth. This could pose a length scale (limit on moment) that could result in decreasing M_c.

One limitation to this interpretation is that the most updip LFE families (downdip distances dip<20km) do not have the largest characteristic moments; their M_c's (both M_c^{ets} and M_c^{all}) are smaller than or approximately equal to those of LFE families with downdip distances between 30-40 km. The breakdown of the trends in M_c^{ets} and M_c^{all} for the most updip LFE families indicates that the updip portion of the transition zone is different. Perhaps more slip happens aseismically on updip edge of the transition zone. This idea is supported by the observation that during slow slip events, slip occurs updip of tremor (Hall & Houston, 2014; Peng & Gomberg, 2010; Wang et al., 2008; Wech et al., 2009). Another possibility is that some of the stress in the most updip region of the transition zone is relieved during mega-thrust earthquakes rather than slow slip events.

4.4 Model for LFE slip across the entire slow slip zone

So far in this paper we have discussed LFE slip on three difference scales, (1) within a single LFE family, (2) within clusters of LFE families, and (3) across the entire Olympic Peninsula, Washington. Within a single LFE family we find that only 2-10% of the area within the LFE family patch slips via LFEs. Following geological observations of exhumed subduction zones (e.g., Fagereng et al., 2014) we propose that regions within patches that do not slip via LFEs deform ductiley (i.e., our ductile matrix model). Beyond a single LFE family patch, LFE families tend to be clustered into groups 10-20 km in diameter (e.g. our east and west clusters). Within and between these LFE family clusters there are areas without observable LFEs.

We propose that LFE slip is heterogeneous on multiple spatial scales. This interpretation is also supported by both modeling (e.g., Ando et al., 2010; Nakata et al., 2011; Skarbek et al., 2012) and observational (Fagereng et al., 2014; Ghosh et al., 2012; Thomas et al., 2016) studies. Figure 3.9 is a cartoon of how we believe LFE slip occurs spatially. LFE families are clustered

into groups outlined by dotted lines. Areas without LFE families separate clusters of LFE families. Both LFE family clusters and LFE family patches (inset in Figure 3.9) also include areas without repeating LFEs. While evidence from Cascadia informed this model, it is applicable to other faults where a patchy distribution of LFE families has been observed, including Japan (Shelly et al., 2006) and the San Andreas Fault (Shelly, 2010). However, LFE moments have only been calculated in Cascadia (Bostock et al., 2015; Chestler & Creager, 2017; Sweet, 2014)

To investigate the amount of slip that occurs through LFEs on the plate interface, we calculate the summed moment release per square kilometer, assuming that each LFE occurs at either its LFE family location or the location of the LFE family centroid from the double difference relocation. We smooth the summed moment distribution using a Gaussian with a half width of 2 km to produce a map of moment density ($M_A(x, y)$ moment per unit area) and convert that to slip ($S_{LFE}(x, y)$) using the following relationship:

$$S_{LFE}(x, y) = \frac{M_A(x, y)}{\mu} \quad [11]$$

where μ=30 GPa is the shear modulus. Figure 3.10 is the resulting plot showing a map view of smoothed LFE slip for all time periods, ETS events, and inter-ETS time periods. We estimate the average slip that occurs within a dense patch of LFE families by dividing the integrated slip within an 18 by 21 km box surrounding the east cluster by the area of the box. The result is an average slip of 0.3 mm. The expected slip over a 16-month time period, assuming a plate rate of 40 mm per year, is approximately 53 mm. Therefore, LFE slip only accounts for approximately 0.6% of the total slip within the box (i.e., a dense region of LFE families). Additionally, we estimate the average amount of slip that occurs via LFEs throughout the entire region using the same method, but a 48 by 77 km box that contains all the LFE families. The result, 0.1 mm of

slip per unit area, implies that only about 0.2% of slip in the entire slow slip zone occurs via LFEs. This estimate is similar to the "seismic efficiency" of ETS events (0.1% or less), which Kao et al. (2010) estimated using tremor. Additionally, for an SSE that occurred in Mexico in 2006, Kostoglodov et al. (2010) estimated that the tremor moment release was more than three orders of magnitude smaller than the moment estimated with GPS data. Both Kao et al. (2010) and this paper estimate seismic moment. The main difference is that Kao et al. (2010) uses tremor amplitudes and we use LFE displacements. Both methods are limited by the ability to detect tremor/LFEs. Missed detections lead to an underestimate of total moment. Kostoglodov et al. (2010) estimates energy by integrating the velocity seismogram squared over time. Integration over time will miss less of the seismic signal than this work and Kao et al. (2010). Despite differences is methodology, it is encouraging that all three studies, including this work, find that moment release by tremor/LFEs represents a very small proportion of the moment released by slip.

We also estimate the percent of slip that occurs via VLFEs. Ide (2016) estimates the average moments from stacked waveforms filtered between 0.02 and 0.05 Hz (i.e. the very-low frequency (VLF) band). He does this for 112 reference points with a uniform spacing of 0.1° beneath southern Vancouver Island and the northern portion of the Olympic Peninsula (latitude≥47.9). He considers high-frequency tremors that occur between January 2005 and December 2014 within 10 km of each reference point and aligns low-frequency waveforms on the times of the peak tremor amplitudes before stacking. Using the average moment and number of events for each reference point, we calculate smoothed VLFE slip. Within the area where Ide's catalog and our catalog overlap (47.9<latitude<48.3 and -123.3<longitude<-122.9), VLFEs account for <1% of the geodetic slip. Similar to LFEs, the "slip efficiency" of VLFEs is low,

indicating that the majority of slip occurs without releasing seismic energy in the VLF (0.02-0.05 Hz) and LFE (2-8 Hz) frequency bands.

Figure 3.10 also illustrates the updip/downdip variation in LFE slip over time. During inter-ETS time there is little slip via LFEs in the updip region (longitude < -123.1). During ETS events, the patch with the most LFE slip (~0.8 mm) occurs in the updip region. This reaffirms our interpretation from section 4.3 that LFE slip occurs primarily updip during ETS events and downdip during inter-ETS time periods.

4.5 What are we missing?

One question we have not yet addressed in this work is what percent of the total seismic moment release are we detecting through repeating LFEs in our catalog. While we believe that we are seeing most of the LFE families beneath the arrays, it is possible that (1) there are low SNR LFEs that we are missing, and (2) there are other sources of seismic moment release. The latter is evidenced by the fact that Peng and Rubin (2016) detect tremors (short window detections) over a larger area than we detect LFE families.

To estimate the percent of seismic energy that we are detecting, we calculate synthetic seismograms for a one-hour time window (2010/8/16 18:00:00-19:00:00) during the 2010 ETS event that contains the most LFEs. Synthetic seismograms are the sum of time-shifted, scaled LFE templates. For LFE family *i*, station/channel *j*, and LFE *k*, the displacement seismogram is:

$$u^S{}_{ijk}(t) = u^T{}_{ij}(t) * \frac{d_{ijk}}{d^T{}_{ij}} \quad [12]$$

where $u^T{}_{ij}$ is the displacement seismogram for the template and $d_{ijk}/d^T{}_{ij}$ is a dimensionless scaling factor used to scale the amplitude of template *ij* to the amplitude of LFE *k*. d_{ijk} is the time integral of the displacement field for LFE *k* and $d^T{}_{ij}$ is the time integral of the displacement

field for template *ij*. The actual synthetic seismogram, ${u^S}_j(t)$, is the sum of the synthetic seismograms for every LFE that occurs within that hour. We convert ${u^S}_j(t)$ to a velocity seismogram, ${v^S}_j(t)$, by taking the time derivative.

We compare our synthetic seismograms to the actual velocity seismograms, $v_j(t)$, filtered between 2 and 8 Hz. Figure 3.11 shows example seismograms for the north and east channels from one station (BS04). Seismograms for other stations look similar. It is clear that LFEs (red) are not accounting for all of the energy in the real seismogram (blue). To quantify the amount of energy from the real seismogram that is not accounted for in the synthetic seismogram we try to match the real seismograms by adding noise to and amplifying the synthetic seismograms. We define the observed cumulative sum of energy for station/channel *j* as:

$$E_{o\,j}(\tau) = \int_0^t {v_j}^2(\tau)d\tau. \qquad [13]$$

Similarly, the predicted cumulative sum for station/channel *j* is defined as:

$$E_{p\,j}(\tau) = \int_0^t (({v_j^S}(\tau)m_j)^2 + n_j(\tau)^2)\,d\tau \qquad [14]$$

where m_j is the amplification factor for station/channel *j* and $n_j(\tau)$ is a vector of white Gaussian noise with standard deviation σ_j. For each station/channel pair we perform a grid search to find the values for m_j and n_j that minimize the misfit between $E_{o\,j}(\tau)$ and $E_{p\,j}(\tau)$. We solve for the amplification and noise values for the north and east channels for 3 stations per array, totaling 36 channels.

The median amplification factors m_j for arrays range from 1.2 to 2.1. The mean amplification factor for all arrays is 1.6. The median noise values for arrays range from 1-4×10^{-8} m/s (Figure 3.11). These values are on par with the median value for the average velocity

measured for hours without LFEs (i.e., background noise), which is ~1×10^{-8} m/s. Given the different locations of each array, we expect noise values to be different for each array. An amplification factor of 1.6 indicates that LFEs in our catalog account for approximately 60% of the recorded energy release that is not noise. We repeated the above analysis for a second hour and the amplification factors and noise levels were similar.

We also estimate the amount of LFE moment missing from our catalog based on our catalog's best-fit moment-frequency distribution (M_c=2.1×10^{11} N-m). To do this, we extrapolate the best-fit moment-frequency curve to M_o=0 N-m and compare the cumulative moment of LFEs represented by the extrapolated curve to the cumulative moment release of LFEs in our catalog. We find that our current catalog accounts for approximately 89% of the moment release. This is not particularly surprising since the number of small LFEs is limited in a catalog with an exponential distribution (as opposed to a power-law distribution). The discrepancy between our two calculated values for the percent of activity that we are seeing (i.e., 60% of the recorded moment release and 89% of moment released by known families) indicates that while we are seeing a large portion of moment release from known LFE families, the LFE families in our catalog only account for approximately 3/5 of the total seismic moment release. There could be other seismic energy sources such as non-repeating tremors or VLFEs.

5 Conclusions

One goal of this work was to further explore two of the end-member models for LFE slip within an LFE family patch proposed by Chestler and Creager (2017): the connected patch model (Figure 3.1b) and the ductile matrix model (Figure 3.1c). For the connected patch model, we assume that individual LFEs rupture connected sub-patches within the LFE family patch.

While the entire LFE family patch slips via LFEs during ETS events, the total amount of LFE slip on the patch (S_T) can be less than the geodetically observed slip (S_{ETS}). For the ductile matrix model, where LFEs rupture small sub-patches (black dots in Figure 3.1c) surrounded by ductilely deforming regions, we assume that within sub-patches $S_T=S_{ETS}$.

We calculate the LFE family patch area (A_P) and the area within the LFE family patch that slips through LFEs (A_T) for LFE families during ETS events. For the ductile matrix model, we estimate A_T by the summed seismic moment release of LFEs and the geodetically determined amount of slip during ETS and find that for every LFE family $A_T=0.02\text{-}0.1A_P$. Therefore, in the ductile matrix model, 2-10% of the LFE family patch area slips via LFEs. For the connected patch model, we estimate S_T by the summed seismic moment and the known slip area $A_T=A_P$ and find that for every family $S_T=0.02\text{-}0.1S_{ETS}$. This indicates that, for the connected patch model, LFE slip only represents 2-10% of the slip that occurs on the LFE family patch.

The ductile matrix model is physically appealing. LFEs could occur via brittle deformation with and along the boundaries of the rigid, mafic lenses observed by Fagereng et al. (2014) (i.e., the mafic lenses could represent LFE sub-patches). The problem with the ductile matrix model is that estimated LFE stress drops are on the order of 10^2-10^3 kPa, which are larger than observed SSE stress drops, and on par with the stress drops for "regular" earthquakes. This does not match the observation from Thomas et al. [2016] that LFEs are low stress drop events. LFE stress drops are much lower in the connected patch model (~1-10 kPa). Admittedly, both models are end-member models and the truth is likely a mix of the two models.

We show that on many spatial scales, within an LFE family patch (~1 km), within clusters of LFEs families (4-15 km), and between clusters of LFE families, there are areas that slip without radiating seismic energy in the form of observable, repeating LFEs. The idea of a

heterogeneous slow slip zone with both brittley and ductiley deforming regions is supported by models of slow slip (e.g., Ando et al., 2010; Nakata et al., 2011; Skarbek et al., 2012) and observational studies (Fagereng et al., 2014; Ghosh et al., 2012; Thomas et al., 2016). Regions without LFEs either slip aseismically/ductiley, as assumed by models, or slip while releasing seismic energy via non-repeating LFEs or events in a different frequency band than LFEs. Our model for heterogeneous LFE slip is illustrated in Figure 3.9. Overall, LFE slip only accounts for approximately 0.2% of the slip that occurs within the slow slip zone.

Additionally, we observe trends in M_c^{ets}, N_T^{ets}, M_c^{all}, and N_T^{all} with downdip distance. While M_c^{ets} decreases with downdip distance, N_T^{ets} does not change. This indicates that more energy is released through updip LFEs than downdip LFEs during ETS events. Alternatively, while, both M_c^{ets} and M_c^{all} decrease with downdip distance, unlike N_T^{ets}, N_T^{all} increases with downdip distance. We interpret this to mean that during the entire ETS cycle, downdip LFE slip occurs through a larger number (800-1200) of small LFEs, while updip LFE slip occurs through a smaller number (200-600) of larger LFEs and primarily during ETS events. This supports the idea proposed by both Sweet (2014) and Wech and Creager (2011), that the plate interface is stronger updip and hence has a higher stress threshold. We also note that the trends in M_c^{ets} and M_c^{all} break down for the most updip LFE families (dip distance<20km). This indicates that the most updip portion of the slow slip zone is different and perhaps releases energy less seismically that the downdip regions of the slow slip zone.

.

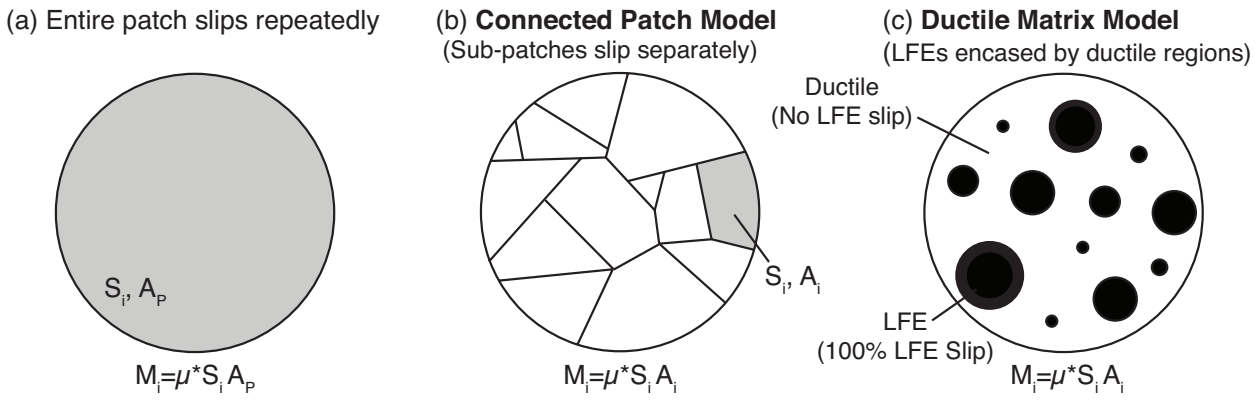

Figure 3.1: Models for LFE slip. (a) Each LFE ruptures the entire LFE family patch. The ith LFE has slip, Si, moment, Mi, and area, Ai=AP, where AP is the area of the LFE family patch. In this model, since slip area remains constant, LFE slip, Si, must follow an exponential distribution. (b) Each LFE ruptures a sub-patch within the LFE family patch and all the patches are connected. The sum of all LFEs during an ETS produces the same accumulate slip everywhere within the family patch. (c) Each LFE ruptures a sup-patch within the LFE family patch, but sub-patches are surrounded by a ductilely-deforming matrix.

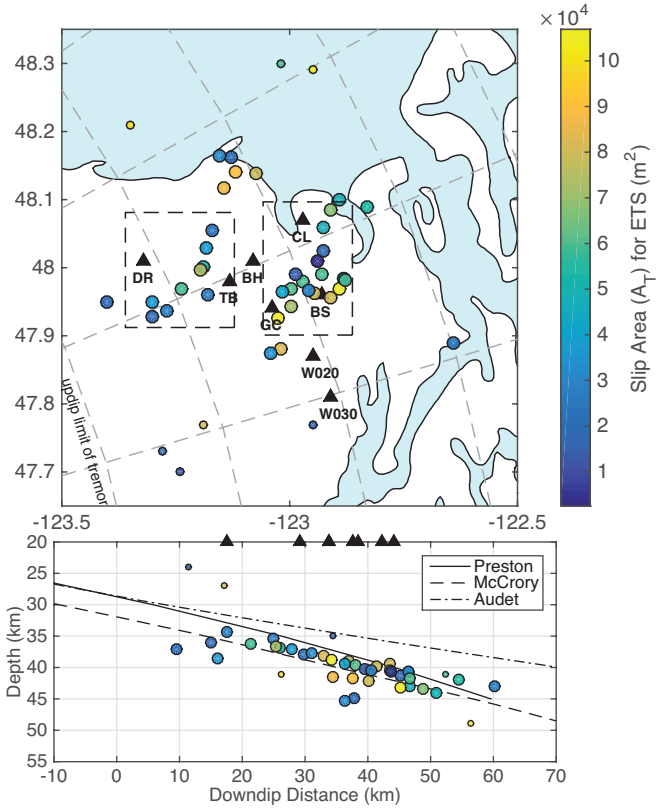

Figure 3.2: Map (top) and cross section (bottom) of LFE families beneath the Olympic Peninsula, WA, color-coded by ETS slip area (AT). LFE families located far from the AofA, whose locations are more uncertain, are shown as smaller dots. Boxed groups of LFE families are those for which we calculate patch size. The curved dashed lines represent the distance from the updip limit of tremor at 20 km increments.

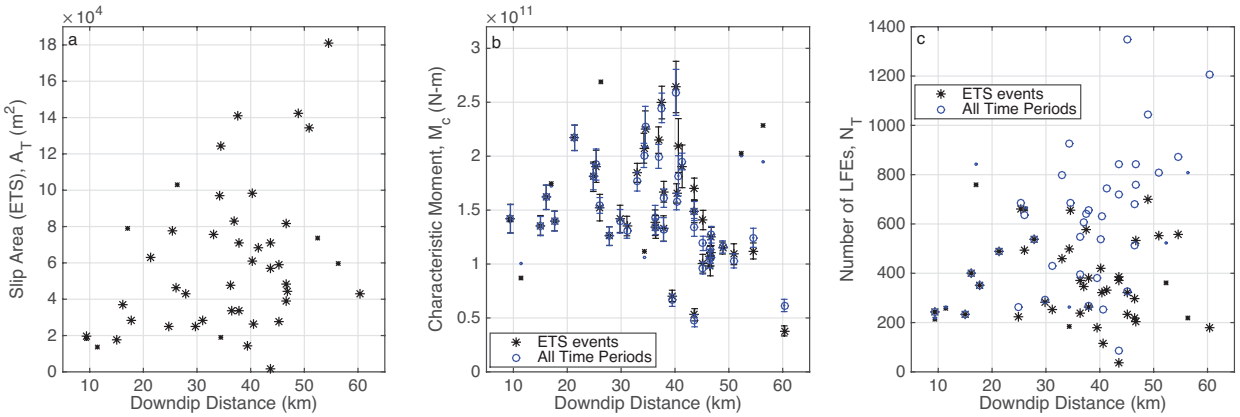

Figure 3.3: Plots showing (a) slip area and (b) characteristic moment of LFE families as well as (c) the number of LFEs in families verses downdip distance. Plot (a) only shows the slip area during ETS events because we do not have good estimates of inter-ETS slip, and hence cannot calculate inter-ETS slip area. Plots (b) and (c) show data from both the entire catalog (inter-ETS time periods included) and just ETS events. Values included in this figure are included in Table A2.1. In all three subplots, small dots and stars represent families located north and south of the AofA respectively.

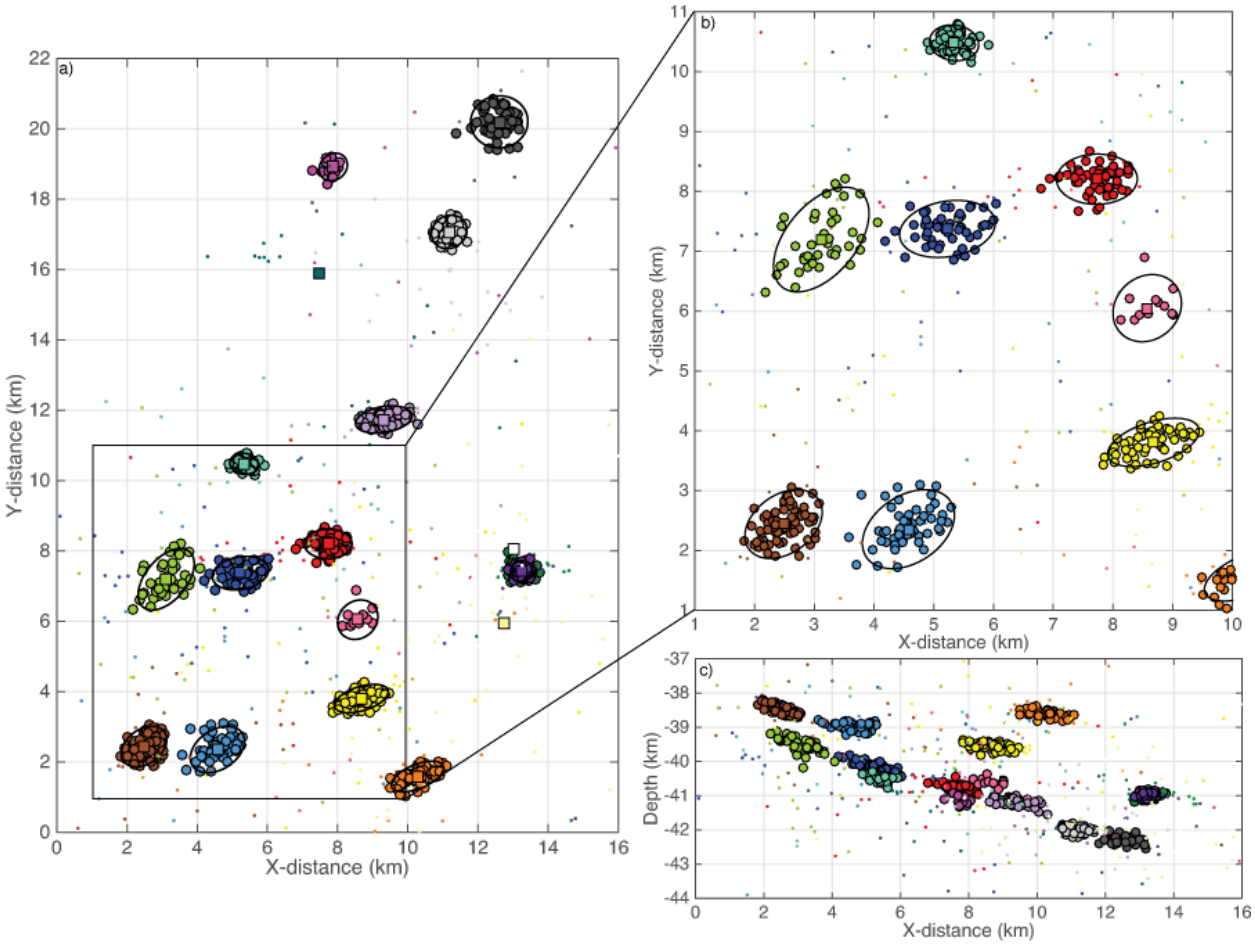

Figure 3.4: Relocation results from the east cluster. (a) Results for all families in map view. Squares represent that family centroids, large dots indicate LFEs that were used to calculate AP, and small dots indicate LFEs that were tossed. The black ellipses are the confidence ellipses used to calculate Ap. (b) Zoomed in version of (a) showing close-up relocations for some families. (c) Results in cross section. The reference location, (0,0) km, is equivalent to 47.9° latitude and -123.06° longitude.

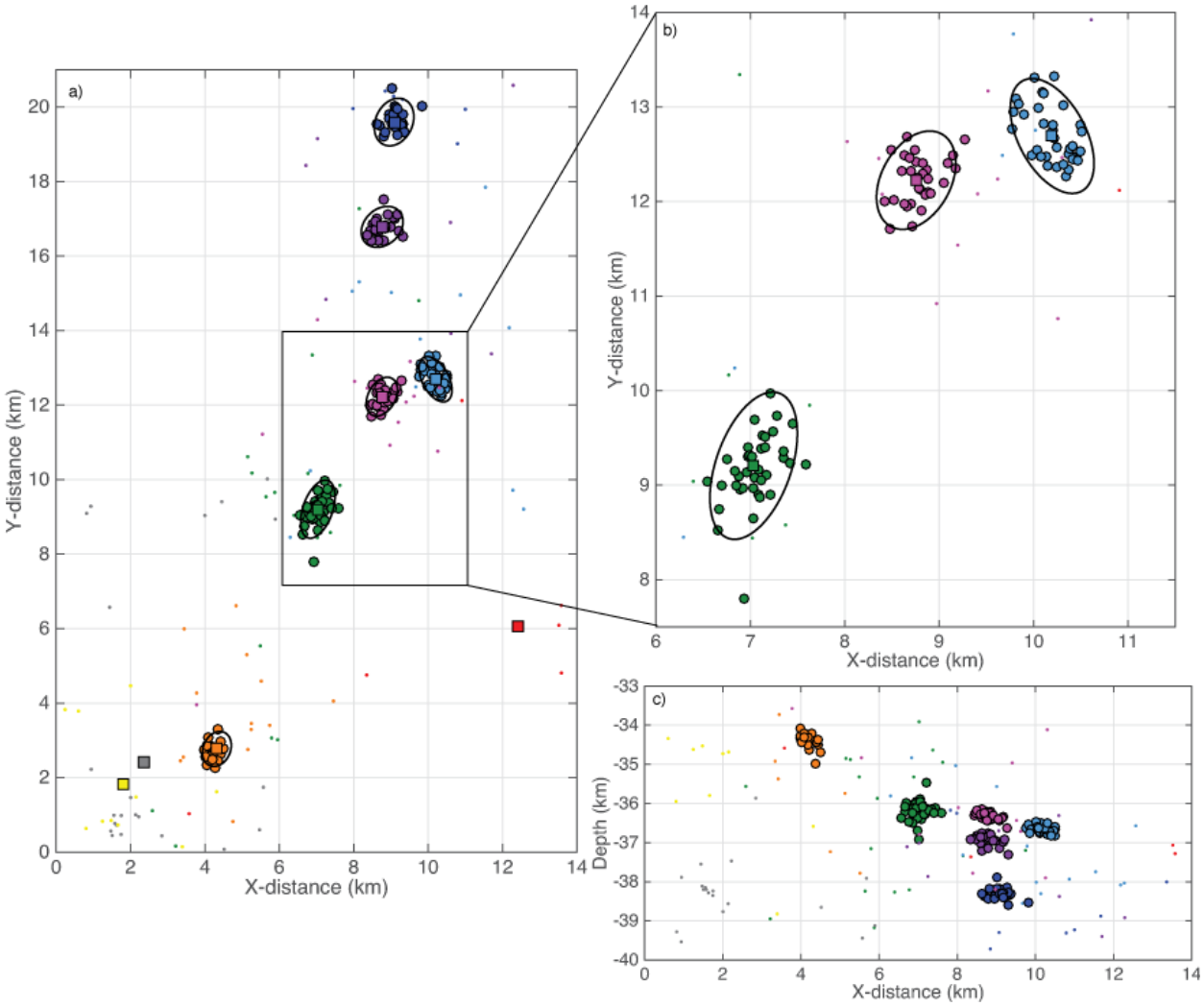

Figure 3.5: Relocation results from the west cluster. (a) Results for all families in map view. Squares, large dots, small dots, and black ellipses are the same as in Figure 4. (b) Zoomed in version of (a) showing close-up relocations for some families. (c) Results in cross section. The reference location, (0,0) km, is equivalent to 47.89° latitude and -123.32° longitude.

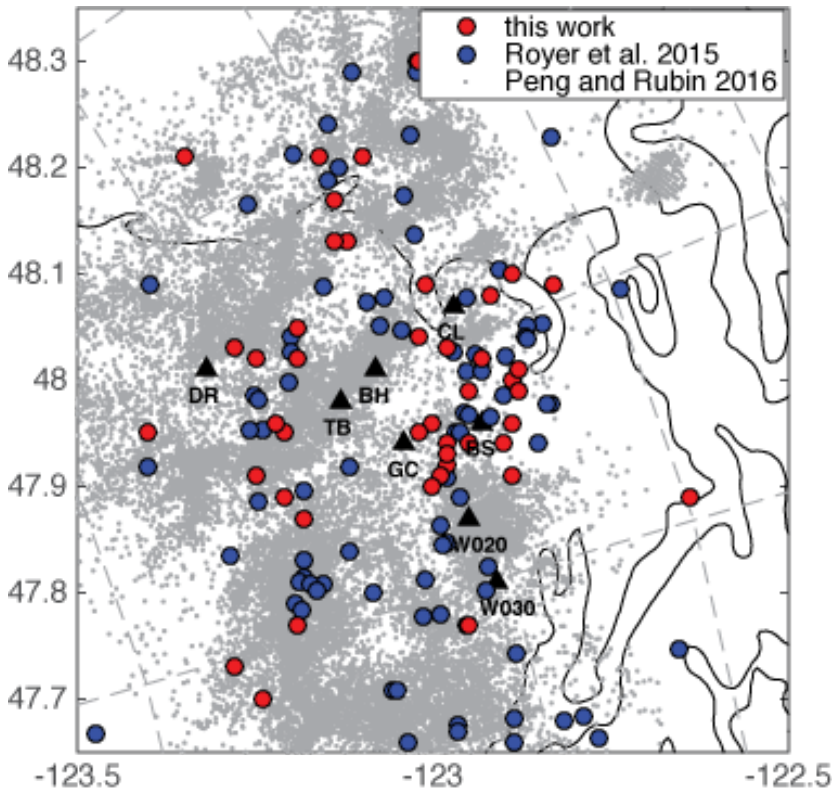

Figure 3.6: Comparison between catalogs from this work (red dots), Royer et al. [2015] (blue dots), and Peng and Rubin [2016] (small, grey dots). Locations from Peng and Rubin [2016] are their 6-second window detections found using the TB, BH, and GC arrays. Locations shown from this work and Royer et al. [2015] are pre-double difference locations.

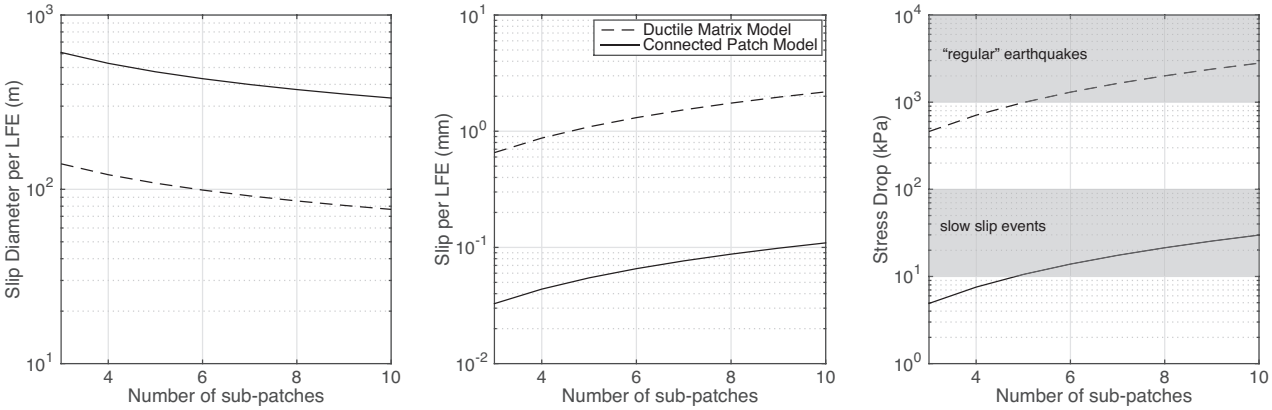

Figure 3.7: Mean (a) slip diameters, (b) slips, and (c) stress drops of LFEs for the ductile matrix (dashed lines) and connected patch (solid lines) models.

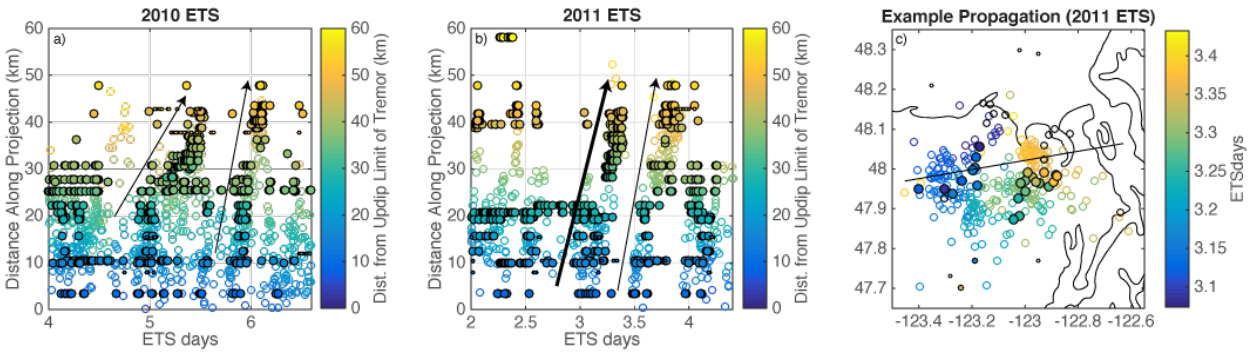

Figure 3.8: Examples of propagations that move between LFE family clusters from the (a) 2010 and (b) 2011 events. (c) Map showing example propagation (bold arrow in (b)) in map view. The black like is the projection used to make plots (a) and (b). The filled dots are LFEs and the open dots are tremors. Small, closed dots represent LFEs within families located north and south of the AofA. Tremor locations are from Ghosh et al. (2012). In (c) black, open circles are LFE families that were not active during the propagation.

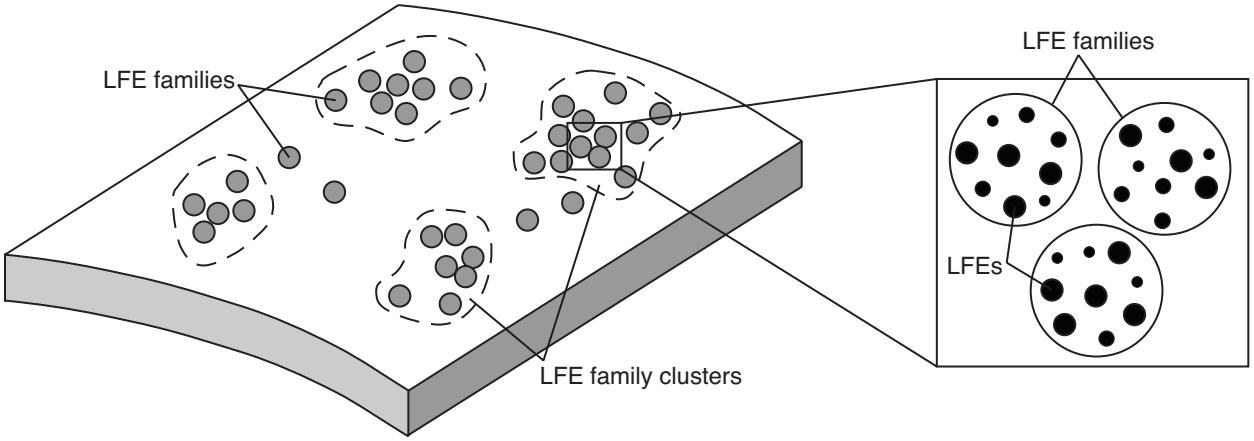

Figure 3.9: Model of LFE slip on the plate interface. LFE families group together in clusters surrounded by regions where slip does not occur through observable, repeating LFEs. Within clusters, there are gaps between families, also where LFEs are not observed. Finally, within an LFE family patch only 2-10% of the area slips via LFEs. The rest likely deforms ductiley. Grey shading=partial LFE slip. Black shading=100% LFE slip.

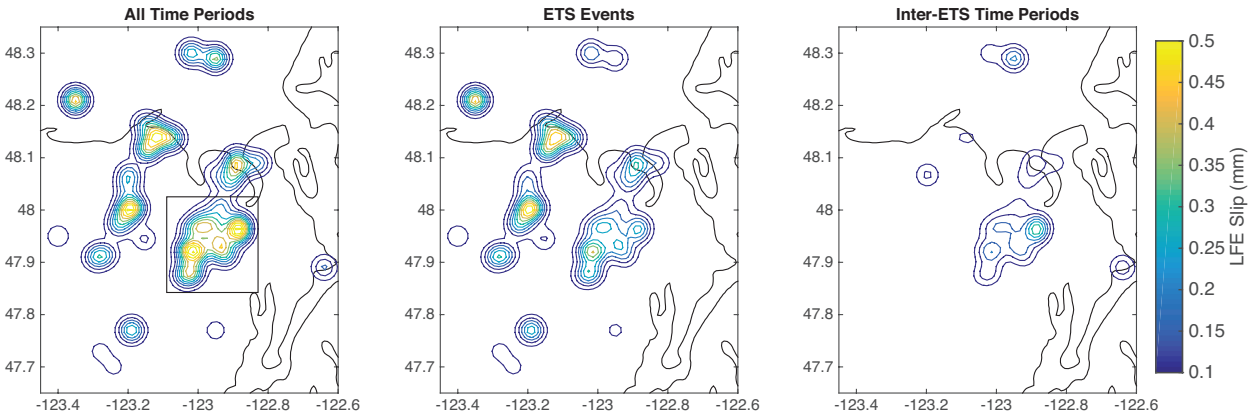

Figure 3.10: Smoothed LFE slip for (a) all time periods, (b) ETS-events, and (c) inter-ETS time periods. The box in (a) shows the region we used to calculate the percent of slip that occurs via LFEs within a dense patch of LFE families.

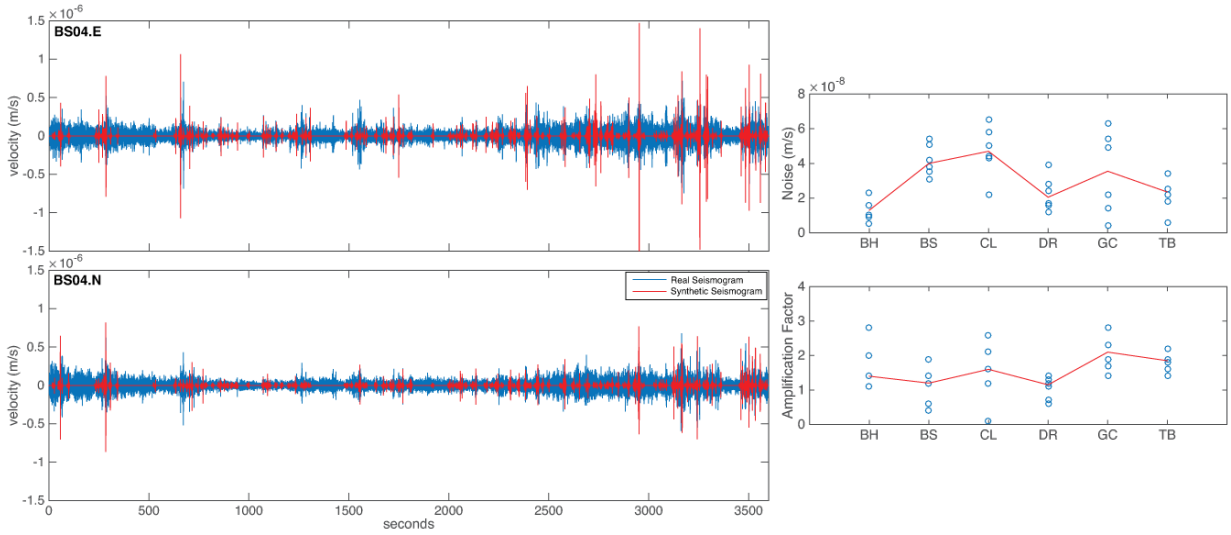

Figure 3.11: (left) Real (blue) and synthetic (red) seismograms for the E and N channels of station BS04. (right) Noise values and amplification factors for 3 stations (E and N channels) for each of the six arrays, resulting in 36 station/channel pairs. The red lines show the median noise values and amplification factors for each array.

Using low-frequency earthquakes as indicators of the depth, geometry, and thickness of the plate interface beneath the Olympic Peninsula, WA

The content of this chapter will be submitted for publication in *Geochemistry, Geophysics, Geosystems*.

1 Introduction

The Cascadia Subduction Zone (CSZ) is a convergent plate boundary where the oceanic Juan de Fuca (JdF) Plate underthrusts the continental North American plate at a rate of ~4 cm/yr. The convergence of these two plates produces both M8-9 megathrust earthquakes (e.g., Atwater, 1987, 1992) and slow slip events (Dragert et al., 2001; Rogers & Dragert, 2003). Knowing the geometry of the CSZ plate interface, including its depth, thickness and how it is situated relative to other features at depth (e.g., earthquakes and the observed low-velocity zone), is important for understanding subduction-related processes. These include earthquake hazards, the transport and release of fluids by subducted minerals, and the mechanics of slow slip. In addition, knowing the depth of the plate interface could shed light on the nature of the widely-observed low-velocity zone (LVZ) (Abers et al., 2009; Audet et al., 2010; Hansen et al., 2012; Nicholson et al., 2005; Rondenay et al., 2001).

In Cascadia, the 3 to 4 km thick LVZ is characterized by low S-wave velocities (2 to 3 km/s), high V_p/V_s ratios (~2.2-2.7), and high reflectivity (Audet et al., 2009; Hansen et al., 2012; Nowack & Bostock, 2013). The LVZ in Cascadia has been identified and mapped beneath Vancouver Island, Canada (e.g., Hansen et al., 2012; Nicholson et al., 2005), Washington (e.g., Abers et al., 2009), and central Oregon (e.g., Rondenay et al., 2001). A study by Audet et al. (2010) provided evidence for the continuity of the LVZ across the entire Cascadia margin to

depths of ~45 km. Several interpretations for the nature of the LVZ have been proposed. A popular model for the LVZ is that it represents the upper oceanic crust, which is comprised of hydrated pillow basalts, sheeted dikes, and sediments (Bostock, 2013; Hansen et al., 2012; Nowack & Bostock, 2013). Other interpretations for the LVZ's nature include that the LVZ represents the entire oceanic crust (Nicholson et al., 2005), underplated sediments (Calvert & Clowes, 1990), or a fluid-rich layer within the overlying plate (Hyndman, 1988). Low-velocity zones with high V_p/V_s have also been observed in Japan (Shelly et al., 2006) and Mexico (Song et al., 2009).

In most subduction zones, background earthquakes are abundant and can be used to illuminate plate interface geometry. The CSZ is different; it lacks widespread earthquakes in both the North American forearc region and the subducting JdF oceanic plate. Wadati-Benioff Zone (WBZ) seismicity primarily occurs in three regions: (1) at shallow (<40 km) depths beneath Vancouver Island, (2) beneath Northwestern California, and (3) at intermediate depths (30-50 km) beneath the Puget Sound regions (McCrory et al., 2012). Because WBZ earthquakes occur over a limited spatial range in Cascadia, their utility for mapping out plate interface geometry is limited.

Multiple methodologies have been employed to map the CSZ plate interface. Preston et al. (2003) simultaneously inverted 90,000 P-wave travel times for earthquake locations, three-dimensional (3D) structure, and reflector (oceanic Moho) geometry. The top of the slab is inferred to be 7 km above the oceanic Moho. Audet et al. (2010) used receiver functions to map the LVZ from northern California to northern Vancouver Island. They map the LVZ as the top of the plate interface. McCrory et al. (2012) performs a 3D inversion for plate geometry using mainly on-slab earthquake locations and previously-determined regional velocity structures.

The location of the plate interface differs somewhat between the above-mentioned studies, likely due to their different methodologies and/or definition of the plate interface. The McCrory et al. (2012) plate interface is located ~5 to 10 km deeper than the plate interface from Audet et al. (2010) and the Preston et al. (2003) slab top lies in between the plate interfaces from other two models. A 5 to 10 km difference in plate interface depth is significant and it could have implications for the nature of the LVZ. We are, therefore, motivated to further investigate plate interface structure beneath the Olympic Peninsula using locations of low-frequency earthquakes (LFEs).

Slow slip events (SSEs) have been observed along the entire CSZ with recurrence intervals ranging from 10 to 19 months, depending on their along-margin location (Brudzinski & Allen, 2007; Szeliga et al., 2008). Observations of SSEs come from both GPS measurements (Bartlow et al., 2011; Rogers & Dragert, 2003; Schmidt & Gao, 2010) and tremor catalogs (e.g., Ghosh et al., 2012; Wech & Creager, 2008). The seismic signature of tremor is emergent rather than impulsive, making it difficult to locate accurately, especially in depth. LFEs on the other hand, which comprise tremor (Shelly et al., 2007), have distinct P- and S-wave arrivals. They can, therefore, be located more-accurately than tremor. LFEs in Japan and Cascadia locate near the plate interface (Bostock et al., 2012; Shelly et al., 2006) and have thrust focal mechanisms (Ide et al., 2007; Royer & Bostock, 2014). It is generally accepted that LFEs are produced by shear slip on the plate interface. Hence, they have the potential to be robust indicators of the depth and shape of the plate interface and the thickness of plate interface deformation.

In this work, we use high-precision, relative LFE locations beneath the Olympic Peninsula, WA to examine the CSZ plate interface structure within our study region. We compare LFE locations to existing plate models and note that the actual plate interface appears

more complex. Using a similar methodology to the method that Chestler and Creager (in review) used to calculate the seismogenic areas of LFE families, we calculate the spread of LFE locations in depth. This provides an indicator of the width of the zone where deformation via LFEs occurs. We propose that this observation, paired with geological studies of slow slip, can help illuminate the deformation mechanism responsible for slow slip at depth.

2 Methods

We use the high-precision, relative LFE locations calculated by Chestler and Creager (in review). Using data from the Array of Arrays (AofA) experiment (Ghosh et al., 2012), Chestler and Creager (in review) inverted for the relative LFE locations of 1586 LFEs in 25 LFE families using the double-difference relocation method (hypoDD, Waldhauser, 2001). The families occur in two clusters, or areas where many LFEs families are located close together, which Chestler and Creager (in review) define as the east and west clusters. In this work, we only examine events within the east cluster of LFE families (1263 events within 18 families) (Figure 4.1). The east cluster of families is located in the middle of AofA station coverage where we expect both absolute and relative locations to be the most robust. We compare relative locations to the Preston et al. (2003), Audet et al. (2010), and McCrory et al. (2012) plate interface models, as well as the 3-D P-wave velocity structure and earthquake locations from Preston et al. (2003).

To perform their relocation, Chestler and Creager (in review) inverted high-precision differential P- and S-wave travel times between common stations and event pairs for relative LFE locations. Differential travel times were calculated by cross-correlating LFE waveforms on 6 AofA arrays (10 to 20 stations per array) and 3 individual stations from the Cascadia Arrays for Earthscope (CAFE) Experiment. Cross-correlating P- and S-waveforms on vertical and horizontal channels respectively give precise lag times between phase arrivals for event pairs.

For more accurate lag time picks they stack the correlation functions from individual stations at each array. The result is two S-wave picks (on the east and north channels) and one P-wave pick (on the vertical channel) per array.

The double-difference technique minimizes the residuals between observed and predicted travel time differences for pairs of nearby events observed at a common station. The hypoDD algorithm minimizes the residuals by weighted least squares using either singular value decomposition (SVD) (for small systems) or the conjugate gradients method (LSQR, Paige & Saunders, 1982) (for large systems). The parameters that Chester and Creager (in review) used to perform the hypoDD inversion are summarized in their supplementary materials. They chose parameters to optimize the LSQR least squares inversion and include a maximum separation distance for event interaction (4 km) that ensures that LFEs only interact with other LFEs with similar waveforms. As a result, events without neighboring LFEs within 4 km were automatically removed.

Chestler and Creager (in review) performed two different relocations: (1) where each LFE starts at its LFE family location, and (2) where LFEs are randomly assigned to starting locations within a 6.5 by 6.5 km grid centered around the original LFE family location. For both relocations (using both types of initial LFE locations) they iterate the hypoDD inversion five times. Each time updated locations and origin times are used from the previous iteration to recalculate differential travel-time picks. To avoid errors due to cycle skipping, they limit the allowed lag times, calculated by cross correlation, to +/- 0.3 s or 0.4 s during the first 4 iterations. This allows poorly located LFEs to stabilize. For the last iteration, they decrease the cutoff value to 0.2 s to better eliminate cycle skipping errors. Both relocation methods (i.e., assuming different starting locations for LFEs) yielded similar results. Here we discuss results from

relocation method 2, where LFEs are randomly assigned to starting locations. This is the same catalog used in Chestler and Creager (in review).

After five iterations, 1222 (97%) of the original 1263 LFEs remained. Chestler and Creager (in review) define the 3-D footprint of an LFE family by the volume of the 3-D confidence ellipsoid that contains 60 to 80% of the events within the family, depending on the quality of locations for that family. The remaining 20 to 40% of the events in each family are scattered broadly and are likely mislocated (see below). To find this confidence ellipsoid, for each family they convert the LFE longitude, latitude, and depth to Cartesian coordinates, remove the mean locations (centroids) and calculate the 3-D covariance matrix **C** (second moment about the centroid). If the LFE locations within the family have a Normal distribution then 95% of the locations would lie within the 95% confidence ellipsoid defined by:

$$\boldsymbol{X}^T\boldsymbol{C}^{-1}\boldsymbol{X} < \Delta^2 \qquad [1]$$

where $\Delta 2 = 7.81$ is the 95th percentile of the chi-squared distribution with three degrees of freedom and **X** is a location vector relative to the centroid. Chestler and Creager (in review) remove the LFEs that lie outside this ellipsoid and recalculate the centroid and error ellipse of the reduced data set and repeat three times until the centroid is stable. Using the stabilized centroids, they recalculate the 3-D covariance matrix. Finally, for each family, they determine the value of $\Delta 2$ corresponding to the confidence ellipsoid that includes 60-80% of all the events. This ellipsoid defines the LFE family footprint.

Tossing 20-40% of events is reasonable due to the low signal-to-noise levels of LFE waveforms in Cascadia. The LFEs that locate outside of the main family clusters are scattered broadly and their locations are poorly constrained. For further justification, see section 3.2 and Figure A2.4 of Chestler and Creager (in review).

We use this same definition for the 3-D footprint of an LFE family to investigate the spread of LFE depth locations for each family. Using the 60-80% of the retained events from each LFE family, we calculate the mean LFE depth. Assuming that the distribution of LFE depth locations is Normal, two thirds of the events in each family should lie within one standard deviation, σ_z, of the family's mean depth. We define the thickness of each family in the depth direction as $2\sigma_z$.

3 Results

3.1 Variance in LFE depths

LFE family footprints are ellipsoidal in shape. For each family, the largest eigenvalue of the 3-D covariance matrix that defines the family's 3-D footprint corresponds to the eigenvector in the downdip direction. The smallest eigenvalue corresponds to the eigenvector in the depth direction. We find that LFE family footprints are thin in the depth direction and elongate in the downdip direction (Figure 4.2). LFE families do not overlap at different depths.

We calculate the standard deviations in the depth direction (σ_z) and find that σ_z ranges from 65-170 meters. Thus, we infer approximate thicknesses of LFE families, $2\sigma_z$, of 130 to 340 meters. This is an upper bound estimate since a portion of the spread in LFE depths is due to location error.

We estimate the errors in LFE depths the same way that Chestler and Creager (in review) estimate horizontal LFE location errors. We relocate LFEs from one family (cyan-colored family in Figures 4.1 and 4.2) using the SVD inversion method, which gives much better error estimates than the LSQR inversion method. The mean depth error for LFEs within the cyan family is 30 meters. This indicates that σ_z could be up to 50% smaller than we estimated above, implying smaller LFE family thicknesses.

3.2 Comparison to plate interface models and 3-D structure

We examine LFE depths projected on three downdip cross sections and three along-strike cross sections (Figure 4.2). Each downdip cross section has a different along-strike distance measured from the southernmost limit of the CSZ in Northern California. Profiles A, B, and C have along-strike distances of 801, 795, and 790 km respectively. In both Figures 4.2 and 4.3, LFEs are only plotted on the profiles that they are nearest to. LFEs plotted on cross section A are 0.5-2 km shallower than the LFEs with similar downdip distances plotted on cross sections B and C.

The variation in LFE depths along strike is apparent on the along-strike cross sections (D, E, and F) in Figure 4.2. For example, on cross section E the northernmost LFE family (greatest along-strike distance) is approximately 2 km deeper than the southernmost LFE family. Similarly, in cross sections D and F, the northern LFEs are deeper than the southern LFEs. In all three cross sections the locations of LFE families dip ~10 to 25° to the north. These results imply a plate interface with substantial geometrical deviation from a smooth plane over distances of about 5 km.

LFE hypocenters lie in between 38 and 43 km in depth. In all three cross sections, LFEs are located on or near the McCrory et al. (2012) plate interface model and consistently 5 to 8 km deeper than the Audet et al. (2010) plate interface. The estimated relative LFE depth errors are approximately two orders of magnitude smaller than the difference in depth between the McCrory et al. (2012) and Audet et al. (2010) plate models. Therefore, even considering potential relative depth errors, families locate closer to the McCrory et al. (2012) plate model. The absolute depths errors are much larger than the relative errors and are harder to estimate. Chestler and Creager (2017). originally locate LFE families by performing a grid search for the

locations that minimize the residuals between the observed and predicted P- and S- wave differential travel times and S minus P times. They use the 3-D P-wave velocity model from Preston et al. (2003), converting to S-wave velocity assuming the Earth is a Poisson solid, to predict travel times. After the double-difference relocation, LFE depths remained near the absolute depths of their LFE families and family centroids collapse onto a closer approximation of a plane, locally.

Figures 4.3a, 4.3c, and 4.3e display the P-wave velocity structure from Preston et al. (2003). While velocity generally increases with depth, all three cross sections contain a zone with a ~7% decrease in velocity that sits beneath the Preston et al. (2003) and McCrory (2012) plate interfaces. This low-velocity zone is approximately 5 to 7 km thick, though resolutions tests (Preston et al., 2003) suggest that a thin layer would appear wider than it is. Our LFE families locate on top of the low-velocity zone. Additionally, our LFE families lie ~5 km above the "regular" earthquakes, located by Preston et al. (2003), that occur in the subducting oceanic plate.

4 Discussion

4.1 Plate interface geometry

In our study region, LFE hypocenters fall between 38 and 43 km depth and correspond most closely with the McCrory et al. (2012) plate model. Royer and Bostock (2014) also created a catalog of LFE families in Northern Cascadia, spanning from Vancouver Island, Canada to the southern portion of the Olympic Peninsula, WA. They relocate their LFE families using the hypoDD algorithm. They find that the McCrory et al. (2012) and Audet et al. (2010) plate models bracket the LFE families below southern Vancouver Island and northern Washington.

More specifically, the LFE families beneath southern Vancouver Island are slightly shallower (29 to 40 km) than the LFE families beneath northern Washington (32 to 49 km). They note that the LFE families in Washington, where our LFEs are also located, correspond more closely with the McCrory et al. (2012) model and that the Vancouver Island families correspond more closely with the Audet et al. (2010) model.

The above observations, from both this work and Royer and Bostock (2014), indicate that the plate interface depth varies along strike. Even in our small, 20 by 20 km study area the southernmost LFEs (profile A) are 0.5 to 2 km shallower than other, more-northern LFEs (profiles B and C) located at similar downdip distances. The along-strike profiles (Figure 4.2d, 4.2e, and 4.2f) clearly illustrate the along-strike variation in LFE depths with constant downdip distance. In all three profiles, LFE depths dip ~10-15° to the north. Plate interface models often depict a flat, smooth plate interface (e.g., the McCrory et al. (2012) and Audet et al. (2010) models in Figure 4.2). To the contrary, our results indicate that the plate interface deviates from a smooth surface on scales of 5 km or less. Like our LFEs, the Preston et al. (2003) plate interface model dips to the northeast in our study region. Without good locations for LFEs over a larger area, it is difficult to rectify the differences in the along-strike plate interface depth indicated by our LFEs versus Preston et al. (2003). Mapping LFE depths over a larger area is necessary to better determine the shape of the plate interface and characterize its deviation from smooth models. For example, is the plate interface indeed generally deeper along strike to the north? Or does plate interface depth fluctuate throughout the CSZ margin over length-scales of only a few km?

4.2 Fault zone thickness and its implications for slow slip deformation

The width over which deformation occurs within a fault zone determines the strain rate in the fault rock, which in turn can control mechanisms involved in the rupture process (Sibson, 2003 and references therein). Geologic, laboratory, seismic, and modeling studies have been key for characterizing deformation in fault zones that host "regular" earthquakes, including the width over which deformation occurs. Studies of exposed faults serve as an effective way to visualize and understand deformation processes, yet outcrop scale and fault exposure can restrict these studies. Laboratory studies allow the direct observation of deformation in conditions where material properties, temperature, pressure, and other variables are well known. Comparing microstructures developed during laboratory experiments to field observations allows researchers to connect deformation processes to the resulting signature in the rock record. Seismic studies can reveal the size and distribution of earthquakes and strain and slip rates on actively deforming faults. And finally, modeling can help elucidate the physics governing slip processes.

Our understanding of slow slip deformation is just emerging. Hence, constraining slow slip from multiple perspectives (i.e., geologic, laboratory, seismic, and modeling) will serve to broaden our knowledge of how slow slip occurs. In the rest of this section we summarize how each of these types of studies have contributed to our understanding of fast slip, emerging research on slow slip deformation in each of these areas, and how our results further the understanding of how slow slip occurs.

Pseudotachylyte (glassy or fined-grained rock formed during frictional melting) has been the primary geological indicator of "regular" earthquake slip (i.e., fast slip at speeds of 0.1 to 1 m/s) in the rock record (Cowan, 1999). However, more recent studies have identified other indicators of frictional heating (e.g., devolatilized hydrous and carbonate minerals) and features formed under extreme transient stress conditions (e.g., injection veins and wing cracks) that are

unique to seismic ruptures (Rowe & Griffith, 2015). These indicators have been critical for identifying faults where fast displacement has occurred.

Fault zones that host "regular" earthquakes are comprised of a highly deformed core surrounded by a damage zone composed of rocks with higher fracture density than the surrounding host rock. While fault damage zone thicknesses range from less than 1-10^3 meters thick (Savage & Brodsky, 2011), fault cores, where finite displacement is accommodated, have thickness of a few centimeters to a few decimeters (e.g., Shipton et al., 2006; Sibson, 2003).

Rowe et al. (2013) studied the thicknesses of subduction thrusts specifically by compiling measurements from ocean drilling projects (<1 km depth) and geological studies of exposed thrust faults (1 to 15 km depth). Their results show that between the depths of 0 and 15 km, subduction plate boundaries consist of 100 to 350-meter-thick fault zones cut by individual fault strands that are 5 to 35 meters thick with 1 to 20 cm thick cores. The characteristics of subduction thrusts at the depths where deep, slow slip events occur (30-45 km), however, are potentially different from the characteristics of thrusts near the surface.

Thus far, robust geologic indicators for slow slip have not been identified. Slip rates for slow slip events (~10^{-3}-10^{-4} mm/s (Bartlow et al., 2011; Colella et al., 2011, 2012; Rubin, 2011)) are much smaller than for "regular" earthquakes and hence are unlikely to produce appreciable frictional heating. Estimated slip rates of LFE patches are faster (~0.2 mm/s) than the estimated slip rates for SSEs on average (Bostock et al., 2015; Chestler & Creager, 2017; Thomas & Bostock, 2015), but are still much slower than the rates for "regular" earthquake slip. In addition, deformation mechanisms at depth (i.e., at higher temperatures and pressures) are much different than for crustal faults. In particular, SSEs occur in a transition between the locked zone, where

deformation occurs brittlely, and the aseismic zone, which is characterized by steady, ductile deformation.

A current concept linking geologic observations with SSE deformation is that slip occurs via mixed brittle and ductile deformation (Collettini et al., 2011; Fagereng, 2011; Fagereng et al., 2014; Fagereng & Sibson, 2010; Hayman & Lavier, 2014). In the Southern Marginal Zone of the Damara Belt, which formed by northward subduction at the time of Gondwana amalgamation (Barnes & Sawyer, 1980; Kasch, 1983), Fagereng et al. (2014) observes 10 to 100s meter-long basalt lenses interlayered with less rigid metapelites and metapsammites. They believe that brittle deformation occurs within and along the boundaries of the mafic lenses, whereas the metapelites and metapsammites deform via shearing flow. Hayman and Lavier (2014) observed mafic lenses enclosed within well-foliated gneiss within the Beagle Channel shear zone in southern Chile. Veins filled with blocky quartz crystals, consistent with immediate precipitation upon crack opening, cut across the center and tapered ends of the mafic lenses, which is indicative of brittle failure (Hayman & Lavier, 2014). Within the Monviso ophiolite, Angiboust et al. (2011) also observe evidence of mixed-mode deformation in the form of blocks of gabbroic basalt interspersed between sheared serpentine. The Monviso ophiolite, a well-preserved fragment of oceanic lithosphere, deformed under the eclogite facies (Angiboust et al., 2011) and hence represents deformation at the downdip edge of the slow slip zone.

Since we cannot probe the slow slip zone directly, studies such as those discussed above provide the only geologic observations so far that can inform a model for slow slip deformation. However, although the temperature/pressure conditions measured for the Southern Marginal and Beagle shear zones (400-600°C and 0.6-1.2 GPa) match the temperature and pressure conditions modeled for the slow slip zone (e.g., Gao & Wang, 2017; Hyndman & Wang, 1993), without a

direct indicator for slow slip, analogous to pseudotachylytes for "regular" earthquakes, one cannot be confident that the observed deformation occurred via slow slip. In addition, deformation during the process of exhumation, could complicate an inference that deformation occurred during slow slip.

Corroborating geologic studies with laboratory experiments, modeling studies, and seismic observations will help build a robust model for slow slip deformation. Thus far laboratory studies have shown that the same governing frictional dynamics that produce "regular" earthquakes can produce slow slip. Slow slip can be generated by slip-weakening behavior where the elastic stiffness is similar to or just larger than the fault stiffness (Ikari et al., 2013; Kaproth & Marone, 2013; Leeman et al., 2016). While some modeling studies reproduce slow slip patterns and rupture velocities by prescribing velocity-weakening behavior to the entire slip zone (e.g., Colella et al., 2011, 2012, 2013; Rubin, 2011), other studies posit a mixed shear zone with frictionally unstable patches characterized by velocity-weakening behavior or high initial traction surrounded by a stable background region (velocity strengthening or low traction) (Ando et al., 2010; Nakata et al., 2011; Skarbek et al., 2012). The latter appears more consistent with geological observations.

Chestler and Creager (in review) find that LFEs occur in distinct clusters around their family centroids. These clusters, or LFE family patches, are approximately 1 km^2 in area. Within these patches, LFEs slip on multiple smaller sub-patches within the overall family patch, which may be surrounded by a ductilely deforming matrix. Here, we find that the thicknesses of LFE family patches in the depth direction are 130 to 340 meters. This range of thicknesses provides a constraint on the width of slow slip deformation. Additionally, the fact that LFE families are not

vertically stacked is further evidence that the active shear zone, at the least part the deforms seismically, is thin (on the order of a few hundreds of meters).

If the outcrops studied by Fagereng et al. (2014) and Hayman and Lavier (2014) do represent places where slow slip occurred, perhaps LFEs are slip events within or on the margins of the mafic blocks. Both studies report that the individual mafic lenses are less than 10 m thick, but reach lengths ranging from 10s to 100s of meters. These lengths are in the range for estimates for the diameters of individual LFE events, which are on the order of 10 to 600 meters (Bostock et al., 2015; Chestler & Creager, 2017; Thomas et al., 2016). The Southern Marginal shear zone is comprised of sheared layers, 10s to 100s of meters thick (Fagereng et al., 2014) and the zone that accumulates shear strain in the Beagle Channel outcrop is ~1 km wide (Hayman & Lavier, 2014). These dimensions fit roughly with our 130 to 340-meter deformation thickness estimated from the range of LFE depths within individual LFE families.

Notably, Chestler and Creager (in review) found that observable LFEs are unevenly distributed over the slow slip zone. There are regions up to 20 km wide that contain no LFE families. Is it possible that mafic blocks are only present in some areas of the slow slip zone and in other areas (where mafic blocks may not be present) slip primarily occurs ductilely? Both the Southern Marginal and Beagle Channel outcrops are less than 10 km in length, and hence do not represent the entire slow slip zone, which is greater than 50 km wide. Therefore, even if we assume that mafic blocks represent areas where LFE occur, these geologic studies cannot entirely address the variability in LFE family density across the entire slow slip zone.

4.3 Implications for the LVZ and the role of fluids in slow slip

While the LVZ is often identified by its low S-wave velocity and high V_p/V_s, we believe that it is visible in the Preston et al. (2003) 3-D P-wave velocity model (Figure 4.2). In all three of our cross sections there is a layer approximately 5 to 7 km thick where the seismic velocity decreases by 7% relative to that of the material directly above it.

Our LFE families lie directly above the layer we interpret as the LVZ. Because LFEs occur on the plate interface, this situates the LVZ within the crust of the subducting oceanic plate. Using 3D waveform modeling to create synthetic LFE seismograms, Nowack and Bostock (2013) also concluded that LFEs sit atop the LVZ. They identified scattered phases within LFE template waveforms and found that the timing of the ŚP and ŚS scattered phases and the simplicity of the P arrivals match most closely with the synthetic seismograms produced by LFEs located at the top of the LVZ.

Our results, as well as the results from Nowack and Bostock (2013), support the explanation for the LVZ advocated by Bostock (2013)—that the LVZ comprises of fluid-rich pillow basalts and sheeted dikes in the upper oceanic crust. A summary of Bostock's (2013) model for the subduction-zone processes that result in the LVZ is as follows: (1) fluids are incorporated into the upper oceanic plate through hydrothermal circulation at the spreading center and through the absorption of water into hydrous minerals during spreading, (2) as the oceanic plate subducts increased temperatures and pressures cause dehydration reactions that liberate fluids, (3) fluids are trapped in the upper oceanic crust due to an impermeable upper plate (Audet et al., 2009; Hyndman, 1988; Peacock et al., 2011) and an impermeable, gabbroic lower oceanic crust, (4) trapped fluids result in high pore pressures in the upper crust, which creates the prominent LVZ, (5) metamorphic reactions culminate with the onset of eclogitization at about 45 km depth, which liberates the remaining fluids and causes volumetric changes that

rupture the plate boundary seal, and (6) the combination of eclogitization in the oceanic crust and serpentinization in the mantle wedge due to fluid penetration erases the contrast of the LVZ with the overlying continental Moho, again at depths of ~45 km.

Not only are the above processes thought to be responsible for the expression of the LVZ, fluids are proposed to play a key role in generating slow slip (Audet et al., 2009; Audet & Bürgmann, 2014; Hyndman et al., 2015). Both Shelly et al. (2006) and Bostock et al. (2012), who examine LFE families in the Nankai Trough and beneath Vancouver Island respectively, propose that fluids trapped at the top of the LVZ decrease the effective normal stress on the plate interface, allowing for brittle failure (i.e., LFEs) to occur on small patches. Given the locations of our LFE families at the top of the LVZ, where trapped fluids are thought to reside, we agree with this interpretation.

The "regular" earthquakes located by Preston et al. (2003) sit approximately 5 km below our LFE families and at the base of the LVZ (Figure 4.3). Shelly et al. (2006) and Bostock et al. (2012) also observe the vertical separation between LFEs and intraslab earthquakes. Bostock et al. (2012) further proposes that low shear strength from high pore fluid pressures does not allow the LVZ to support earthquakes.

5 Conclusions

Using high-resolution relative LFE locations we find that the depth of LFE families beneath the Olympic Peninsula are most consistent with the McCrory et al. (2012) plate interface model. However, looking along strike, the depths of LFE families at constant downdip distances dip ~10 to 25° to the north, indicating significant along-strike variations in plate interface depth

over distances of ~5 km. High-precision locations of more LFE families would help illuminate complex geometry in the along-strike structure of the plate interface.

We find that LFEs sit directly atop the low-velocity zone and ~5 km above intraslab earthquakes. This supports the explanation for the LVZ proposed by Bostock (2013)—that the LVZ comprises the upper oceanic crust and is composed of fluid-rich pillow basalts, sheeted dikes, and sediments. In this view, fluids are primarily responsible for the velocity contrast between the LVZ and surrounding layers and also play a key role in the generation of slow slip and LFEs.

The range of LFE depths in individual LFE families is 130 to 340 meters, which gives an upper bound on the thickness of slow slip deformation. Our error analysis suggests that the values could be ~50% smaller. While the mechanism for slow slip deformation is still a current topic of study, researchers observe mafic blocks surrounded by material that appears to have deformed ductiley in exhumed subduction zones that may have hosted slow slip (Collettini et al., 2011; Fagereng, 2011; Fagereng et al., 2014; Fagereng & Sibson, 2010; Hayman & Lavier, 2014)). We suggest that LFEs might be generated by slip in and along the edges of the mafic blocks. Deformed layers within the outcrops studied in Fagerang et al. (2014) and Hayman and Lavier (2014) are 10s to 100s of meters thick, on par with the deformation width we estimate from LFEs.

High-resolution LFE locations have the power to illuminate subduction zone plate interface geometries, depths, and thicknesses throughout Cascadia and in other subduction zones worldwide. LFEs are an important tool for constraining how deformation occurs during slow slip. Studies of LFE locations should be corroborated with geological, laboratory, and modeling studies of slow slip to give a complete idea of the mechanism for slow slip.

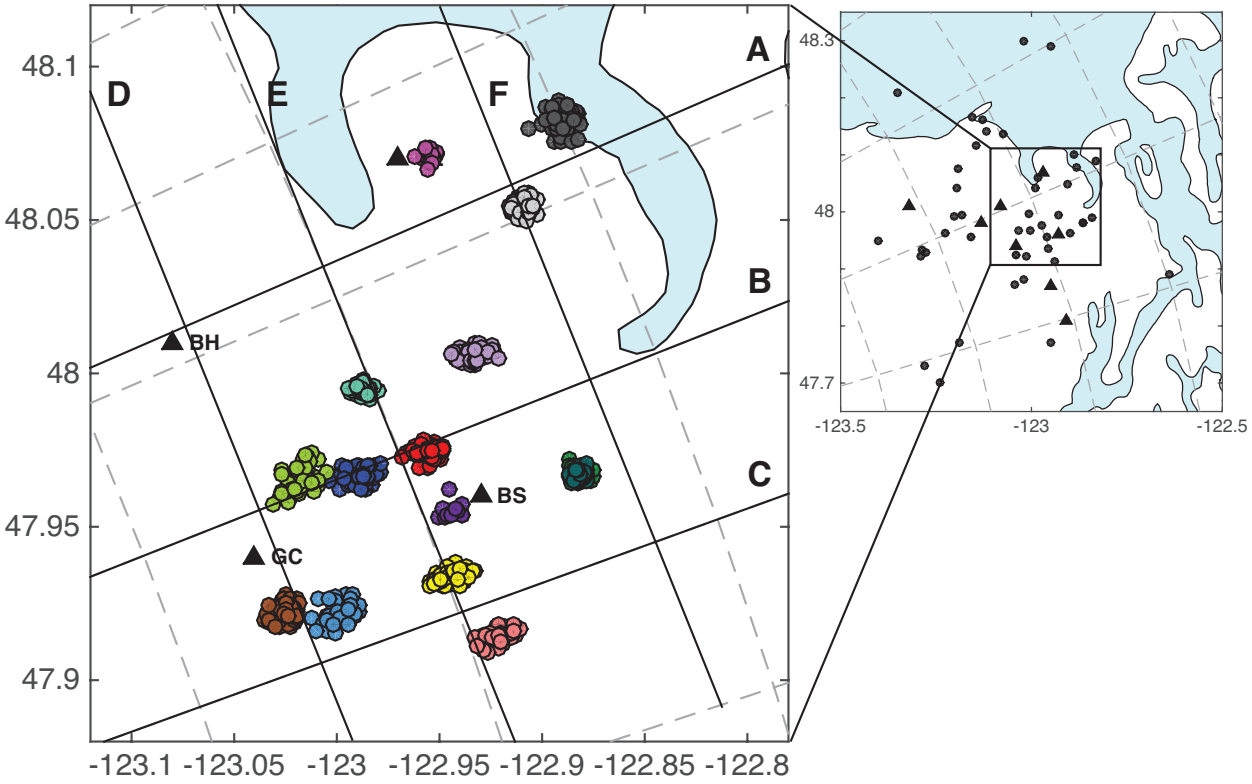

Figure 4.1: Relocated LFEs in the east cluster of LFE families from Chestler and Creager (in press). LFEs (colored dots) are color-coded by LFE family; each LFE family is a different color. AofA arrays are black triangles. Lines A, B, and C indicate the downdip profiles used for the cross sections in Figure 4.2. Each downdip profile has a constant along-strike distance (801, 795, and 790 km for A, B, and C respectively) from the southernmost limit of the CSZ in Northern California. Line D, E, and F indicate the along-strike profiles used for the cross sections in Figure 4.3. The along-strike profiles have constant downdip distances (35, 40.5, and 48 km respectively). The inset shows the locations of all the LFE families from the Chestler and Creager (in press) catalog (black dots) and the locations of AofA arrays and CAFE stations used to locate LFE families (black triangles).

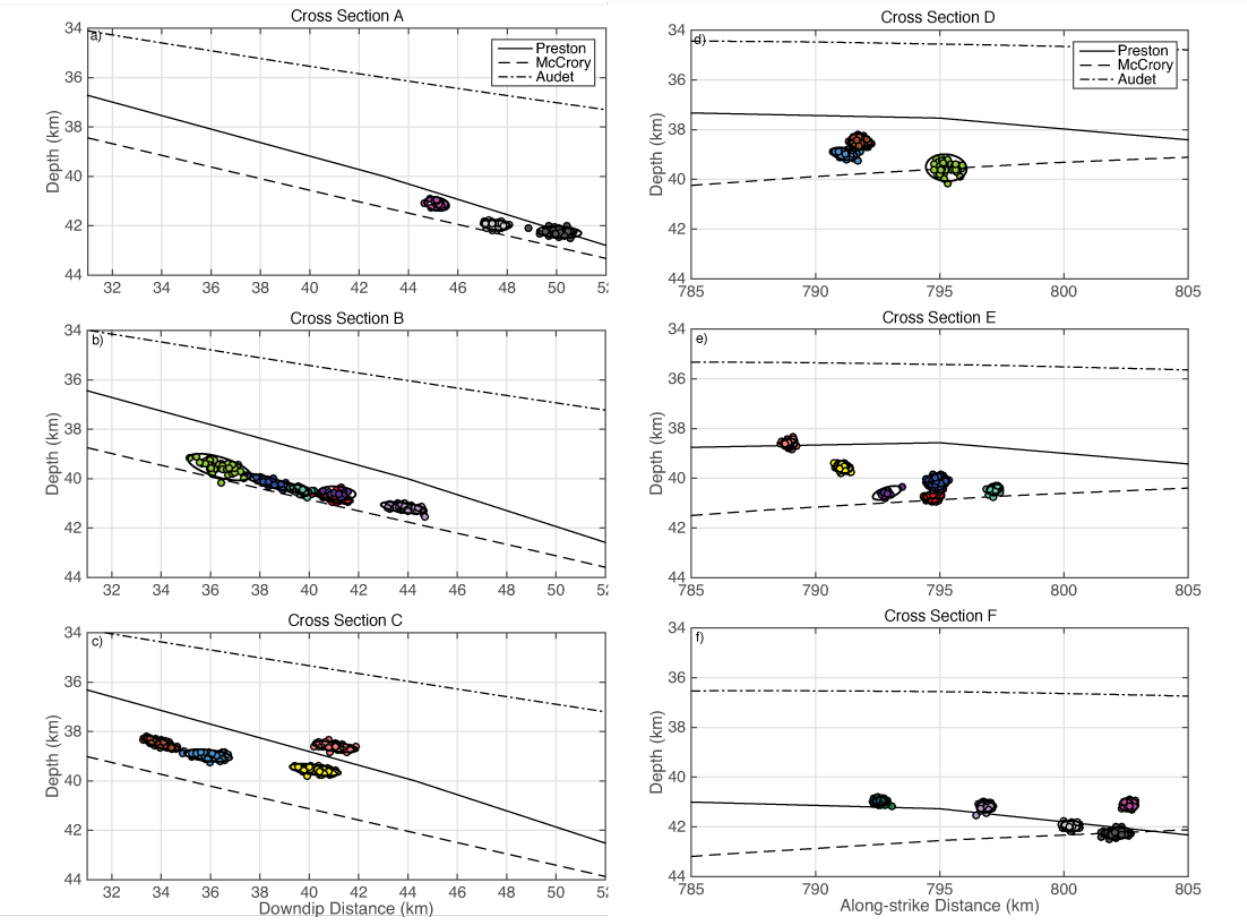

Figure 4.2: Cross sections for profiles A, B, C, D, E, and F. LFEs are dots colored coded by LFE family. The Preston, McCrory, and Audet plate interface models are shown as solid, dotted, and dot-dashed lines respectively. Black ellipses indicate the 95% confidence ellipses in the depth/downdip plane for 60-80% of the LFEs in each family.

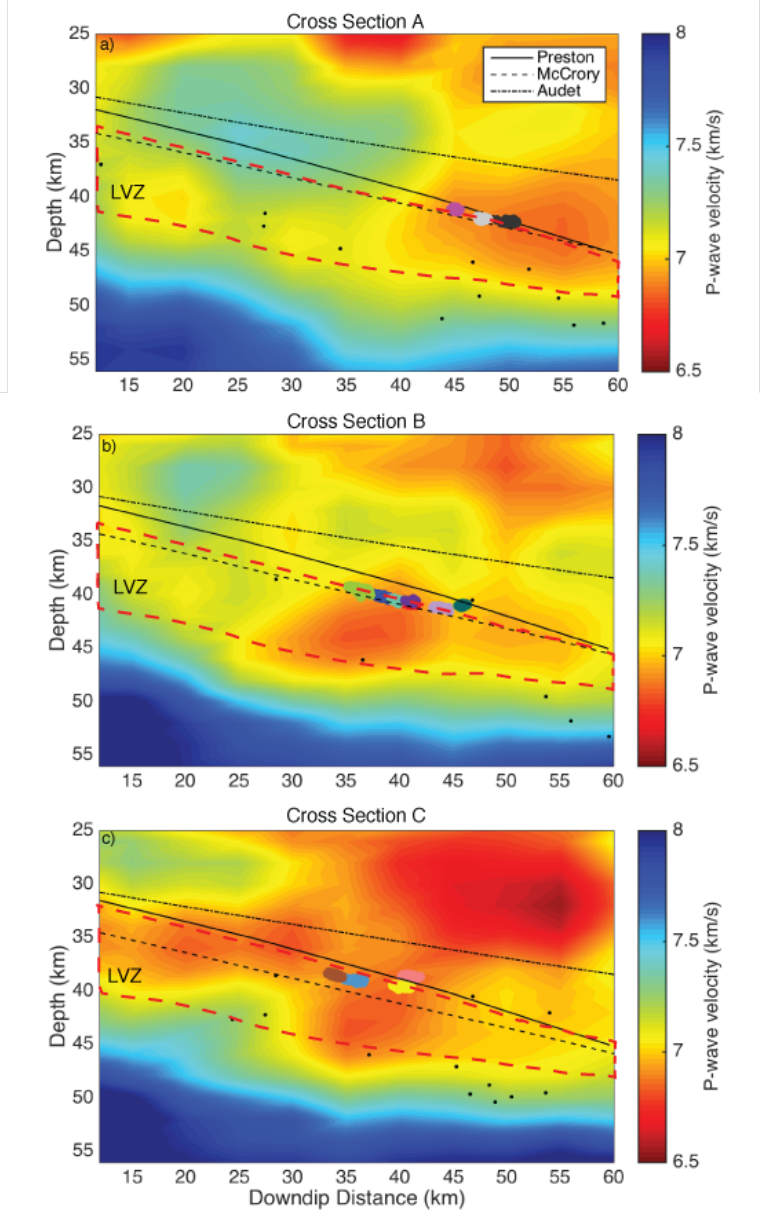

Figure 4.3: Cross sections A, B, and C plotted with the Preston et al. (2003) P-wave velocity model in the background. LVZ is indicated by the dotted red line.

Summary & Future Work

This work consists of three chapters that forward the scientific understanding of the LFE source process, how LFEs are related to geodetically observed slow slip, and how LFEs can be used to investigate plate interface structure. Key findings include that:

1. The moment frequency distribution for LFEs is exponential, which implies a scale-limited source-process,
2. LFEs within a single LFE family likely slip on multiple sub-patches within the LFE family patch,
3. LFEs cluster into families and clusters of families, between which are gaps where slip occurs without producing observable, repeating LFEs,
4. LFE family patches have diameters of 600-1600 meters (areas of 0.3-2 km^2),
5. In regions with the most LFEs only ~0.2% of the geodetically determined slip during ETS events occurs via LFEs,
6. The thicknesses of LFE families in the depth direction is 130-340 meters, which is a proxy for the thickness of deformation on the plate interface,
7. LFE families lie on top of the LVZ and their depths beneath the Olympic Peninsula correspond most closely with the McCrory et al. (2012) plate model, and
8. Along-strike variations in LFE depth indicate that the plate interface is not smooth.

These findings, and in particular findings 3 and 5, show that there are limitations to using LFEs as slip indicators. LFEs can only indicate when slow slip is occurring at the locations of LFE families. Hence, while LFEs are good indicators for when and where slow slip is happening in general, their coverage is limited. Even during ETS events geodesy does not have the spatial resolution to infer whether slip is happening between LFE families. Additionally, LFEs only

represent a very small proportion (~0.2%) of the geodetically observed slow slip. Therefore, they are not useful tools for quantifying the total amount of slip that occurs during SSEs. While slip can be inferred from geodetic measurements for large SSEs (i.e., ETS events), as of now there is no method for quantifying the amount of slip that occurs during individual, small SSEs. Frank (2016) made a step towards quantifying inter-ETS slip. He summed geodetic observations of many small SSEs to infer the amount of slip averaged over many small events. One limitation to this work is that our catalog only spans two ETS events for which we can compare LFE slip to geodetically observed slow slip. A catalog that spans a larger amount of time would be useful for developing a scaling relationship between observed LFE slip and the total amount of slow slip that occurs during SSEs.

Another limitation to this work is that we only study LFE families beneath the Olympic Peninsula, WA, a small sub-portion of the Cascadia Subduction Zone. LFEs have been observed in many other parts of Cascadia, including beneath Vancouver Island (Bostock et al., 2012), throughout northern Washington (Royer and Bostock, 2013), and beneath Northern California (Plourde et al., 2015), and in other subduction zones (e.g. Mexico and Japan). Thorough analysis of LFEs in other regions will lead to further insight on the role LFEs play in the slow slip process. In particular, LFE moments have only been measured beneath the Olympic Peninsula, WA (this work, Sweet et al., 2014) and Vancouver Island, Canada (Bostock et al., 2015). Calculating LFE moments in other regions will (1) help us understand why our LFE moments are so much smaller than the LFE moments in Bostock et al. (2015) and (2) give a view of the full range of LFE moments in subduction zones worldwide. Additionally, calculating the portion of geodetically observed slip that LFEs represent in other regions where both LFEs and slow slip

are observed (e.g., Mexico and Japan), as we did in chapter two, would be useful to further constrain the role that LFEs play in generating slow slip.

Finally, we have demonstrated the usefulness of high-precision LFE locations for investigating plate interface structure. We implore other workers, where good data is available, to also relocate individual LFEs. This could (1) further allow the quantification of the thickness of deformation in the slow slip zone, (2) verify that LFE families are elongate in the downdip direction (or the direction of plate motion), and (3) map out along-strike variations in plate interface depth over large areas. In addition, LFEs sit at the top of the LVZ observed by Audet et al. (2010) and Preston et al. (2003). Nowack and Bostock (2013) demonstrate the use of 3D modeling of LFE waveforms to investigate the relationship between LFEs and plate interface structure, including the LVZ. Analysis similar to that of Nowack and Bostock (2013) could be performed using my catalog in the future.

Wide-scale observations of where we do and do not observe LFE families, the size family patches, and the distribution of LFEs within LFE family patches could broaden our understanding of the role that both brittle and ductile deformation processes play in driving slow slip.

Acknowledgements

Special thanks to Abhijit Ghosh for proving the stacked tremor waveforms used to search for LFE families. We thank Heidi Houston, David Schmidt, and William Wilcock for useful discussions and feedback on an early presentation of this work and Justin Sweet, whose PhD research is the foundation for this research. Kelley Hall provided the GPS inversions of slip from the 2010 and 2011 ETS events that we used to calculate A_T. We thank Michael Bostock for sharing the Royer et al. (2015) LFE catalog and Yajun Peng for directing us to the Peng and Rubin (2016) short-window detection catalog. Finally, we thank Darrell Cowen for fruitful discussions about fault mechanics and deformation. All the waveforms from the Array of Arrays and CAFÉ experiments can be found at the IRIS Data Management Center. This study was supported by National Science Foundation grants, EAR0844392 and EAR1358512.

References

Abers, G. A., MacKenzie, L. S., Rondenay, S., Zhang, Z., Wech, A. G., & Creager, K. C. (2009). Imaging the source region of Cascadia tremor and intermediate-depth earthquakes. *Geology*, *37*(12), 1119–1122. https://doi.org/10.1130/G30143A.1

Allmann, B. P., & Shearer, P. M. (2009). Global variations of stress drop for moderate to large earthquakes. *Journal of Geophysical Research: Solid Earth*, *114*(B1), B01310. https://doi.org/10.1029/2008JB005821

Ando, R., Nakata, R., & Hori, T. (2010). A slip pulse model with fault heterogeneity for low-frequency earthquakes and tremor along plate interfaces. *Geophysical Research Letters*, *37*(10), L10310. https://doi.org/10.1029/2010GL043056

Angiboust, S., Agard, P., Raimbourg, H., Yamato, P., & Huet, B. (2011). Subduction interface processes recorded by eclogite-facies shear zones (Monviso, W. Alps). *Lithos*, *127*(1), 222–238. https://doi.org/10.1016/j.lithos.2011.09.004

Atwater, B. F. (1987). Evidence for Great Holocene Earthquakes along the Outer Coast of Washington State. *Science*, *236*(4804), 942–944. https://doi.org/10.2307/1699641

Atwater, B. F. (1992). Geologic evidence for earthquakes during the past 2000 years along the Copalis River, southern coastal Washington. *Journal of Geophysical Research: Solid Earth*, *97*(B2), 1901–1919. https://doi.org/10.1029/91JB02346

Audet, P., Bostock, M. G., Boyarko, D. C., Brudzinski, M. R., & Allen, R. M. (2010). Slab morphology in the Cascadia fore arc and its relation to episodic tremor and slip. *Journal of Geophysical Research: Solid Earth*, *115*(B4), B00A16. https://doi.org/10.1029/2008JB006053

Audet, P., Bostock, M. G., Christensen, N. I., & Peacock, S. M. (2009). Seismic evidence for overpressured subducted oceanic crust and megathrust fault sealing. *Nature*, *457*(7225), 76–78. https://doi.org/10.1038/nature07650

Baltay, A. S., & Beroza, G. C. (2013). Ground-motion prediction from tremor. *Geophysical Research Letters*, *40*(24), 2013GL058506. https://doi.org/10.1002/2013GL058506

Barnes, S.-J., & Sawyer, E. W. (1980). An alternative model for the Damara Mobile Belt: Ocean crust subduction and continental convergence. *Precambrian Research*, *13*(4), 297–336. https://doi.org/10.1016/0301-9268(80)90048-0

Bartlow, N. M., Miyazaki, S., Bradley, A. M., & Segall, P. (2011). Space-time correlation of slip and tremor during the 2009 Cascadia slow slip event. *Geophysical Research Letters*, *38*(18), L18309. https://doi.org/10.1029/2011GL048714

Beeler, N. M., Thomas, A., Bürgmann, R., & Shelly, D. (2013). Inferring fault rheology from low-frequency earthquakes on the San Andreas. *Journal of Geophysical Research: Solid Earth*, *118*(11), 2013JB010118. https://doi.org/10.1002/2013JB010118

Bostock, M. G. (2013). The Moho in subduction zones. *Tectonophysics*, *609*, 547–557. https://doi.org/10.1016/j.tecto.2012.07.007

Bostock, M. G., Royer, A. A., Hearn, E. H., & Peacock, S. M. (2012). Low frequency earthquakes below southern Vancouver Island. *Geochemistry, Geophysics, Geosystems*, *13*(11), Q11007. https://doi.org/10.1029/2012GC004391

Bostock, M. G., Thomas, A. M., Savard, G., Chuang, L., & Rubin, A. M. (2015). Magnitudes and moment-duration scaling of low-frequency earthquakes beneath southern Vancouver Island. *Journal of Geophysical Research: Solid Earth*, *120*(9), 2015JB012195. https://doi.org/10.1002/2015JB012195

Brown, J. R., Prejean, S. G., Beroza, G. C., Gomberg, J. S., & Haeussler, P. J. (2013). Deep low-frequency earthquakes in tectonic tremor along the Alaska-Aleutian subduction zone. *Journal of Geophysical Research: Solid Earth*, *118*(3), 1079–1090. https://doi.org/10.1029/2012JB009459

Brown, J. R., Beroza, G. C., & Shelly, D. R. (2008). An autocorrelation method to detect low frequency earthquakes within tremor. *Geophysical Research Letters*, *35*(16), L16305. https://doi.org/10.1029/2008GL034560

Brown, K. M., Tryon, M. D., DeShon, H. R., Dorman, L. M., & Schwartz, S. Y. (2005). Correlated transient fluid pulsing and seismic tremor in the Costa Rica subduction zone. *Earth and Planetary Science Letters*, *238*(1), 189–203. https://doi.org/10.1016/j.epsl.2005.06.055

Brudzinski, M. R., & Allen, R. M. (2007). Segmentation in episodic tremor and slip all along Cascadia. *Geology*, *35*(10), 907–910. https://doi.org/10.1130/G23740A.1

Calvert, A. J., & Clowes, R. M. (1990). Deep, high-amplitude reflections from a major shear zone above the subducting Juan de Fuca plate. *Geology*, *18*(11), 1091–1094. https://doi.org/10.1130/0091-7613(1990)018<1091:DHARFA>2.3.CO;2

Chamberlain, C. J., Shelly, D. R., Townend, J., & Stern, T. A. (2014). Low-frequency earthquakes reveal punctuated slow slip on the deep extent of the Alpine Fault, New Zealand. *Geochemistry, Geophysics, Geosystems*, *15*(7), 2984–2999. https://doi.org/10.1002/2014GC005436

Chestler, S. R., & Creager, K. C. (2017). Evidence for a scale-limited Low-Frequency Earthquake source process. *Journal of Geophysical Research: Solid Earth*, 2016JB013717. https://doi.org/10.1002/2016JB013717

Colella, H. V., Dieterich, J. H., & Richards-Dinger, K. B. (2011). Multi-event simulations of slow slip events for a Cascadia-like subduction zone. *Geophysical Research Letters*, *38*(16), L16312. https://doi.org/10.1029/2011GL048817

Colella, H. V., Dieterich, J. H., Richards-Dinger, K., & Rubin, A. M. (2012). Complex characteristics of slow slip events in subduction zones reproduced in multi-cycle simulations. *Geophysical Research Letters*, *39*(20), L20312. https://doi.org/10.1029/2012GL053276

Collettini, C., Niemeijer, A., Viti, C., Smith, S. A. F., & Marone, C. (2011). Fault structure, frictional properties and mixed-mode fault slip behavior. *Earth and Planetary Science Letters*, *311*(3), 316–327. https://doi.org/10.1016/j.epsl.2011.09.020

Compton, K. E., Kirkpatrick, J. D., & Holk, G. J. (2017). Cyclical shear fracture and viscous flow during transitional ductile-brittle deformation in the Saddlebag Lake Shear Zone, California. *Tectonophysics*, *708*, 1–14. https://doi.org/10.1016/j.tecto.2017.04.006

Cowan, D. S. (1999). Do faults preserve a record of seismic slip? A field geologist's opinion. *Journal of Structural Geology*, *21*, 995–1001. https://doi.org/10.1016/S0191-8141(99)00046-2

Daub, E. G., Shelly, D. R., Guyer, R. A., & Johnson, P. A. (2011). Brittle and ductile friction and the physics of tectonic tremor. *Geophysical Research Letters*, *38*(10), L10301. https://doi.org/10.1029/2011GL046866

Douglas, A., Beavan, J., Wallace, L., & Townend, J. (2005). Slow slip on the northern Hikurangi subduction interface, New Zealand. *Geophysical Research Letters*, *32*(16), L16305. https://doi.org/10.1029/2005GL023607

Dragert, H., Wang, K., & James, T. S. (2001). A Silent Slip Event on the Deeper Cascadia Subduction Interface. *Science*, *292*(5521), 1525–1528. https://doi.org/10.1126/science.1060152

Fagereng, Å. (2011). Geology of the seismogenic subduction thrust interface. *Geological Society, London, Special Publications*, *359*(1), 55–76. https://doi.org/10.1144/SP359.4

Fagereng, Å., Hillary, G. W. B., & Diener, J. F. A. (2014). Brittle-viscous deformation, slow slip, and tremor. *Geophysical Research Letters*, *41*(12), 4159–4167. https://doi.org/10.1002/2014GL060433

Fagereng, Å., & Sibson, R. H. (2010). Mélange rheology and seismic style. *Geology*, *38*(8), 751–754. https://doi.org/10.1130/G30868.1

Frank, W. B. (2016). Slow slip hidden in the noise: The intermittence of tectonic release. *Geophysical Research Letters*, *43*(19), 2016GL069537. https://doi.org/10.1002/2016GL069537

Frank, W. B., Shapiro, N. M., Husker, A. L., Kostoglodov, V., Romanenko, A., & Campillo, M. (2014). Using systematically characterized low-frequency earthquakes as a fault probe in Guerrero, Mexico. *Journal of Geophysical Research: Solid Earth*, *119*(10), 7686–7700. https://doi.org/10.1002/2014JB011457

Frank, W. B., Radiguet, M., Rousset, B., Shapiro, N. M., Husker, A. L., Kostoglodov, V., … Campillo, M. (2015). Uncovering the geodetic signature of silent slip through repeating earthquakes. *Geophysical Research Letters*, *42*(8), 2015GL063685. https://doi.org/10.1002/2015GL063685

Frank, W. B., Shapiro, N. M., Kostoglodov, V., Husker, A. L., Campillo, M., Payero, J. S., & Prieto, G. A. (2013). Low-frequency earthquakes in the Mexican Sweet Spot. *Geophysical Research Letters*, *40*(11), 2661–2666. https://doi.org/10.1002/grl.50561

Ghosh, A., Vidale, J. E., & Creager, K. C. (2012). Tremor asperities in the transition zone control evolution of slow earthquakes. *Journal of Geophysical Research: Solid Earth*, *117*(B10), B10301. https://doi.org/10.1029/2012JB009249

Ghosh, A., Huesca-Pérez, E., Brodsky, E., & Ito, Y. (2015). Very low frequency earthquakes in Cascadia migrate with tremor. *Geophysical Research Letters*, *42*(9), 2015GL063286. https://doi.org/10.1002/2015GL063286

Gomberg, J., Creager, K., Sweet, J., Vidale, J., Ghosh, A., & Hotovec, A. (2012). Earthquake spectra and near-source attenuation in the Cascadia subduction zone. *Journal of Geophysical Research: Solid Earth*, *117*(B5), B05312. https://doi.org/10.1029/2011JB009055

Hall, K., & Houston, H. (2014). Slip Updip of Tremor during the 2012 Cascadia ETS Event. *AGU Fall Meeting Abstracts*, *53*. Retrieved from http://adsabs.harvard.edu/abs/2014AGUFM.S53C4516H

Hansen, R. T. J., Bostock, M. G., & Christensen, N. I. (2012). Nature of the low velocity zone in Cascadia from receiver function waveform inversion. *Earth and Planetary Science Letters*, *337*, 25–38. https://doi.org/10.1016/j.epsl.2012.05.031

Hawthorne, J. C., & Rubin, A. M. (2013). Laterally propagating slow slip events in a rate and state friction model with a velocity-weakening to velocity-strengthening transition. *Journal of Geophysical Research: Solid Earth*, *118*(7), 3785–3808. https://doi.org/10.1002/jgrb.50261

Hawthorne, J. C., Bostock, M. G., Royer, A. A., & Thomas, A. M. (2016). Variations in slow slip moment rate associated with rapid tremor reversals in Cascadia. *Geochemistry, Geophysics, Geosystems*, *17*(12), 4899–4919. https://doi.org/10.1002/2016GC006489

Hayman, N. W., & Lavier, L. L. (2014). The geologic record of deep episodic tremor and slip. *Geology*, *42*(3), 195–198. https://doi.org/10.1130/G34990.1

Hyndman, R. D. (1988). Dipping Seismic Reflectors, Electrically Conductive Zones, and Trapped Water in the Crust Over a Subducting Plate. *Journal of Geophysical Research: Solid Earth*, *93*(B11), 13391–13405. https://doi.org/10.1029/JB093iB11p13391

Ide, S. (2016). Characteristics of slow earthquakes in the very low frequency band: Application to the Cascadia subduction zone. *Journal of Geophysical Research: Solid Earth*, *121*(8), 2016JB013085. https://doi.org/10.1002/2016JB013085

Ide, S., Shelly, D. R., & Beroza, G. C. (2007). Mechanism of deep low frequency earthquakes: Further evidence that deep non-volcanic tremor is generated by shear slip on the plate interface. *Geophysical Research Letters*, *34*(3), L03308. https://doi.org/10.1029/2006GL028890

Jiang, Y., Wdowinski, S., Dixon, T. H., Hackl, M., Protti, M., & Gonzalez, V. (2012). Slow slip events in Costa Rica detected by continuous GPS observations, 2002–2011. *Geochemistry, Geophysics, Geosystems*, *13*(4), Q04006. https://doi.org/10.1029/2012GC004058

Kanamori, H., & Anderson, D. L. (1975a). Theoretical basis of some empirical relations in seismology. *Bulletin of the Seismological Society of America*, *65*(5), 1073–1095.

Kanamori, H., & Anderson, D. L. (1975b). Theoretical basis of some empirical relations in seismology. *Bulletin of the Seismological Society of America*, *65*(5), 1073–1095.

Kao, H., Wang, K., Dragert, H., Kao, J. Y., & Rogers, G. (2010). Estimating seismic moment magnitude (Mw) of tremor bursts in northern Cascadia: Implications for the "seismic efficiency" of episodic tremor and slip. *Geophysical Research Letters*, *37*(19), L19306. https://doi.org/10.1029/2010GL044927

Kasch, K. W. (1983). Tectonothermal evolution of the southern Damara Orogen. *Special Publication of the Geological Society of South Africa*, *11*, 255–265.

Kim, M. J., Schwartz, S. Y., & Bannister, S. (2011). Non-volcanic tremor associated with the March 2010 Gisborne slow slip event at the Hikurangi subduction margin, New Zealand. *Geophysical Research Letters*, *38*(14), L14301. https://doi.org/10.1029/2011GL048400

Kostoglodov, V., Singh, S. K., Santiago, J. A., Franco, S. I., Larson, K. M., Lowry, A. R., & Bilham, R. (2003). A large silent earthquake in the Guerrero seismic gap, Mexico. *Geophysical Research Letters*, *30*(15), 1807. https://doi.org/10.1029/2003GL017219

McCrory, P. A., Blair, J. L., Waldhauser, F., & Oppenheimer, D. H. (2012). Juan de Fuca slab geometry and its relation to Wadati-Benioff zone seismicity. *Journal of Geophysical Research: Solid Earth*, *117*(B9), B09306. https://doi.org/10.1029/2012JB009407

Nadeau, R. M., Foxall, W., & McEvilly, T. V. (1995). Clustering and Periodic Recurrence of Microearthquakes on the San Andreas Fault at Parkfield, California. *Science*, *267*(5197), 503–507.

Nakata, R., Ando, R., Hori, T., & Ide, S. (2011). Generation mechanism of slow earthquakes: Numerical analysis based on a dynamic model with brittle-ductile mixed fault heterogeneity. *Journal of Geophysical Research: Solid Earth*, *116*(B8), B08308. https://doi.org/10.1029/2010JB008188

Nicholson, T., Bostock, M., & Cassidy, J. F. (2005). New constraints on subduction zone structure in northern Cascadia. *Geophysical Journal International*, *161*(3), 849–859. https://doi.org/10.1111/j.1365-246X.2005.02605.x

Nowack, R. L., & Bostock, M. G. (2013). Scattered waves from low-frequency earthquakes and plate boundary structure in northern Cascadia. *Geophysical Research Letters*, *40*(16), 4238–4243. https://doi.org/10.1002/grl.50826

Obara, K. (2002). Nonvolcanic Deep Tremor Associated with Subduction in Southwest Japan. *Science*, *296*(5573), 1679–1681. https://doi.org/10.1126/science.1070378

Obara, K., Hirose, H., Yamamizu, F., & Kasahara, K. (2004). Episodic slow slip events accompanied by non-volcanic tremors in southwest Japan subduction zone. *Geophysical Research Letters*, *31*(23), L23602. https://doi.org/10.1029/2004GL020848

Ohta, Y., Freymueller, J. T., Hreinsdóttir, S., & Suito, H. (2006). A large slow slip event and the depth of the seismogenic zone in the south central Alaska subduction zone. *Earth and Planetary Science Letters*, *247*(1), 108–116. https://doi.org/10.1016/j.epsl.2006.05.013

Paige, C. C., & Saunders, M. A. (1982). LSQR: Sparse linear equations and least squares problems,. *ACM Transactions on Mathematical Software*, *8/2*, 195–209.

Payero, J. S., Kostoglodov, V., Shapiro, N., Mikumo, T., Iglesias, A., Pérez-Campos, X., & Clayton, R. W. (2008). Nonvolcanic tremor observed in the Mexican subduction zone. *Geophysical Research Letters*, *35*(7), L07305. https://doi.org/10.1029/2007GL032877

Peng, Y., & Rubin, A. M. (2016). High-resolution images of tremor migrations beneath the Olympic Peninsula from stacked array of arrays seismic data. *Geochemistry, Geophysics, Geosystems*, *17*(2), 587–601. https://doi.org/10.1002/2015GC006141

Peng, Z., & Gomberg, J. (2010). An integrated perspective of the continuum between earthquakes and slow-slip phenomena. *Nature Geoscience*, *3*(9), 599–607. https://doi.org/10.1038/ngeo940

Peterson, C. L., & Christensen, D. H. (2009). Possible relationship between nonvolcanic tremor and the 1998–2001 slow slip event, south central Alaska. *Journal of Geophysical Research: Solid Earth*, *114*(B6), B06302. https://doi.org/10.1029/2008JB006096

Plourde, A. P., Bostock, M. G., Audet, P., & Thomas, A. M. (2015). Low-frequency earthquakes at the southern Cascadia margin. *Geophysical Research Letters*, *42*(12), 2015GL064363. https://doi.org/10.1002/2015GL064363

Preston, L. A., Creager, K. C., Crosson, R. S., Brocher, T. M., & Trehu, A. M. (2003). Intraslab Earthquakes: Dehydration of the Cascadia Slab. *Science*, *302*(5648), 1197–1200. https://doi.org/10.1126/science.1090751

Rogers, G., & Dragert, H. (2003). Episodic Tremor and Slip on the Cascadia Subduction Zone: The Chatter of Silent Slip. *Science*, *300*(5627), 1942–1943. https://doi.org/10.1126/science.1084783

Rondenay, S., Bostock, M. G., & Shragge, J. (2001). Multiparameter two-dimensional inversion of scattered teleseismic body waves 3. Application to the Cascadia 1993 data set. *Journal of Geophysical Research: Solid Earth*, *106*(B12), 30795–30807. https://doi.org/10.1029/2000JB000039

Rowe, C. D., & Griffith, W. A. (2015). Do faults preserve a record of seismic slip: A second opinion. *Journal of Structural Geology*, *78*(Supplement C), 1–26. https://doi.org/10.1016/j.jsg.2015.06.006

Rowe, C. D., Moore, J. C., & Remitti, F. (2013). The thickness of subduction plate boundary faults from the seafloor into the seismogenic zone. *Geology*, *41*(9), 991–994. https://doi.org/10.1130/G34556.1

Royer, A. A., & Bostock, M. G. (2014). A comparative study of low frequency earthquake templates in northern Cascadia. *Earth and Planetary Science Letters*, *402*, 247–256. https://doi.org/10.1016/j.epsl.2013.08.040

Royer, A. A., Thomas, A. M., & Bostock, M. G. (2015). Tidal modulation and triggering of low-frequency earthquakes in northern Cascadia. *Journal of Geophysical Research: Solid Earth*, *120*(1), 2014JB011430. https://doi.org/10.1002/2014JB011430

Rubin, A. M. (2011). Designer friction laws for bimodal slow slip propagation speeds. *Geochemistry, Geophysics, Geosystems*, *12*(4), Q04007. https://doi.org/10.1029/2010GC003386

Rubin, A. M., & Armbruster, J. G. (2013). Imaging slow slip fronts in Cascadia with high precision cross-station tremor locations. *Geochemistry, Geophysics, Geosystems*, *14*(12), 5371–5392. https://doi.org/10.1002/2013GC005031

Savage, H. M., & Brodsky, E. E. (2011). Collateral damage: Evolution with displacement of fracture distribution and secondary fault strands in fault damage zones. *Journal of Geophysical Research: Solid Earth*, *116*(B3), B03405. https://doi.org/10.1029/2010JB007665

Schmidt, D. A., & Gao, H. (2010). Source parameters and time-dependent slip distributions of slow slip events on the Cascadia subduction zone from 1998 to 2008. *Journal of Geophysical Research: Solid Earth*, *115*(B4), B00A18. https://doi.org/10.1029/2008JB006045

Shearer, P. M. (2009). *Introduction to Seismology*. Cambridge University Press.

Shelly, D. R. (2010). Periodic, Chaotic, and Doubled Earthquake Recurrence Intervals on the Deep San Andreas Fault. *Science*, *328*(5984), 1385–1388. https://doi.org/10.1126/science.1189741

Shelly, D. R., & Hardebeck, J. L. (2010). Precise tremor source locations and amplitude variations along the lower-crustal central San Andreas Fault. *Geophysical Research Letters*, *37*(14), L14301. https://doi.org/10.1029/2010GL043672

Shelly, D. R., Beroza, G. C., & Ide, S. (2007). Non-volcanic tremor and low-frequency earthquake swarms. *Nature*, *446*(7133), 305–307. https://doi.org/10.1038/nature05666

Shelly, D. R., Beroza, G. C., Ide, S., & Nakamula, S. (2006). Low-frequency earthquakes in Shikoku, Japan, and their relationship to episodic tremor and slip. *Nature*, *442*(7099), 188–191. https://doi.org/10.1038/nature04931

Shipton, Z. K., Soden, A. M., Kirkpatrick, J. D., Bright, A. M., & Lunn, R. J. (2006). How Thick is a Fault? Fault Displacement-Thickness Scaling Revisited. In R. Abercrombie, A. McGarr, G. D. Toro, & H. Kanamori (Eds.), *Earthquakes: Radiated Energy and the Physics of Faulting* (pp. 193–198). American Geophysical Union. https://doi.org/10.1029/170GM19

Sibson, R. H. (2003). Thickness of the Seismic Slip Zone. *Bulletin of the Seismological Society of America*, *93*(3), 1169–1178. https://doi.org/10.1785/0120020061

Skarbek, R. M., Rempel, A. W., & Schmidt, D. A. (2012). Geologic heterogeneity can produce aseismic slip transients. *Geophysical Research Letters*, *39*(21), L21306. https://doi.org/10.1029/2012GL053762

Song, T.-R. A., Helmberger, D. V., Brudzinski, M. R., Clayton, R. W., Davis, P., Pérez-Campos, X., & Singh, S. K. (2009). Subducting Slab Ultra-Slow Velocity Layer Coincident with Silent Earthquakes in Southern Mexico. *Science*, *324*(5926), 502–506. https://doi.org/10.1126/science.1167595

Sweet, J. (2014, February 24). *Unlocking the secrets of slow slip in Cascadia using low-frequency earthquakes* (Thesis). Retrieved from https://digital.lib.washington.edu:443/researchworks/handle/1773/27340

Sweet, J. R., Creager, K. C., & Houston, H. (2014). A family of repeating low-frequency earthquakes at the downdip edge of tremor and slip. *Geochemistry, Geophysics, Geosystems*, *15*(9), 3713–3721. https://doi.org/10.1002/2014GC005449

Szeliga, W., Melbourne, T., Santillan, M., & Miller, M. (2008). GPS constraints on 34 slow slip events within the Cascadia subduction zone, 1997–2005. *Journal of Geophysical Research: Solid Earth*, *113*(B4), B04404. https://doi.org/10.1029/2007JB004948

Thomas, A. M., & Bostock, M. G. (2015). Identifying low-frequency earthquakes in central Cascadia using cross-station correlation. *Tectonophysics*, *658*, 111–116. https://doi.org/10.1016/j.tecto.2015.07.013

Thomas, A. M., Beroza, G. C., & Shelly, D. R. (2016). Constraints on the source parameters of low-frequency earthquakes on the San Andreas Fault. *Geophysical Research Letters*, *43*(4), 2015GL067173. https://doi.org/10.1002/2015GL067173

Waldhauser, F. (2001). *hypoDD-A Program to Compute Double-Difference Hypocenter Locations* (USGS Numbered Series No. 2001–113). Retrieved from http://pubs.er.usgs.gov/publication/ofr01113

Waldhauser, F., & Ellsworth, W. L. (2000). A Double-Difference Earthquake Location Algorithm: Method and Application to the Northern Hayward Fault, California. *Bulletin of the Seismological Society of America*, *90*(6), 1353–1368. https://doi.org/10.1785/0120000006

Wang, K., Dragert, H., Kao, H., & Roeloffs, E. (2008). Characterizing an "uncharacteristic" ETS event in northern Cascadia. *Geophysical Research Letters*, *35*(15), L15303. https://doi.org/10.1029/2008GL034415

Watanabe, T., Hiramatsu, Y., & Obara, K. (2007). Scaling relationship between the duration and the amplitude of non-volcanic deep low-frequency tremors. *Geophysical Research Letters*, *34*(7), L07305. https://doi.org/10.1029/2007GL029391

Wech, A. G. (2016). Extending Alaska's plate boundary: Tectonic tremor generated by Yakutat subduction. *Geology*, *44*(7), 587–590. https://doi.org/10.1130/G37817.1

Wech, A. G., & Creager, K. C. (2008). Automated detection and location of Cascadia tremor. *Geophysical Research Letters*, *35*(20), L20302. https://doi.org/10.1029/2008GL035458

Wech, A. G., & Creager, K. C. (2011). A continuum of stress, strength and slip in the Cascadia subduction zone. *Nature Geoscience*, *4*(9), 624–628. https://doi.org/10.1038/ngeo1215

Wech, A. G., Creager, K. C., & Melbourne, T. I. (2009a). Seismic and geodetic constraints on Cascadia slow slip. *Journal of Geophysical Research: Solid Earth*, *114*(B10), B10316. https://doi.org/10.1029/2008JB006090

Wech, A. G., Creager, K. C., & Melbourne, T. I. (2009b). Seismic and geodetic constraints on Cascadia slow slip. *Journal of Geophysical Research: Solid Earth*, *114*(B10), B10316. https://doi.org/10.1029/2008JB006090

Wech, A. G., Boese, C. M., Stern, T. A., & Townend, J. (2012). Tectonic tremor and deep slow slip on the Alpine Fault. *Geophysical Research Letters*, *39*(10), L10303. https://doi.org/10.1029/2012GL051751

Yoshioka, S., Mikumo, T., Kostoglodov, V., Larson, K. M., Lowry, A. R., & Singh, S. K. (2004). Interplate coupling and a recent aseismic slow slip event in the Guerrero seismic gap of the Mexican subduction zone, as deduced from GPS data inversion using a Bayesian information criterion. *Physics of the Earth and Planetary Interiors*, *146*(3), 513–530. https://doi.org/10.1016/j.pepi.2004.05.006

Appendix 1: Chapter 1 supplementary materials

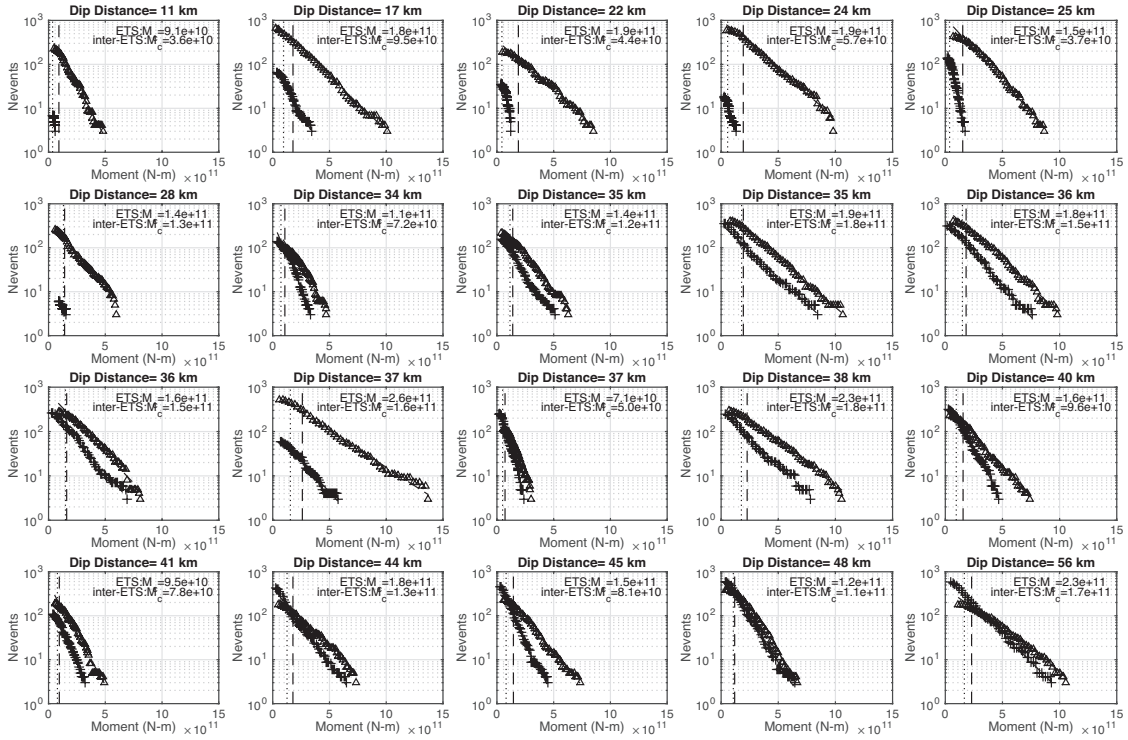

Figure A1.1: Exponential moment-frequency distributions during ETS events and inter-ETS time periods for LFE families ordered from updip (top left) to downdip (bottom right). Dip distances are from the updip limit of tremor. LFEs during ETS events are triangles and LFEs during inter-ETS times periods are crosses. The dashed lines and dot-dashed lines respectively are the characteristic moments for ETS events and inter-ETS time periods respectively.

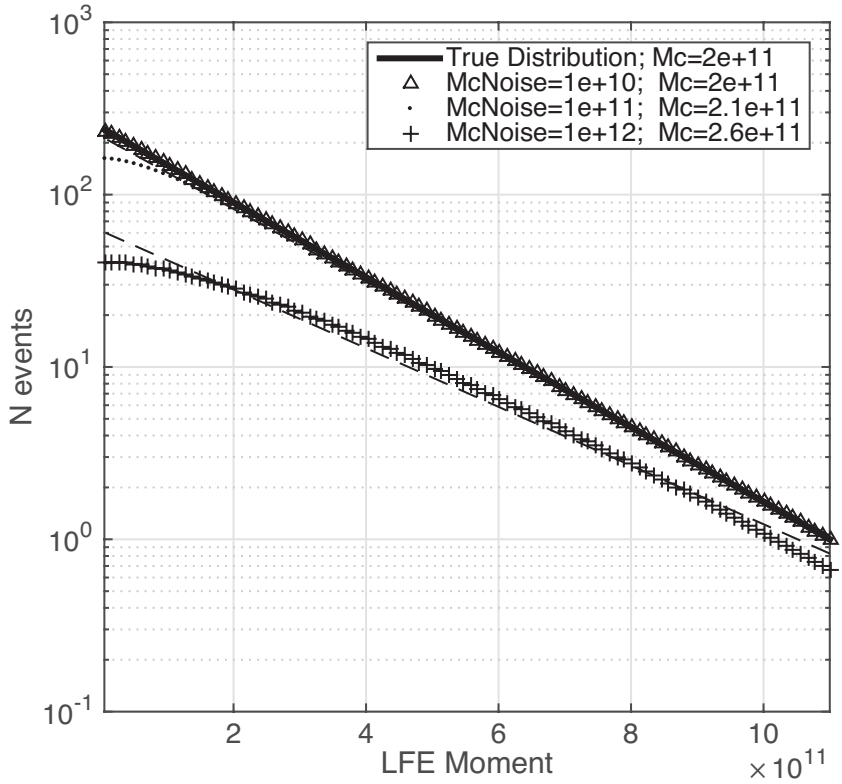

Figure A1.2: Consider a synthetic LFE catalog with an exponential distribution and Mc=2e11 N-m (solid line). This figure shows the best-fit exponential moment frequency distributions of synthetic "filtered" LFE catalogs. Triangles, dots, and cross represent filtered catalogs created by combining the catalog described above with varying exponential noise (Mc= 1010, 1011, 1012 N-m respectively). The dotted lines show best-fit exponential distributions. Higher noise levels result in a less steep slope, or a higher apparent Mc.

Table A1.1: Chapter 1 LFE Catalog Statistics

Number of LFEs	Number of ETS LFEs	Characteristic Moment (N-m)	Latitude	Longitude	Depth (km)
275	255	1.50×10^{11}	47.73	-123.28	19
291	279	1.45×10^{11}	47.95	-123.40	37
334	308	0.96×10^{11}	47.70	-123.24	24
937	822	1.75×10^{11}	47.77	-123.19	27
411	399	1.45×10^{11}	47.93	-123.24	34
553	541	2.23×10^{11}	47.95	-123.25	35
513	502	1.66×10^{11}	48.02	-123.28	40
340	264	1.89×10^{11}	47.94	-123.20	35
270	256	1.43×10^{11}	48.02	-123.25	39
414	289	2.39×10^{11}	48.21	-123.40	38
781	742	1.95×10^{11}	47.98	-123.22	36

757	565	1.56×10^{11}	47.99	-123.20	37
788	523	2.74×10^{11}	48.21	-123.35	41
623	606	1.32×10^{11}	48.01	-123.19	37
373	359	1.41×10^{11}	48.02	-123.17	38
349	324	1.72×10^{11}	48.11	-123.16	42
377	152	1.02×10^{11}	47.77	-122.95	35
787	731	2.23×10^{11}	48.11	-123.14	42
538	286	1.35×10^{11}	47.90	-123.00	37
984	481	1.95×10^{11}	47.91	-123.00	38
733	272	1.38×10^{11}	47.95	-123.02	40
937	494	1.76×10^{11}	47.90	-122.69	38
378	120	1.48×10^{11}	47.94	-123.01	38
772	381	1.57×10^{11}	47.91	-122.99	38
540	413	1.40×10^{11}	48.17	-123.16	45
763	658	2.56×10^{11}	48.14	-123.12	42
599	168	0.63×10^{11}	47.96	-123.00	40
322	223	1.23×10^{11}	48.16	-123.14	45
689	364	2.08×10^{11}	47.92	-122.97	39
1131	480	1.87×10^{11}	47.94	-122.98	41
135	40	0.46×10^{11}	48.04	-123.02	42
753	314	1.35×10^{11}	47.92	-122.94	38
934	422	1.58×10^{11}	47.98	-122.97	40
483	274	0.90×10^{11}	48.04	-122.99	43
1294	559	1.39×10^{11}	47.91	-122.89	37
1142	343	1.54×10^{11}	47.94	-122.90	42
494	107	0.93×10^{11}	47.98	-122.92	42
1187	358	1.25×10^{11}	48.02	-122.93	42
1193	443	1.07×10^{11}	48.05	-122.93	43
1667	639	1.17×10^{11}	48.08	-122.92	44
1516	356	1.12×10^{11}	48.09	-122.83	42
1028	248	1.95×10^{11}	48.29	-122.95	49
2192	151	0.60×10^{11}	47.89	-122.64	43

Appendix 2: Chapter 2 supplementary materials

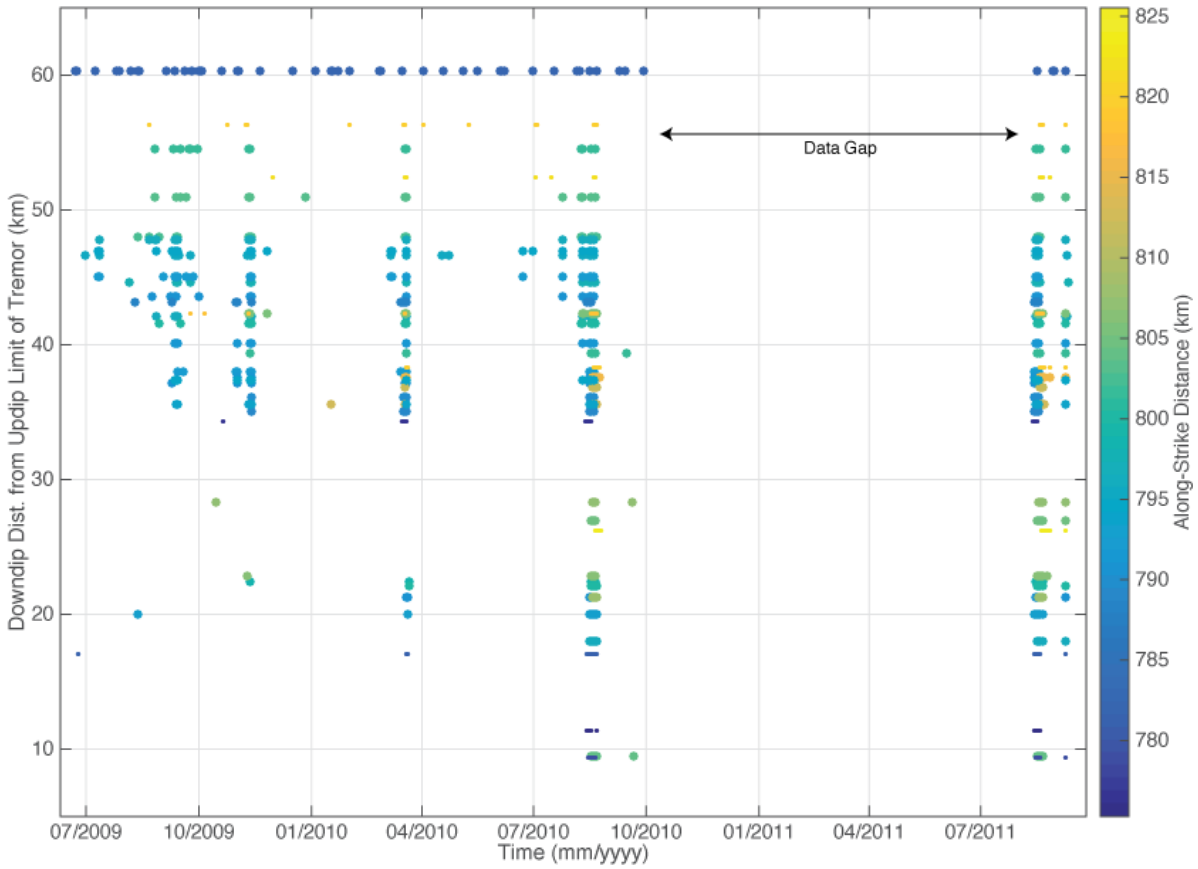

Figure A2.1: LFE catalog over time. Dots are individual LFEs, horizontal lines of dots are LFE families. The y-axis is downdip distance (distance from the updip limit of tremor) and LFEs are color-coded by along-strike distance.

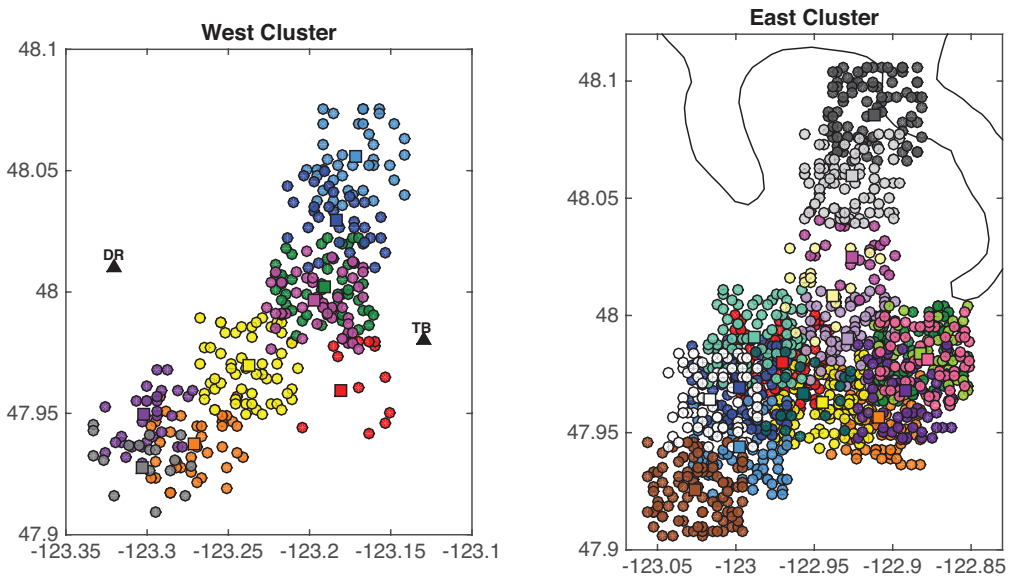

Figure A2.2: LFE starting locations used for the first iteration of the hypoDD inversion. LFEs are randomly assigned to grid points within a 6.5 by 6.5 km box around their LFE family locations.

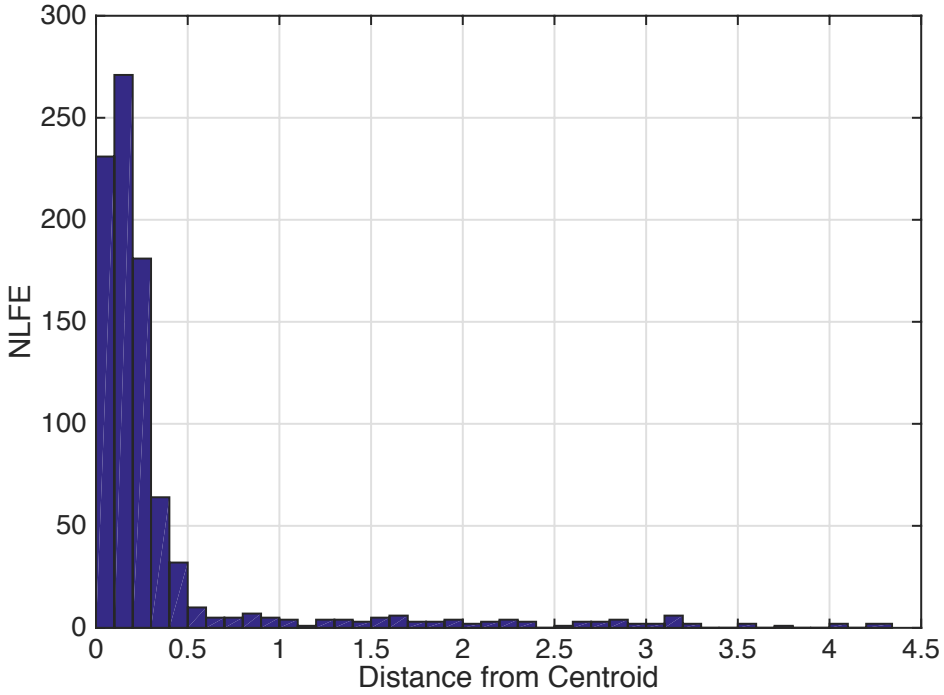

Figure A2.3: Histogram of the distance from each LFE to its family centroid. Near the family centroids the distribution is Gaussian. Father away from the centroid the distribution levels off, showing that the LFEs are evenly and randomly distributed. This is evidence that the locations of LFEs farther from their family centroids are poorly constrained.

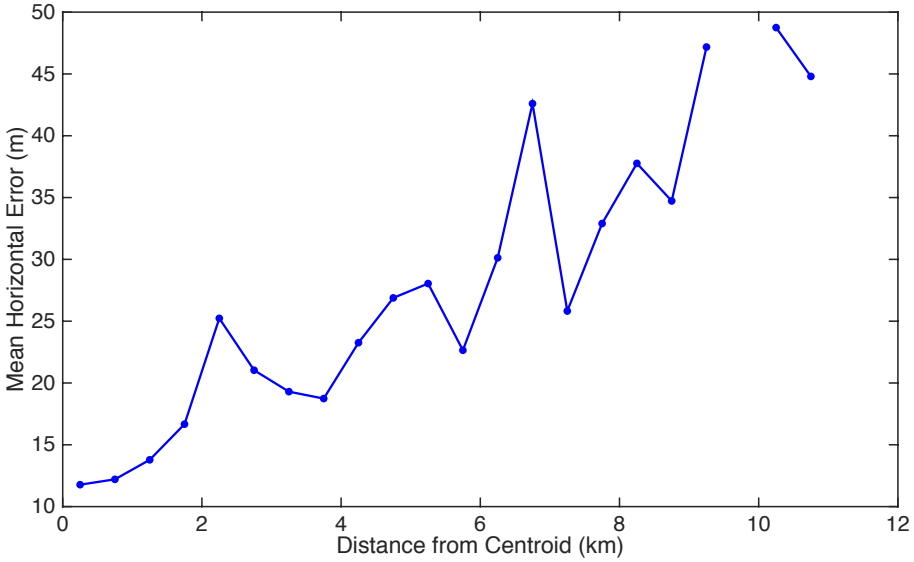

Figure A2.4: Mean horizontal errors for LFEs grouped into bins based on their distance from centroid. Bins are 0.5 km wide (i.e. 0-0.5, 0.5-1, 1-1.5 km, etc.). The mean horizontal error clearly increases as distance from centroid increases. This is evidence that LFEs farther from their family centroids are likely mislocated. Errors are from the LSQR relocation and are likely underestimated.

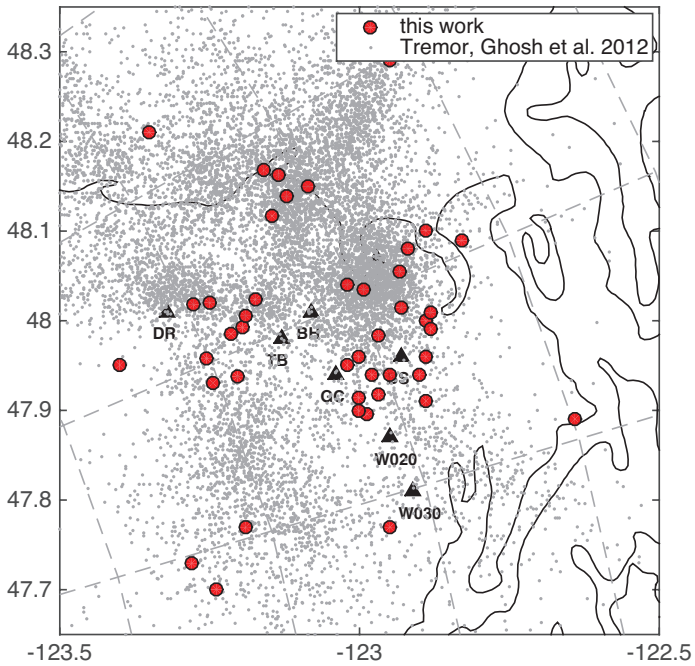

Figure A2.5: LFE family locations from this work (red dots) compared to tremor locations from Ghosh et al. [2012] (grey dots). Tremor is less dense downdip of the majority of LFE families and in the gap in LFE families beneath the TB and BH arrays. Beneath our east cluster of LFE families, tremor is also less dense than in other regions. This inconsistency between catalogs could be due to differences in the methods used to locate LFE families and tremor.

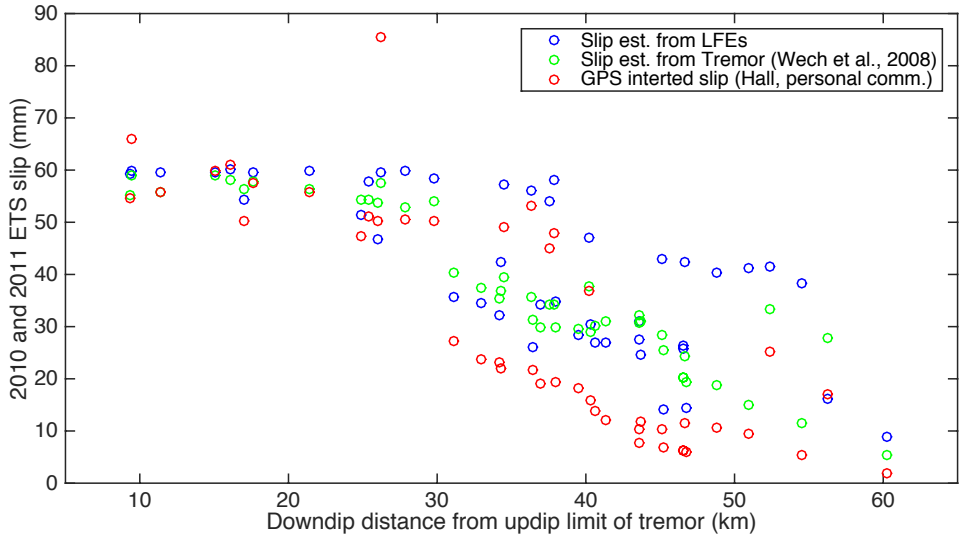

Figure A2.6: ETS slip estimates at the location of each LFE family. Slip is estimated using three different methods: (1) 6 cm * NETS/Nall for LFEs (blue), (2) 6 cm * NETS/Nall for tremor (green), and (3) from the GPS inversions from Hall et al. (personal communication) (red). NETS and Nall are the number of LFEs/tremors during ETS times periods and all time periods respectively. In the paper, we use slip estimated from tremor.

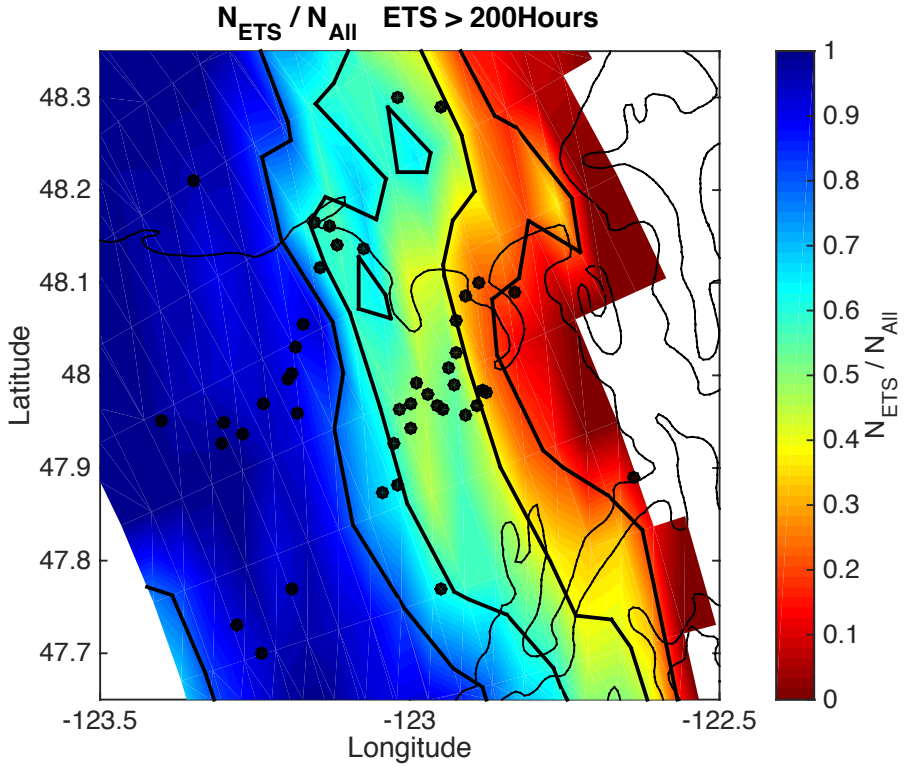

Figure A2.7: Map view of N_{ETS}/N_{all} for tremor for the 2010 and 2011 ETS events (Wech et al. 2008). Clearly the proportion of tremor that occurs during ETS events decreases with downdip distance. Black contours mark N_{ETS}/N_{all} = 0.2, 0.4, 0.6 and 0.8. LFE families are plotted as black circles.

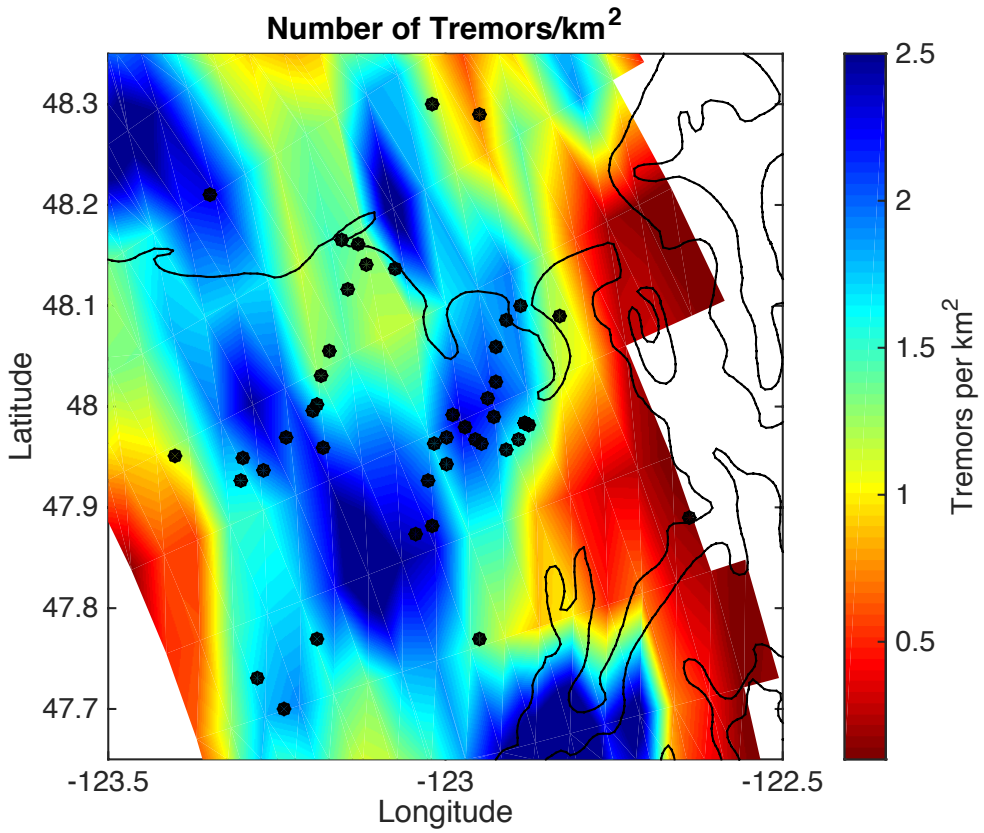

Figure A2.8: Map view of tremors per square kilometer for the 2010 and 2011 ETS events (Wech et al. 2008). LFE families are plotted as black circles. A high-density tremor region corresponds with the location of the east cluster of LFE families.

Table A2.1: Chapter 2 LFE Catalog Statistics

Ref #	Number of LFEs	Number of LFEs, ETS	Characteristic Moment (N-m)	Characteristic Moment, ETS (N-m)	Slip Area A_T (m^2)	Patch Area, A_P (m^2)	Latitude	Longitude	Depth (km)
1	874	558	1.24×10^{11}	1.12×10^{11}	18×10^{4}		48.09	-122.83	42.0
2	1045	701	1.16×10^{11}	1.15×10^{11}	14×10^{4}	1.9×10^{6}	48.08	-122.91	43.3
3	631	321	1.58×10^{11}	1.65×10^{11}	6.1×10^{4}	$.89\times10^{6}$	47.98	-122.97	40.5
4	261	259	1.00×10^{11}	0.87×10^{11}	1.3×10^{4}		47.70	-123.24	24.0
5	264	186	1.06×10^{11}	1.11×10^{11}	1.9×10^{4}		47.77	-122.95	35.0
6	840	759	1.72×10^{11}	1.75×10^{11}	7.8×10^{4}		47.77	-123.19	27.0
7	844	387	1.49×10^{11}	1.70×10^{11}	7.1×10^{4}	$.85\times10^{6}$	47.95	-122.91	39.5
8	744	333	1.95×10^{11}	1.91×10^{11}	6.8×10^{4}	$.85\times10^{6}$	47.96	-122.95	39.7
9	1208	180	0.62×10^{11}	0.37×10^{11}	4.3×10^{4}		47.89	-122.64	43.0
10	263	225	1.81×10^{11}	1.81×10^{11}	2.5×10^{4}		47.96	-123.18	35.5
11	680	298	1.14×10^{11}	0.98×10^{11}	4.8×10^{4}	$.45\times10^{6}$	47.98	-122.88	40.7
12	665	661	2.70×10^{11}	2.70×10^{11}	10×10^{4}		48.21	-123.35	41.0

13	606	246	2.00×10^{11}	2.15×10^{11}	8.3×10^{4}	1.5×10^{6}	47.94	-123.00	38.9
14	800	460	1.76×10^{11}	1.85×10^{11}	7.5×10^{4}		17.88	-123.02	38.2
15	656	382	1.61×10^{11}	1.67×10^{11}	7.1×10^{4}	1.2×10^{6}	47.97	-123.00	39.7
16	352	349	1.40×10^{11}	1.40×10^{11}	2.8×10^{4}	$.56\times10^{6}$	47.94	-123.27	34.3
17	719	370	1.34×10^{11}	1.49×10^{11}	5.7×10^{4}	$.94\times10^{6}$	47.99	-122.93	40.5
18	491	489	2.17×10^{11}	2.17×10^{11}	6.3×10^{4}	1.0×10^{6}	47.97	-123.24	36.2
19	634	493	1.54×10^{11}	1.52×10^{11}	4.6×10^{4}	$.74\times10^{6}$	48.00	-123.19	37.0
20	292	284	1.40×10^{11}	1.42×10^{11}	2.5×10^{4}	1.0×10^{6}	48.06	-123.17	37.9
21	540	538	1.26×10^{11}	1.26×10^{11}	4.3×10^{4}	$.93\times10^{6}$	48.03	-123.18	37.0
22	242	241	1.42×10^{11}	1.42×10^{11}	1.9×10^{4}		47.95	-123.40	37.0
23	329	235	0.96×10^{11}	1.00×10^{11}	2.8×10^{4}	$.49\times10^{6}$	48.02	-122.93	41.2
24	400	400	1.61×10^{11}	1.61×10^{11}	3.7×10^{4}		47.95	-123.3	38.6
25	760	535	1.06×10^{11}	1.10×10^{11}	8.2×10^{4}	$.75\times10^{6}$	48.06	-122.92	42.9
26	687	663	1.92×10^{11}	1.90×10^{11}	7.7×10^{4}	$.64\times10^{6}$	48.00	-123.20	36.6
27	928	496	2.01×10^{11}	2.07×10^{11}	9.7×10^{4}	1.1×10^{6}	47.93	-123.03	38.8
28	809	218	1.95×10^{11}	2.28×10^{11}	6.0×10^{4}		48.29	-122.95	49.0
29	642	578	2.44×10^{11}	2.50×10^{11}	14×10^{4}		48.14	-123.12	41.8
30	524	363	2.00×10^{11}	2.03×10^{11}	7.3×10^{4}		48.30	-123.02	41.0
31	686	656	2.27×10^{11}	2.25×10^{11}	12×10^{4}		48.12	-123.15	41.5
32	270	261	1.32×10^{11}	1.33×10^{11}	3.4×10^{4}		48.16	-123.13	44.9
33	395	370	1.43×10^{11}	1.38×10^{11}	4.8×10^{4}		48.17	-123.16	45.2
34	538	421	2.59×10^{11}	2.64×10^{11}	9.8×10^{4}		48.14	-123.08	42.2
35	381	181	0.66×10^{11}	0.70×10^{11}	1.4×10^{4}	$.38\times10^{6}$	47.99	-122.99	40.1
36	428	255	1.30×10^{11}	1.35×10^{11}	2.8×10^{4}		47.87	-123.04	37.7
37	550	238	1.35×10^{11}	1.34×10^{11}	3.4×10^{4}	1.9×10^{6}	47.96	-123.02	39.3
38	218	215	1.41×10^{11}	1.41×10^{11}	1.8×10^{4}		47.73	-123.28	19.0
39	235	233	1.35×10^{11}	1.36×10^{11}	0.2×10^{4}		47.93	-123.30	35.9
40	515	221	1.05×10^{11}	1.08×10^{11}	1.8×10^{4}	$.29\times10^{6}$	47.98	-122.88	40.7
41	251	113	1.82×10^{11}	2.10×10^{11}	3.9×10^{4}	1.0×10^{6}	47.97	-122.96	40.5
42	1346	320	1.19×10^{11}	1.41×10^{11}	2.6×10^{4}		47.97	-122.89	43.2
43	842	204	1.27×10^{11}	1.26×10^{11}	5.9×10^{4}		47.98	-122.88	41.8
44	807	553	1.03×10^{11}	1.09×10^{11}	4.4×10^{4}		48.1	-122.89	44.0
45	85	35	0.47×10^{11}	0.53×10^{11}	13×10^{4}		48.0	-122.94	40.7

Table A2.2: Chapter 2 LFE Catalog Statistics

NITER	WTCCP	WTCCS	WRCC	WDCC	WTCTP	WTCTS	WRCT	WDCT	DAMP
10	1	0.5	8	4	-9	-9	-9	-9	100
10	1	0.5	5	4	-9	-9	-9	-9	100
20	1	0.5	4	4	-9	-9	-9	-9	100
30	1	0.5	3	4	-9	-9	-9	-9	100

We use only cross-correlation data, so at catalog data parameters are inactive (-9). NITER: Number of iterations with the current setting parameters. WTCCP, WTCCS: Weights for P and S wave cross-correlation data. WTCTP, WTCTS: Weights for P and S wave catalog data. WRCC, WRCT: residual cut-off threshold in seconds for cross-correlation and catalog data. WDCC, WDCT: maximum separation distance in kilometers between cross-correlation and catalog linked pairs. DAMP: Damping for least squares solution.

Table A2.3: Parameters for the Connected Patch and Ductile Matrix Models

	Ductile Matrix Model			Connected Patch Model		
Ref #	Slip/LFE (mm)	Diameter /LFE (m)	Stress drop/ LFE (kPA)	Slip/LFE (mm)	Diameter/LFE (m)	Stress drop/ LFE (kPA)
2	.29-.97	130-230	$.10\text{-}.63\times10^3$	.019-.064	490-900	1.8-11
3	.65-2.2	81-150	$.36\text{-}2.2\times10^3$	.039-.13	340-610	5.2-31
7	.53-1.8	89-160	$.27\text{-}1.6\times10^3$	.039-.13	330-600	5.3-32
8	.61-2.0	88-160	$.31\text{-}1.9\times10^3$	.043-.14	330-600	5.9-36
11	.71-2.4	72-130	$.44\text{-}2.7\times10^3$	.065-.22	240-440	12-75
13	.59-2.0	96-180	$.28\text{-}1.7\times10^3$	.029-.097	440-800	3.0-18
15	.54-1.8	89-160	$.28\text{-}1.7\times10^3$	.029-.095	390-710	3.3-20
16	.62-2.1	54-100	$.51\text{-}3.1\times10^3$	.026-.087	270-490	4.3-27
17	.54-1.8	81-150	$.30\text{-}1.8\times10^3$	.030-.098	350-630	3.8-23
18	.42-1.4	84-150	$.22\text{-}1.4\times10^3$	.023-.076	360-660	2.8-17
19	.42-1.4	72-130	$.27\text{-}1.6\times10^3$	.023-.076	310-560	3.4-20
20	.70-2.3	54-100	$.59\text{-}3.6\times10^3$	.015-.051	360-660	1.9-12
21	.40-1.3	67-120	$.27\text{-}1.7\times10^3$	.015-.051	340-630	2.0-12
23	.87-2.9	56-100	$.71\text{-}4.3\times10^3$	.043-.14	250-450	7.9-48
25	.38-1.3	96-180	$.18\text{-}1.1\times10^3$	.037-.12	310-560	5.3-33
26	.31-1.0	93-170	$.15\text{-}.91\times10^3$	.033-.11	290-520	5.2-31
27	.40-1.3	110-190	$.17\text{-}1.0\times10^3$	.032-.11	370-680	3.9-24
35	1.1-3.8	40-73	$1.3\text{-}7.7\times10^3$	.037-.12	220-400	7.6-46
37	.89-3.0	61-110	$.66\text{-}4.0\times10^3$	.014-.045	490-900	1.2-7
40	.94-3.1	38-350	$1.1\text{-}6.7\times10^3$	.038-.12	190-350	8.9-54
41	1.8-6.1	66-120	$1.2\text{-}7.6\times10^3$	.062-.21	360-650	7.9-48